

Occurrence Statistics and Driving Mechanisms of Ionospheric Ultra-Low Frequency Waves Observed by SuperDARN Radars

Xueling Shi

Dissertation submitted to the Faculty of the
Virginia Polytechnic Institute and State University
in partial fulfillment of the requirements for the degree of

Doctor of Philosophy

in

Electrical Engineering

J. Michael Ruohoniemi, Chair

Joseph B. H. Baker, Co-chair

Wayne A. Scales

C. Robert Clauer

Bhuvana Srinivasan

R. Michael Buehrer

April 18, 2019

Blacksburg, Virginia

Keywords: ULF waves, geomagnetic pulsations, SuperDARN, ionosphere, magnetosphere

Copyright 2019, Xueling Shi

Occurrence Statistics and Driving Mechanisms of Ionospheric Ultra-Low Frequency Waves Observed by SuperDARN Radars

Xueling Shi

(ABSTRACT)

Ultra-low frequency (ULF; 1 mHz - 1 Hz) waves are known to play an important role in the transfer of energy from the solar wind to Earth's magnetosphere and ionosphere. The Super Dual Auroral Radar Network (SuperDARN) is an international network consisting of 35 low-power high frequency (HF: 3-30 MHz) coherent scatter radars at middle to polar latitudes that look into Earth's upper atmosphere and ionosphere. In this study, we use Doppler velocity measurements obtained by the SuperDARN radars and coordinated spacecraft observations to investigate the occurrence statistics and driving mechanisms of ionospheric ULF waves. We begin in Chapter 2 with a case study of Pi2 pulsations which are short-duration (5-15 min) damped geomagnetic field oscillations with periods of 40-150 s. Simultaneous observations of Pi2 pulsations from THEMIS spacecraft, midlatitude SuperDARN radars, and ground magnetometers, together with analysis of their longitudinal polarization pattern and azimuthal phase propagation, confirmed that they are consistent with a plasmaspheric virtual resonance excited by a longitudinally localized source near midnight. In Chapter 3, to further investigate the overall occurrence of ionospheric ULF signatures, a comprehensive statistical study was conducted using an automated detection algorithm to identify ionospheric signatures of Pc3-4 and Pc5 waves over 7 years of high time resolution SuperDARN radar data. Specifically, we have investigated their spatial occurrence, frequency characteristics, seasonal factors, and dependence on solar wind and geomagnetic conditions. We note two particular findings: (i) an internal wave-particle interaction source is most likely responsible for Pc4 waves at high latitudes in the duskside ionosphere; and, (ii) a source associated with magnetotail dynamics during active geomagnetic times is suggested for Pc3-4/Pi2 waves at midlatitudes in the nightside ionosphere. These findings are further expanded in Chapter 4 which investigates the hypothesis that internal wave-particle interactions are an important source for generation of these waves. A case study of long-lasting poloidal waves was conducted using coordinated observations with the GOES and THEMIS satellites to examine the generation and propagation of waves observed in the dayside ionosphere by multiple SuperDARN radars. The source of wave excitation is suggested to be bump-on-tail ion distributions at 1-3 keV. Collectively, these research findings provide better constraints on where and when ionospheric ULF waves occur, their source mechanisms, and how they might affect magnetospheric and ionospheric dynamics.

Occurrence Statistics and Driving Mechanisms of Ionospheric Ultra-Low Frequency Waves Observed by SuperDARN Radars

Xueling Shi

(GENERAL AUDIENCE ABSTRACT)

Earth's magnetic field, approximates that of a bar magnet. It is an effective barrier to charged particles originating directly from the Sun and protects us against harmful space weather influences. The geomagnetic field lines can oscillate in ultra-low frequencies (ULF: 1 mHz - 1 Hz). These natural oscillations of closed magnetic field lines, analogous to vibrations on a stretched string, are also called geomagnetic pulsations or ULF waves. The interaction between matter and electromagnetic fields emitted from the Sun and the Earth's outer atmosphere and magnetic field form a magnetic shield named the Earth's magnetosphere. ULF waves play a key role in the transfer of energy from outside this shield to regions inside it, including Earth's upper atmosphere and ionosphere (a region extending from about 60 km to 1000 km above the Earth's surface). In this study, we use Doppler velocity measurements obtained by the Super Dual Auroral Radar Network (SuperDARN) radars and coordinated spacecraft observations to investigate the occurrence statistics and driving mechanisms of ionospheric ULF waves. We begin in Chapter 2 with an event study of a type of irregular pulsations (Pi2) which are short-duration (5-15 min) damped geomagnetic field oscillations with periods of 40-150 s. Simultaneous observations of Pi2 pulsations from NASA THEMIS spacecraft, midlatitude SuperDARN radars, and ground magnetometers, together with further analysis of wave spectra and propagation, confirmed their driving mechanism as a type of magnetic resonance, analogous to striking a bell. In Chapter 3, to further investigate the overall occurrence of ionospheric ULF signatures, a statistical study was conducted using an automated detection algorithm to identify ionospheric signatures of ULF waves over 7 years of high time resolution SuperDARN radar data. Specifically, we have investigated their spatial occurrence, frequency characteristics, seasonal factors, and dependence on solar and geomagnetic activity. We obtained findings regarding the different driving sources of waves observed in different regions. The findings are further expanded in Chapter 4 which investigates the generation of waves through energy exchange with charged particles. A case study of long-lasting (2-3 days) waves was conducted using coordinated observations with the GOES and THEMIS satellites to examine the generation and propagation of waves observed in the dayside ionosphere by multiple SuperDARN radars. The source of wave excitation is suggested to be unstable particle distributions in the magnetosphere. Collectively, these research findings provide better constraints on where and when ULF waves occur, their source mechanisms, and how they affect dynamics in the geospace environment.

Dedication

This dissertation is dedicated to my husband Dong Lin, our unborn child Simai Lin, and our parents (Zhanghe Shi and Yun Zhao, Lianhong Lin and Youlian Tu).

Acknowledgments

Throughout my PhD study I have received a lot of support and assistance. I would first like to acknowledge my PhD supervisors, Professor J. Michael Ruohoniemi and Professor Joseph B. H. Baker, for their mentoring, support, and inspiration since my enrollment in 2014. I will never forget the enlightening guidance and warmhearted kindness of my supervisors. Mike and Jo, you are the most admired and respected professors in my life! I feel so proud to be your student and cannot wait to start my post-graduate career with all the knowledge and spirit you have taught me.

I am also sincerely grateful to all of my co-authors and collaborators for their contribution to studies presented in this dissertation. Among them, I would like to especially acknowledge Dr. Michael Hartinger who has been providing weekly office hours for productive research discussions and career development suggestions. I would like to thank my academic advisor Ms. JoAnna Lewis, Space@VT center administrator Ms. Debbie Collins, RF engineer Mr. Kevin Sterne, and the department computer systems administrators John Ghra, Brandon Russell, and Roderick DeHart, for their technical support and assistance throughout my PhD study. I would like to thank my labmates in the SuperDARN research group for open-minded suggestions and insightful discussions, including Nathaniel Frissell, Evan Thomas, Garima Malhotra, Maimaitirebike Maimaiti, Shibaji Chakraborty, Bharat Kunduri, and Paul Kennedy. I would like to thank my Space@VT colleagues for creating a collaborative and enjoyable working environment all together, including Zhonghua Xu, Dong Lin, Magda Moses, Karthik Venkataramani, Thomas Edwards, Yuxiang Peng, Taikara Peek, Shantanab Debchaudhury, Shane Coyle and many others.

I would like to thank Debbie again for always listening to me, encouraging me, and treating me like family. I would like to thank my dear friends in Blacksburg: Wenjing Xue and Lijie Tang family, Yufeng Liu and Caleb Reach couple, Wenjuan Sun and Song Xue couple, Xuewen Feng and Zhengyang Liu couple, Ying Li, Zichen Zhang and many others, who have made my life in the U.S. much easier, warmer, and more colorful.

Finally, I specially thank my family who have been giving me lots of comfort and support in my life. This dissertation would not have been possible without the continued support and encouragement from my family, especially my husband Dong Lin.

Funding for this research was provided by the National Science Foundation under grants AGS-1341918, AGS-1342968, and ICER-1541007. Support was also provided by National Aeronautics and Space Administration Headquarters under the NASA Earth and Space Science Fellowship (NESSF) Program - Grant 80NSSC17K0456 P00001.

Attribution

Several colleagues provided data, research, figures, and text which culminated in the three manuscripts presented as Chapters 2, 3, and 4 in this dissertation. A brief description of their contribution is included here.

J. Michael Ruohoniemi, PhD (Virginia Tech) is a Professor in the Bradley Department of Electrical and Computer Engineering at Virginia Tech. He was a co-author for Chapters 2, 3, and 4 and is the Principal Investigator for the NSF grants and NASA NESSF grant supporting this research. Dr. Ruohoniemi is one of two advisors for my graduate studies and has contributed text and editorial comments throughout this dissertation.

Joseph B. H. Baker, PhD (Virginia Tech) is an Associate Professor in the Bradley Department of Electrical and Computer Engineering at Virginia Tech. He was a co-author for Chapters 2, 3, and 4 and is a Co-Investigator for the NSF grants and a Support Staff for the NASA NESSF grant supporting this research. Dr. Baker is one of two advisors for my graduate studies and has contributed text and editorial comments throughout this dissertation.

Michael Hartinger, PhD (Virginia Tech and Space Science Institute, Boulder) is a Research Assistant Professor in the Bradley Department of Electrical and Computer Engineering at Virginia Tech and a Research Scientist at Space Science Institute, Boulder. He was a co-author and has provided valuable inputs for Chapters 2, 3, and 4. Dr. Hartinger has also contributed text and editorial comments for all three manuscripts.

Nathaniel A. Frissell, PhD (New Jersey Institute of Technology) is a Research Professor in the Center for Solar-Terrestrial Research at New Jersey Institute of Technology. He was a co-author for Chapter 2 and provided some editorial comments for Chapter 2.

Jiang Liu, PhD (University of California Los Angeles) is an Assistant Researcher in the

Department of Earth, Planetary and Space Sciences at University of California Los Angeles. He was a co-author for Chapter 2 and provided guidance on THEMIS satellite data analysis.

Dong Lin, PhD (Virginia Tech) is a PhD student in the Bradley Department of Electrical and Computer Engineering at Virginia Tech. He was a co-author for Chapter 3 and developed the numerical experiments described in Appendix A. Dong has also contributed text and editorial comments for Chapter 3.

Emma C. Bland, PhD (University Centre in Svalbard and Birkeland Centre for Space Science) is a Post-doc in Middle Atmospheric Physics, Birkeland Centre for Space Science and the University Centre in Svalbard. She was a co-author for Chapter 3 and provided guidance on data processing and algorithm development. Dr. Bland has also contributed text and editorial comments for Chapter 3.

Wayne A. Scales, PhD (Virginia Tech) is a Professor in the Bradley Department of Electrical and Computer Engineering at Virginia Tech. He was a co-author for Chapter 3 and provided guidance for the numerical experiment development.

Kyle R. Murphy, PhD (NASA Goddard Space Flight Center) is a Research Scientist at NASA Goddard Space Flight Center. He was a co-author for Chapter 4 and also contributed text and editorial comments.

Juan V. Rodriguez, PhD (University of Colorado Boulder and National Oceanic and Atmospheric Administration) is the Director of NOAA National Centers for Environmental Information and Cooperative Institute for Research in Environmental Sciences at University of Colorado at Boulder. He is a co-author for Chapter 4 and provided guidance on GOES satellite data analysis. Dr. Rodriguez also provided editorial comments for Chapter 4.

Yukitoshi Nishimura, PhD (Boston University and University of California Los Angeles) is a Research Associate Professor in the Department of Electrical and Computer Engineering and Center for Space Physics at Boston University. He is a co-author for Chapter 4 and provided guidance on THEMIS satellite data analysis. Dr. Nishimura has also contributed

editorial comments for Chapter 4.

Kathryn A. McWilliams, PhD (University of Saskatchewan) is an Associate Professor in the Department of Physics and Engineering Physics at the University of Saskatchewan. She was a co-author for Chapter 4 and is the Principal Investigator of SuperDARN Canada. Dr. McWilliams also provided editorial comments for Chapter 4.

Vassilis Angelopoulos, PhD (University of California Los Angeles) is a Professor in the Department of Earth, Planetary and Space Sciences at University of California Los Angeles. He was a co-author for Chapter 4 and is the Principal Investigator of the NASA THMEIS mission.

Contents

List of Figures	xiv
List of Tables	xxiii
1 Introduction	1
1.1 The Solar-Terrestrial Environment	1
1.1.1 The Sun and Solar Wind	1
1.1.2 The Earth’s Magnetosphere	2
1.1.3 Structure of the Earth’s Atmosphere and Ionosphere	7
1.1.4 The Solar Wind - Magnetosphere - Ionosphere Coupling	10
1.1.5 Geomagnetic Activity	13
1.2 Ultra-Low Frequency Waves	16
1.2.1 Historical Background	16
1.2.2 MHD Theory	18
1.2.3 Definition and Category	20
1.2.4 Driving Mechanisms	23
1.3 Objectives and Dissertation Organization	27
2 Simultaneous Space and Ground-Based Observations of a Plasmaspheric	

Virtual Resonance	29
2.1 Introduction	30
2.2 Data Sets	34
2.2.1 THEMIS Spacecraft	34
2.2.2 SuperDARN Radars	35
2.2.3 Other Data Sets	36
2.3 Observations and Analysis	38
2.3.1 Interplanetary and Geomagnetic Conditions	39
2.3.2 THEMIS Spacecraft Observations	40
2.3.3 Ground Magnetometer Measurements	44
2.3.4 SuperDARN HF Radar Measurements	48
2.3.5 Polarization and Propagation Analysis	53
2.4 Discussion	57
2.5 Conclusions	61
3 Survey of Ionospheric Pc3-5 ULF Wave Signatures in SuperDARN High Time Resolution Data	64
3.1 Introduction	66
3.2 Instrumentation and Event Detection Method	68
3.2.1 SuperDARN	68
3.2.2 Data Processing and Event Selection	70

3.3	Statistical Results	73
3.3.1	Spatial Occurrence Distribution	74
3.3.2	Frequency Characteristics	76
3.3.3	Seasonal Effects	78
3.3.4	Solar Wind and Geomagnetic Disturbance Dependencies	80
3.4	Discussion	83
3.5	Summary and Conclusions	86
4	Long-Lasting Poloidal ULF Waves Observed by Multiple Satellites and High-Latitude SuperDARN Radars	88
4.1	Introduction	90
4.2	Instrumentation and Analysis	92
4.2.1	Satellite Missions	92
4.2.2	Ground-based Instruments	93
4.2.3	Signal Processing	94
4.2.4	Instrument Locations	94
4.3	Observations	95
4.3.1	Event Overview	96
4.3.2	Wave Properties in the Magnetosphere	99
4.3.3	Wave Properties in the Ionosphere	102
4.3.4	Wave Spatial and Spectral Characteristics	106

4.4 Discussion	107
4.5 Conclusions	114
5 Conclusions and Future Work	118
Bibliography	122
Appendices	151
Appendix A Methodology: Lomb-Scargle Periodogram	152

List of Figures

1.1	The Solar Wind and Earth’s Magnetosphere. [Image credit: https://helios.gsfc.nasa.gov/magnet.html]	3
1.2	Motions of charged particles in the geomagnetic field: (a) schematic representation of the guiding-center trajectory of a trapped charged particle; (b) three cyclic motions: gyro, bounce, and drift. [Regi, 2016]	4
1.3	Left: Earth’s plasmasphere as measured by IMAGE’s extreme ultraviolet imager [Sandel et al., 2003]; Right: A cross section of Van Allen radiation belts. [Image credit: NASA]	6
1.4	Typical profiles of neutral atmospheric temperature (left) and ionospheric plasma density (right) with the various layers designated. [Kelley, 2009]	8
1.5	Magnetic reconnection in the Earth’s magnetosphere and the associated magnetospheric and ionospheric convection. [Adapted from Kivelson and Russell, 1995]	11
1.6	Fields of view of 35 currently operational SuperDARN radars from the northern (left) and southern (right) hemispheres in magnetic coordinates. Polar cap, high-latitude, and mid-latitude radar FOVs are shaded green, blue, and red, respectively.	12
1.7	The Dst index shows the SSC, initial phase, main phase, and the recovery phase of a classic geomagnetic storm [Lui, 2000].	14

1.8	An example of a photographic recording of magnetic oscillations of a compass needle. From Figure 1 in McPherron [2005].	17
1.9	Fundamental (top) and second harmonic (bottom) perturbations looking earthward at a field line stretched from north to south for toroidal modes (left) and sketched in a meridional plane for poloidal modes (right) [Hughes, 1994]. ΔH and ΔD refer to north-south and east-west perturbations, respectively.	21
1.10	A schematic representation of the generation of a FLR by compressional waves of the waveguide mode excited via the Kelvin-Helmholtz instability at the magnetopause. [Adapted from Rae et al., 2008]	22
1.11	A schematic representation of standing poloidal Alfvén waves and wave-particle resonance interactions [Dai et al., 2013].	25
2.1	Locations of various space and ground instruments. The upper panels show the locations of THE (blue curve) and THD (red curve) spacecraft in (a) the X-Y plane and (b) the X-Z plane in SM coordinates. The asterisks identify the starting time at 06:04 UT on 25 September 2014. The lower panel (c) shows the locations of ionospheric footprints of THE (blue asterisk) and THD (red asterisk), ground magnetometers (black dots), THEMIS all-sky imagers (green dots), and SuperDARN radar FOV and camping beams of FHW (cyan), FHE (red), and BKS (green) in AACGM coordinates at 06:04 UT.	37
2.2	Interplanetary and geomagnetic conditions on 25 September 2014: (a) OMNI IMF B_y and B_z components and (b) solar wind speed V_x in the Geocentric Solar Magnetospheric (GSM) coordinate system, (c) solar wind proton density N_p , (d) AE (blue), AU (green), and AL (red) indices, and (e) SymH index. The cyan shaded region identifies the time interval of interest.	39

2.3	Plasmaspheric context of two THEMIS spacecraft during the time interval of Pi2 activity. Each panel shows profiles of spacecraft potential (blue) and electron density (black) for (a) THE and (b) THD. The cyan shaded region identifies the time interval of interest. Vertical dashed red lines identify sharp gradients indicative of plasmopause crossings.	40
2.4	Time series of Pi2 pulsations observed inside the plasmasphere. The upper five panels show THD measurements of (a) E_x , (b) E_y , (c) B_x , (d) B_y , and (e) B_z components, while the bottom panel (f) shows the CCNV ground magnetometer H component. Vertical dashed red lines indicate prominent peaks in the THD E_y component.	41
2.5	Cross-spectral analysis of THD E_y and B_z components: (a) Auto spectrum of the E_y component from THD, (b) Auto spectrum of the B_z component from THD, (c) Cross spectrum of the E_y and B_z components, (d) Coherence between the E_y and B_z components, and (e) E_y - B_z phase shift as a function of frequency. Vertical dashed red lines indicate the dominant cross-spectral frequency peak at ~ 13.4 mHz.	43
2.6	Cross-spectral analysis of THD E_y and CCNV H components (same format as Figure 2.5).	44
2.7	Magnetic local time variation of pulsations seen by several low latitude ground magnetometers. Filtered magnetic field H (solid black) and D (dashed blue) components are shown. Station identifiers are on the left axes and the relevant L and MLT values are labeled at the upper right-hand corner in each panel. Vertical dashed red lines identify the same times as those shown in Figure 2.4.	45

2.8	Latitudinal variation of pulsations seen by several nightside ground magnetometers straddling the footprint latitude of the plasmopause (similar format to Figure 2.7).	46
2.9	Spectral analysis of ground magnetometer data shown in Figure 2.8: auto spectral power density of (a) H and (b) D components, and (c) relative phase from cross-spectral analysis. In (a) and (b), the stations are color coded as shown at right; vertical dashed red lines identify the dominant spectral peaks. In (c), the H (D) component is shown in black (blue); vertical dashed red line identifies the magnetic latitude of the plasmopause footprint.	47
2.10	LOS Doppler velocities measured by three mid-latitude SuperDARN radars (CVW, FHW and FHE) at 06:04 - 06:06 UT, color coded according to the scale at right with positive (blue-green) values being toward the radar. Three camping beams (blue) of the FHW, FHE and BKS radars operating in THEMIS mode and footprints of THE (blue asterisk) and THD (black asterisk) at the same time are overlaid. The dashed black curve indicates the magnetic latitude of the plasmopause footprint.	49
2.11	Left (Right) panels show time series of Doppler velocity (backscatter power) versus magnetic latitude measured on the camping beams of the FHW, FHE, and BKS SuperDARN radars. Two vertical black lines identify the interval of interest when Pi2 pulsations were observed during the early stages of the substorm.	50
2.12	Latitudinal variation of pulsations observed on the camping beam of the FHE radar: (a) Time series stack plot for range gates 23 - 42; (b) Relative phase versus magnetic latitude; and (c) Spectral power versus magnetic latitude.	51

2.13	Spectral analysis of FHE radar camping beam measurements for (a) range gates 34 - 42 nominally near or poleward of the plasmopause, and (b) range gates 23 - 33 well inside the plasmasphere. Vertical dashed red lines identify the dominant spectral peaks.	52
2.14	Filtered ground magnetic field data between 06:05-06:09 UT from two longitudinal magnetometer chains at $L \sim 3.5$ (upper panels a, b, c) and $L \sim 2.9$ (lower panels d, e, f). Panels (a) and (d) show the H component while panels (b) and (e) show the D component. Panels (c) and (f) are corresponding hodograms with arrows showing the sense of polarization.	54
3.1	Fields of view of seventeen Northern Hemisphere SuperDARN radars in AACGM coordinates. Cyan highlighted beams indicate the camping beams.	69
3.2	Time series of THEMIS mode data measured on beam 6 of the SAS radar on 16 February 2015 from 03:30-04:30 UT: (a) RTI plot of Doppler velocity; (b) Time series of Doppler velocity for range gate 13.	70
3.3	Event examples identified by the automatic detection algorithm using data collected on beam 12 of the PGR radar at 01:00-01:30 UT on 25 January 2016 (left) and beam 6 of the SAS radar at 03:30-04:30 UT on 16 February 2015 (right). (From top to bottom) RTI plots of unfiltered Doppler velocity; RTI plots of median filtered Doppler velocity; time series of filtered Doppler velocity for two particular range gates (red and blue); Lomb-Scargle periodograms of data shown in (c) and (g).	72
3.4	MLAT-MLT maps of ionospheric backscatter occurrence (left), occurrence (middle), and occurrence rate (right) of Pc3-4 (upper panels) and Pc5 events (lower panels).	75

3.5	Frequency distribution of Pc3-4 events. Upper panel (a) shows the histogram of event frequencies while the lower panels show two-dimensional histograms of (b) frequency versus MLT and (c) frequency versus AACGM latitude.	77
3.6	Frequency distribution of Pc5 events. Same format as Figure 3.5.	78
3.7	MLAT-MLT maps of Pc3-4 (upper panels) and Pc5 (lower panels) event occurrence rate at different seasons: summer (left), equinox (middle), and winter (right).	79
3.8	Occurrence rate variation as a function of MLT at specific latitudes color coded by season. Occurrence rate variation of (a) Pc5 at polar latitudes (79-83°), (b) Pc5 at high latitudes (66-74°), and (c) Pc3-4 at midlatitudes (54-62°). Black curves indicate data from all seasons.	80
3.9	MLAT-MLT maps of Pc3-4 event occurrence rate sorted by 0.5 h average AE index (upper panels) and IMF B_Z (lower panels).	81
3.10	MLAT-MLT maps of Pc5 event occurrence rate sorted by 1 h average AE index (upper panels) and IMF B_Z (lower panels).	82
3.11	Time evolution of histograms of average AE index (top row), SYM-H index (middle row), and IMF B_Z (bottom row) for Pc3-4 events at midlatitudes on the nightside (left column), Pc4 (middle column) and Pc5 (right column) events at high latitudes on the duskside. Zero hour indicates the ULF wave event occurrence time. Solid black lines show the median AE (top row), SYM-H index (middle row), and IMF B_Z (bottom row) values. Dashed black lines in the bottom row indicate zero IMF B_Z	83

4.1	Locations of various space and ground instruments. The upper panels show the locations of GOES 13 and 15 (black curve), THE (blue curve) and THD (red curve) spacecraft in (a) the X-Y plane and (b) the X-Z plane in Solar Magnetic coordinates from 20:00 UT on 24 January 2016 to 02:00 UT on 25 January 2016. The lower panel (c) shows the locations of ionospheric footprints of GOES 13 and 15 (black diamonds), THE (blue asterisk) and THD (red asterisk), ground magnetometers (black dots), and SuperDARN radar FOV and camping beams of PGR (cyan), SAS (green), and KAP (orange) in AACGM coordinates at 23:00 UT on 24 January 2016.	96
4.2	Geomagnetic indices and interplanetary parameters covering the wave event: (a) SymH index on 19-28 January 2016; (b) AE (red), AU (green), and AL (blue) indices, (c) OMNI/WIND IMF Bx, By and Bz components in the Geocentric Solar Magnetospheric coordinate system, (d) solar wind speed, (e) solar wind proton density, and (f) solar wind dynamic pressure on 24-27 January 2016. The cyan shaded regions identify the time intervals of interest.	97
4.3	Plasmaspheric context from two THEMIS spacecraft during the recovery phase of the geomagnetic storm. Each panel shows profiles of electron density inferred from spacecraft potential versus L shell value during four successive outbound passes of (a) THD and (b) THE from 23 to 27 January 2016. . . .	98
4.4	The magnetic field data from GOES 13 in the Mean-Field-Aligned coordinate system and the dynamic power spectra from 24 to 27 January 2016. The red (black) vertical lines identify local noon (midnight). The green (yellow) vertical lines identify local dawn (dusk).	100

4.5	The magnetic field data from GOES 15 in the Mean-Field-Aligned coordinate system and the dynamic power spectra from 24 to 27 January 2016.	101
4.6	The dynamic power spectra of electric and magnetic field components in the Mean-Field-Aligned coordinate system from THD (left) and THE (right) at 22:00-23:15 UT on 24 January 2016.	102
4.7	Ionospheric ULF signatures observed by the PGR radar in the camping beam 12 from 2016-01-24/23:00 UT to 2016-01-25/02:00 UT. (a) The range-time intensity plot; (b) Doppler velocity time series from range gate 12 of beam 12; (c) Dynamic power spectrum of data from panel (b); (d) Doppler velocity time series from range gate 8-15 of beam 12.	104
4.8	(Left) The range-time intensity plot for (a) PGR, (b) SAS, and (c) KAP radar from 2016-01-24/20:00 UT to 2016-01-25/04:00 UT. (Right) Frequency versus (d) MLT and (e) magnetic latitude distribution of wave events.	105
4.9	Time series and dynamic power spectra of ground magnetic field northward (B _x) and eastward (B _y) components observed at the SNKQ (left) and FSIM (right) stations from 24 to 26 January 2016.	106
4.10	Frequency distribution as a function of magnetic latitude and MLT for ULF wave events from three high latitude SuperDARN radars, GOES and THEMIS satellites from 2016-01-24/20:00 UT to 2016-01-25/04:00 UT.	108
4.11	(a) The azimuthal electric field from 22:40 UT to 23:10 UT on 24 January 2016 and ion phase space density as a function of energy measured at about (b) 22:45 UT, (c) 22:55 UT, and (d) 23:05 UT by the THE spacecraft.	109

4.12	Time series of magnetic field and energetic ion residual flux data from GOES 13 between 17:20 and 17:50 UT on Jan 25, 2016: (a) radial magnetic field; (b) southward moving energetic ion residual fluxes at $\sim 140^\circ$ pitch angle from detector telescope 9; (c) northward moving energetic ion residual fluxes at $\sim 2^\circ$ pitch angle from detector telescope 7.	113
A.1	Example Lomb-Scargle periodogram analysis: (a) A simulated signal with length of 600 points, wave period of 45 points, wave amplitude of 2, and 4 sinusoidal cycles; (b) Lomb-Scargle periodogram of the simulated signal. The magenta dashed line indicates the NPP is 37.6, the wave frequency is 0.02, and the wave period is 46.	154
A.2	Procedure to derive wave period-dependent threshold NPP. (a) NPP distribution for ($N = 600, T_{sin} = 45, A_{sin} = 2, N_{CYC} = 4$); (b) P_{Cf} (green) and mean NPP (blue) for $N_{CYC} = 1 - 6$ with ($N = 600, T_{sin} = 45, A_{sin} = 2$); (c) Threshold NPP for $A_{sin} = 1 - 10$ with ($N = 600, T_{sin} = 45$); (d) Asymptotic threshold NPP for $T_{sin} = 25 - 100$ with ($N = 600$). See text for details.	155

List of Tables

1.1	Classification of ULF Pulsations	20
1.2	Category, location and source of different types of Pc3-5 oscillations [Anderson, 1994, 1993].	24
2.1	Coordinates of Ground Stations	38
2.2	Cross-spectral and cross correlation analyses of midlatitude Pi2 pulsations (See text for details)	56
3.1	Empirical equations of threshold NPP dependence on wave period with signal length from 66.7% to 133.3% of ideally even sampled length in the Pc3-4 and Pc5 range.	73
4.1	Comparisons of Select Long-Lasting Poloidal ULF Wave Case Studies	117

Chapter 1

Introduction

In this chapter, we present some background material for this dissertation including the Sun-Earth environment, properties of ultra-low frequency (ULF) waves, research objectives, and the dissertation organization.

1.1 The Solar-Terrestrial Environment

In this section, we describe the solar-terrestrial environment starting from the surface of the Sun to the Earth's upper atmosphere including the coupling processes in the geospace environment and geomagnetic disturbances caused by the interaction between matter and electromagnetic fields emitted from the Sun and the Earth's outer atmosphere and magnetic field.

1.1.1 The Sun and Solar Wind

The four fundamental states of matter in physics are solid, liquid, gas, and plasma. We are most familiar with the first three states which are observable or sensible in everyday life. However, the fourth state of matter, plasma, consisting of approximately equal numbers of positively charged ions and negatively charged electrons, is the most ubiquitous in the universe. The Sun, our nearest star, contains 99.86% of the total mass of the solar system.

It is the source of radiation and energy for planets in the solar system. The plasma flow erupting from the Sun and propagating outward is called the solar wind. Embedded in the solar wind is the outward extension of the Sun’s magnetic field, which is termed the interplanetary magnetic field (IMF). In the fluid description, or ideal magnetohydrodynamic (MHD) approximation, the IMF is “frozen-in” to the solar wind plasma as it propagates at speeds of several hundred kilometers per second. Rotation of the Sun gives a spiral shape to the magnetic field lines as the solar wind plasma flows outward named the Parker Spiral [Parker, 1958].

Over an 11-year solar cycle, solar activity waxes and wanes as magnetic field lines that are wound and tangled inside the Sun periodically break through to the surface [Babcock, 1961]. Pairs of sunspots of opposite magnetic polarity that move across the surface of the Sun are produced during this process. Solar magnetic activity associated with sunspots can lead to solar flares, coronal mass ejections (CMEs), and other electromagnetic phenomena that give rise to disturbances in the geospace environment that are known as space weather [Cade III and Chan-Park, 2015].

1.1.2 The Earth’s Magnetosphere

The interaction of the solar wind with the Earth’s magnetic field results in the Earth’s magnetosphere [Kivelson and Russell, 1995] (Figure 1.1). Since the solar wind is propagating at supersonic speed, a structure named the “bow shock” forms in front of the Earth’s magnetosphere that mediates the discontinuous change in plasma properties. The outer boundary of the magnetosphere is named the *magnetopause*; here, the pressure from the Earth’s magnetic field balances the dynamic pressure of the solar wind. The region between the bow shock and magnetopause is named the *magnetosheath*; here, turbulent plasma flow and waves are

commonly observed. The magnetopause is compressed on the dayside by the upstream solar wind pressure while on the nightside it is stretched downstream to form the *magnetotail*. In the equatorial magnetotail, the region of closed field lines with hot and dense plasma is termed the *plasma sheet*.

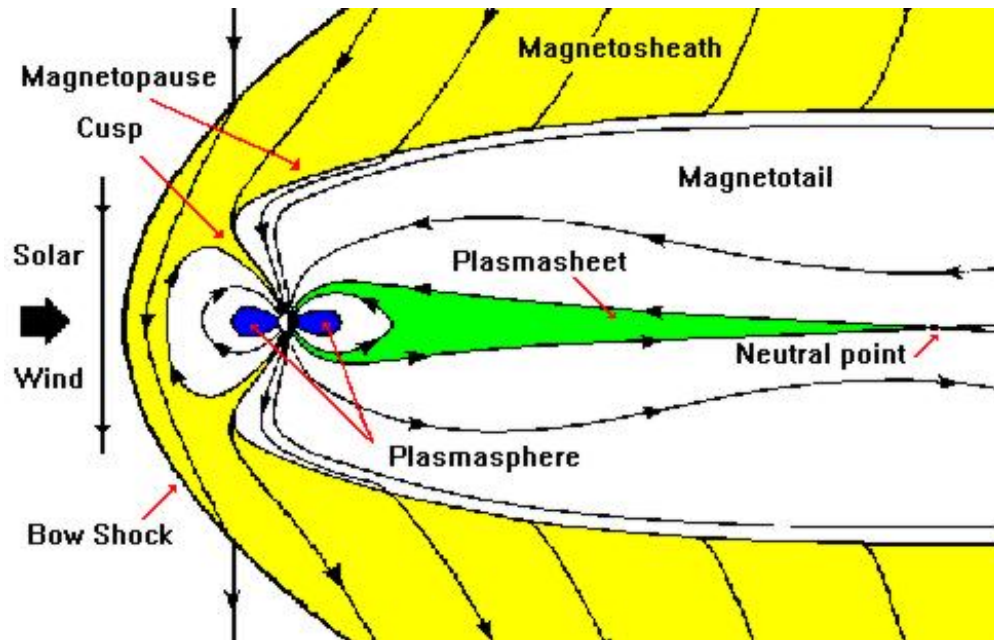


Figure 1.1: The Solar Wind and Earth's Magnetosphere. [Image credit: <https://helios.gsfc.nasa.gov/magnet.html>]

Earth's magnetic field

To first order, Earth's magnetic field resembles that of a magnetic dipole, being essentially horizontal at the ground-level magnetic equator and nearly vertical at the poles. The geomagnetic field plays an important role in coupling the upper atmosphere to the magnetosphere and solar wind. In particular, energetic ions and electrons can travel along magnetic field lines freely and so large-scale perpendicular electric fields map along their full length almost without attenuation. To better understand these processes, we need to review some basic plasma physics of the system. We start with the motion of a charged particle in the

geomagnetic field.

Motion of a Charged Particle in the Geomagnetic Field

There are three basic motions of a charged particle in the geomagnetic field: gyration, bounce, and drift, as shown in Figure 1.2b. A particle typically gyrates about a field line as it moves along its length. Gyrofrequency ($\frac{qB}{m}$) is the angular frequency of the circular motion of a particle in the plane perpendicular to the magnetic field. Bounce motion results when the gyrating particle is reflected from the converging ends of the field line. The locations where the particle is reflected are known as *mirror points*. The angle between the particle velocity vector and the direction of the magnetic field is called the *pitch angle*. This is an important factor for determining whether a particle will be trapped by the geomagnetic field and bounce between two mirror points (Figure 1.2a) or be lost to the Earth's atmosphere.

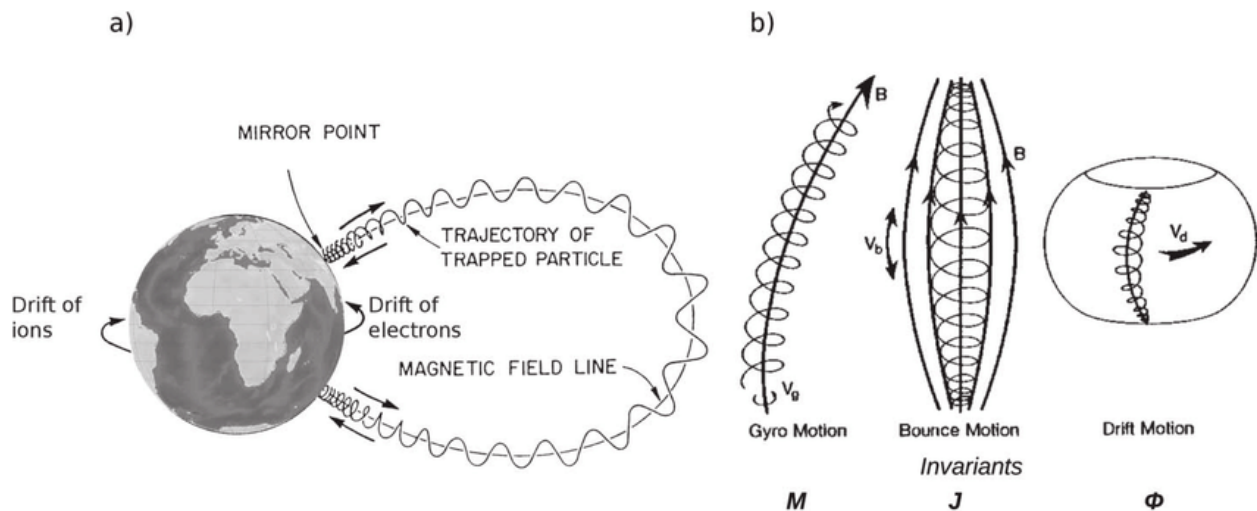


Figure 1.2: Motions of charged particles in the geomagnetic field: (a) schematic representation of the guiding-center trajectory of a trapped charged particle; (b) three cyclic motions: gyro, bounce, and drift. [Regi, 2016]

In addition to gyration and bounce motions, a particle can drift around the Earth in a longitudinal sense. There are three primary drifts to consider in the geomagnetic field:

$\mathbf{E} \times \mathbf{B}$, curvature, and gradient drifts. In the presence of a force other than the magnetic field force, the drift velocity is perpendicular to both the magnetic field and the force and is thus given by:

$$\mathbf{v}_D = \frac{\mathbf{F} \times \mathbf{B}}{qB^2} \quad (1.1)$$

The application of an external electric field force ($\mathbf{F} = q\mathbf{E}$) thus produces an $\mathbf{E} \times \mathbf{B}$ plasma drift with velocity $\mathbf{v} = \frac{\mathbf{E} \times \mathbf{B}}{B^2}$. Since \mathbf{v} is independent of the mass and sign of the charge, ions and electrons move together as bulk plasma motion in the absence of collisions and thus do not create electric current. The $\mathbf{E} \times \mathbf{B}$ drift plays an important role in plasma transport in the magnetosphere and ionosphere. Since the magnetic field in the magnetotail is predominantly northward, a dawn-dusk directed electric field will move plasma Earthward. When the plasma moves to the inner magnetosphere, the curvature and gradient drifts created by the gradient and curvature of the nonuniform geomagnetic field, become dominant. Unlike $\mathbf{E} \times \mathbf{B}$ drift, these drifts cause particles of opposite signs to move in opposite directions, creating current. To be specific, ions (electrons) drift westward (eastward) as shown in Figure 1.2a, creating the east-to-west directed **ring current**, which will be described in more detail in the next subsection.

The inner magnetosphere particle populations

The inner magnetosphere can be treated as a magnetic dipole in which various types of charged particles are trapped by the Earth's intrinsic magnetic field. With ordering of the particle populations by energy and origin, the Earth's inner magnetosphere consists of the ring current, plasmasphere, and Van Allen radiation belts.

Ring current: consists of hot (1-400 keV) and tenuous ions of both ionospheric and solar

wind origins [Daglis et al., 1999], dominates the energy density of the inner magnetosphere. It is located in the equatorial plane at a distance of 3 to 8 Earth radii (R_E) and flows westward around the Earth, thus creating a magnetic field opposite to the Earth's geomagnetic field. Intensification of the ring current leads to characteristic signatures of a geomagnetic storm in the Dst index which will be further described in subsection 1.1.5.

Plasmasphere: is a torus of cold (1-10 eV) and dense ($100\text{-}10000 / \text{cm}^{-3}$) plasma of ionospheric origin, dominates the mass density of the inner magnetosphere. The outer boundary of the plasmasphere, known as the plasmopause, is shown in Figure 1.3 (left) and is defined by an order of magnitude drop in plasma density. The plasmasphere is essentially an extension of the ionosphere (see subsection 1.1.3) at high altitudes that is trapped by the geomagnetic field [Lemaire and Gringauz, 2005].

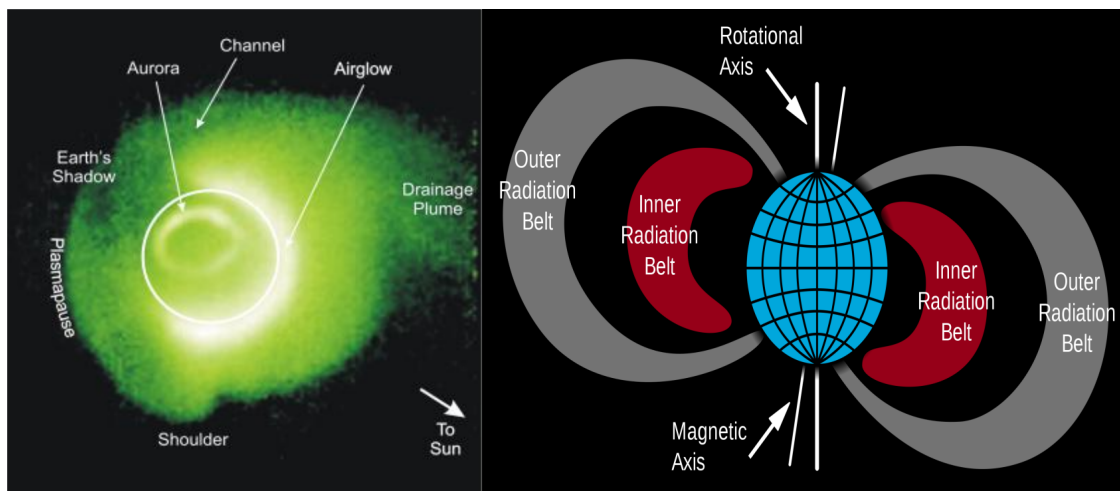


Figure 1.3: Left: Earth's plasmasphere as measured by IMAGE's extreme ultraviolet imager [Sandel et al., 2003]; Right: A cross section of Van Allen radiation belts. [Image credit: NASA]

Radiation belts: were named after James Van Allen, following their discovery in early 1958 by the Explore 1 and Explore 3 satellites [Van Allen et al., 1958, Van Allen and Frank, 1959]. Van Allen radiation belts consist of energetic charged particles originating primarily

from the solar wind with two main belts in a donut shape as shown in Figure 1.3 (right). The inner belt from an altitude of 0.2-2 R_E above the Earth contains mainly protons with energies exceeding 100 MeV. The outer belt consists mainly of 0.4-15 MeV electrons and is more variable than the inner belt as it is more easily influenced by geomagnetic disturbances caused by solar activity. The high-energy particles of the radiation belts pose a hazard to spacecraft and astronauts.

1.1.3 Structure of the Earth's Atmosphere and Ionosphere

Surrounding the Earth is a layer of gases called the atmosphere, commonly known as air. The Earth's atmosphere as retained by gravity is mainly composed of nitrogen ($\sim 78\%$), oxygen ($\sim 21\%$), and argon ($\sim 0.93\%$) with significant contributions by carbon dioxide (0.038%). Water vapor and other gases exist in small amounts as well. The layers of the atmosphere are distinguished by their temperature variation with altitude as shown in Figure 1.4 (left). The surface of the Earth is warmed by sunlight and so the air is heated at ground or sea level and temperature initially drops with altitude.

The lowest layer of the atmosphere is called the troposphere and extends from 0 km to ~ 10 km above the surface of the Earth. The temperature profile (the solid curve in Figure 1.4 (left)) shows that the temperature drops with increasing altitude in the troposphere. This drop is explained by the increasing distance from the source of heating, i.e., the surface of the Earth. Roughly 80% of the mass of Earth's atmosphere and most of the weather and clouds are found in this layer. The upper boundary of the troposphere is the tropopause, where the temperature starts to increase with altitude, producing a temperature inversion, i.e., a region of relatively warm air above a colder one. The increase continues until the stratopause is encountered at 50-55 km altitude. The rise of temperature with increasing

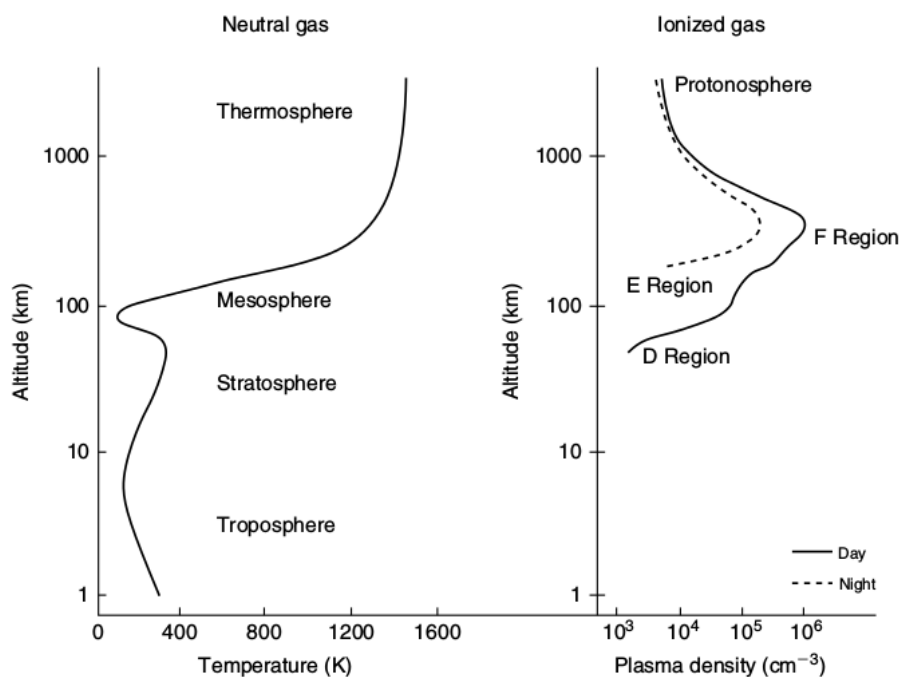


Figure 1.4: Typical profiles of neutral atmospheric temperature (left) and ionospheric plasma density (right) with the various layers designated. [Kelley, 2009]

altitude in the stratosphere is mainly caused by the absorption of ultraviolet (UV) radiation from the Sun by ozone, which peaks as an atmospheric component in the stratosphere. The third layer of the Earth's atmosphere is the mesosphere which extends from the stratopause to the mesopause at an altitude of about 80-85 km. In this layer, temperature drops as the altitude increases due to decreased solar heating and increased cooling by CO_2 radiative emission. The decrease in temperature continues until the mesopause is encountered, which is the coldest part of the Earth's atmosphere. Above the mesopause lies the thermosphere, where the temperature increases dramatically due to the absorption of solar X-ray and a portion of extreme ultraviolet radiation. The radiation causes photoionization of neutral gases and thus creates plasmas that consist of ions and electrons.

The ionosphere is the ionized region of the Earth's upper atmosphere, extending from about

60 km to 1000 km above the Earth's surface. Unlike the neutral atmosphere, whose stratification is controlled by the temperature, ionospheric structure is more organized by plasma density (Figure 1.4 (right)). It is formed due to photoionization of neutral gases by solar radiation. The plasma component becomes increasingly dominant over the background neutral atmosphere with altitude. The ionosphere varies significantly between day and night and it is generally divided into three layers: D, E, F regions.

D-region: altitude range 60-90 km. This layer is mainly produced by Lyman series- α ionization of NO and hard X-ray ionization of O_2 and N_2 . Recombination rates are high in this region, thus the D-region is very weakly ionized and has more neutral gases than charged particles. Due to the high concentration of neutral molecules, this layer causes most absorption of high frequency (HF:3-30 MHz) radio waves, particularly at 10 MHz and below. This explains the disappearance of distant AM broadcast band stations in the daytime. At night, when there is little incident radiation (except for cosmic rays), the D-region almost disappears except at very high latitudes.

E-region: altitude range 90-150 km. Ionization in this region is mainly due to soft X-ray and far ultraviolet solar radiation of O_2 . In addition, photoelectrons and precipitating electrons also make contributions. At night, the E-region weakens due to lack of incident radiation, which results in the height of maximum density increasing.

F-region: altitude range > 150 km. The F-region is the outermost layer with maximum electron density in the ionosphere. This region consists of one layer at night, but splits into two layers during the day. **F1-region:** altitude range 150-200 km. This lower layer is mainly caused by EUV ionization of atomic Oxygen. **F2-region:** altitude range > 200 km. The upper layer usually has highest electron density and consists primarily of O^+ , followed by H^+ at the top and NO^+ and O_2^+ at the bottom. Vertical transport is the primary source of ionization at upper F region altitudes.

1.1.4 The Solar Wind - Magnetosphere - Ionosphere Coupling

Plasma and energy from the Sun are transferred to the Earth's magnetosphere and ionosphere through coupling processes between the solar wind, magnetosphere, and ionosphere. The two most important coupling processes between the solar wind and the magnetosphere are viscous interaction [Axford and Hines, 1961] and magnetic reconnection [Dungey, 1961]. In general, magnetic reconnection dominates in transporting mass, momentum, and energy from the solar wind into the magnetosphere. And it also drives the large scale magnetospheric and ionospheric convection.

Magnetic Reconnection

Magnetic reconnection (or merging) occurs when the magnetic fields from two neighboring regions are anti-parallel. In the Earth's magnetosphere, there are two common sites for magnetic reconnection to occur. As shown in Figure 1.5, when the upstream southward IMF meets the dayside northward geomagnetic field, dayside reconnection occurs. For the magnetotail reconnection, sunward magnetic fields at the northern lobe merge with anti-sunward magnetic fields at the southern lobe. Magnetic reconnection breaks the frozen-in condition and converts magnetic field energy into plasma kinetic and thermal energy. Dayside magnetic reconnection plays an important role in energy transfer from the solar wind to the magnetosphere, while magnetotail reconnection is known to release the energy of the magnetosphere to the ionosphere and atmosphere.

Magnetospheric and Ionospheric Convection

Magnetic reconnection drives plasma convection in the magnetosphere, which is known as the Dungey Cycle [Dungey, 1961]. When dayside reconnection occurs, the IMF and geo-

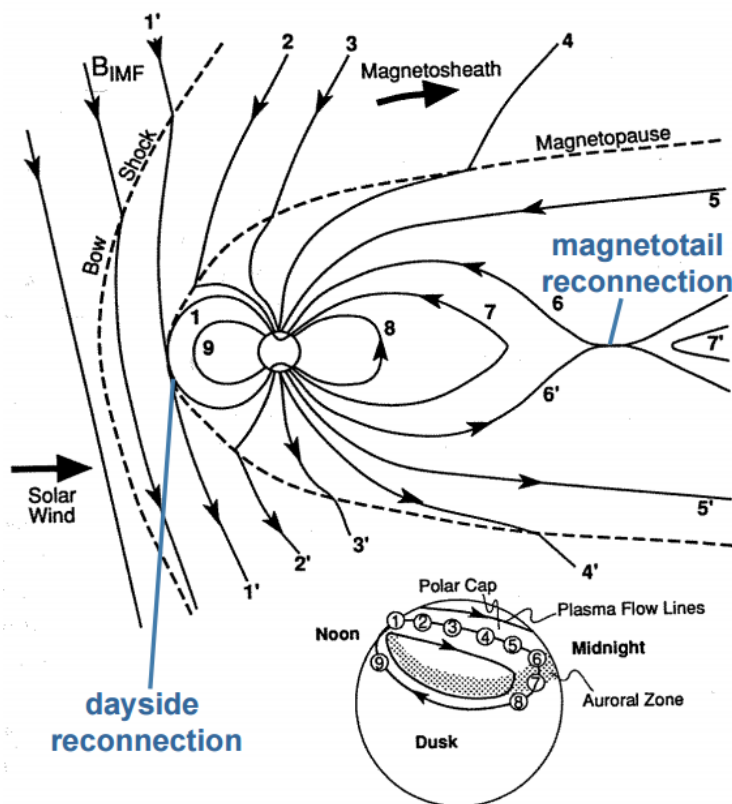


Figure 1.5: Magnetic reconnection in the Earth's magnetosphere and the associated magnetospheric and ionospheric convection. [Adapted from [Kivelson and Russell, 1995](#)]

magnetic fields merge together and form a new topology denoted as 1' in Figure 1.5. The plasma and magnetic field then move together tailward in the sequence from number 2 to 6 until magnetotail reconnection occurs, at which point newly closed field lines move sunward toward the dayside magnetosphere in the sequence from number 7 to 9. The corresponding ionospheric convection is shown in the bottom sketch. From here, we can see how high-latitude ionospheric measurements from ground networks covering relatively small regions can be used to monitor activity over vast regions of the magnetosphere. This approach is much less expensive than using in-situ satellite measurements.

SuperDARN Radars

The Super Dual Auroral Radar Network (SuperDARN) was designed to be a tool for monitoring ionospheric convection over large geographical areas in both hemispheres [Chisham et al., 2007, Nishitani et al., 2019]. It is an international network consisting of 35 low-power HF coherent scatter radars at middle to polar latitudes that look into Earth's upper atmosphere and ionosphere. The radars measure the Doppler shifts of decameter-scale magnetic field-aligned irregularities at F region latitudes in the ionosphere, which are usually caused by $\mathbf{E} \times \mathbf{B}$ drift. Figure 1.6 shows the locations and fields-of-view (FOVs) of 35 currently operational SuperDARN radars in the northern (left) and southern (right) hemispheres. SuperDARN radars from the northern hemisphere are the primary data set used in this dissertation.

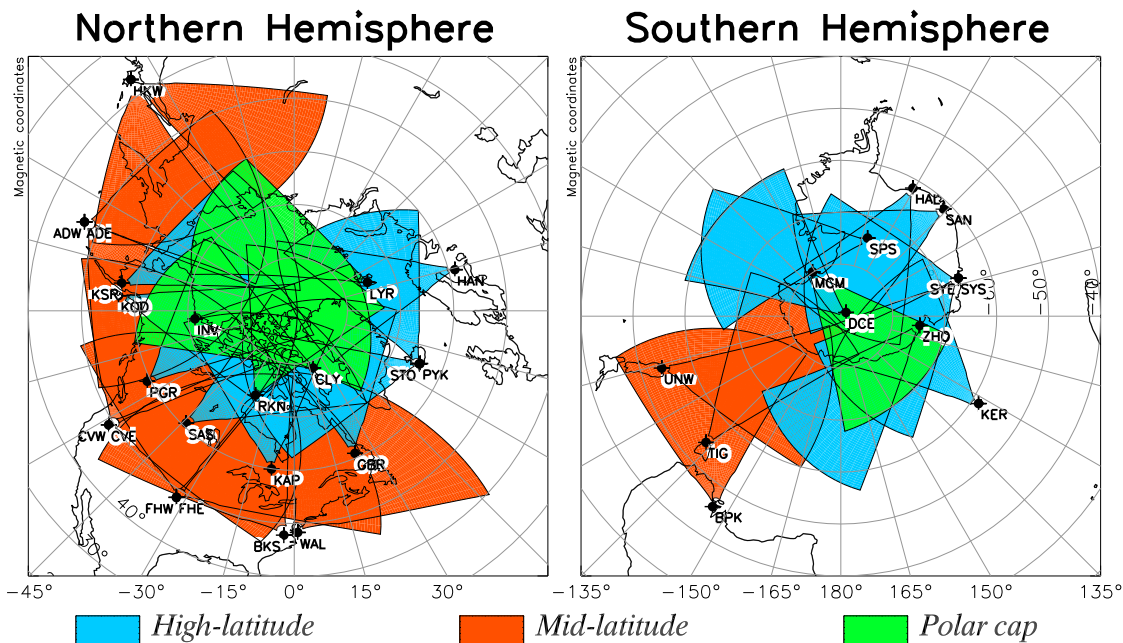


Figure 1.6: Fields of view of 35 currently operational SuperDARN radars from the northern (left) and southern (right) hemispheres in magnetic coordinates. Polar cap, high-latitude, and mid-latitude radar FOVs are shaded green, blue, and red, respectively.

1.1.5 Geomagnetic Activity

Geomagnetic Storm

The most intense manifestation of magnetic reconnection and solar wind - magnetosphere coupling is a geomagnetic storm. Geomagnetic storms are commonly characterized by the Disturbance storm time (Dst) index, which is an hourly measurement derived from four near-equatorial geomagnetic observatories that measure the intensity of the globally symmetrical westward flowing ring current [Sugiura and Kamei, 1991]. Hourly horizontal (H, north-south) component magnetic variations are analyzed to remove annual secular change trends from records of a worldwide array of low-latitude observatories. The Dst index has been used to assess the magnetic storm strength and characterize different storm phases (Figure 1.7). The SYM-H index is a higher resolution (1 min) version of Dst [Iyemori, 1990], which is calculated using different magnetometer stations and slightly different baseline subtraction method. Both indices are designed to measure the intensity of the storm time ring current and are roughly equivalent [Wanliss and Showalter, 2006]. We have used 1-min resolution SYM-H index in this dissertation.

Associated with solar CMEs or coronal holes [Zhang et al., 2007], a geomagnetic storm is caused by a solar wind shock wave which typically strikes the Earth's magnetic field 24 to 36 hours after the solar event. Geomagnetic storms usually begin with storm sudden commencement (SSC), as seen in Dst index suddenly turning positive. The SSC is produced by the arrival of a shock in the solar wind, and followed by a period of enhanced field (the initial phase), and then followed by a period of substantially reduced field (the main phase), which is caused by intensification of the ring current associated with energetic particle injections from the magnetotail and in-situ acceleration processes. When the enhanced solar wind conditions subside and after the Dst index reaches its minimum, the magnetic field

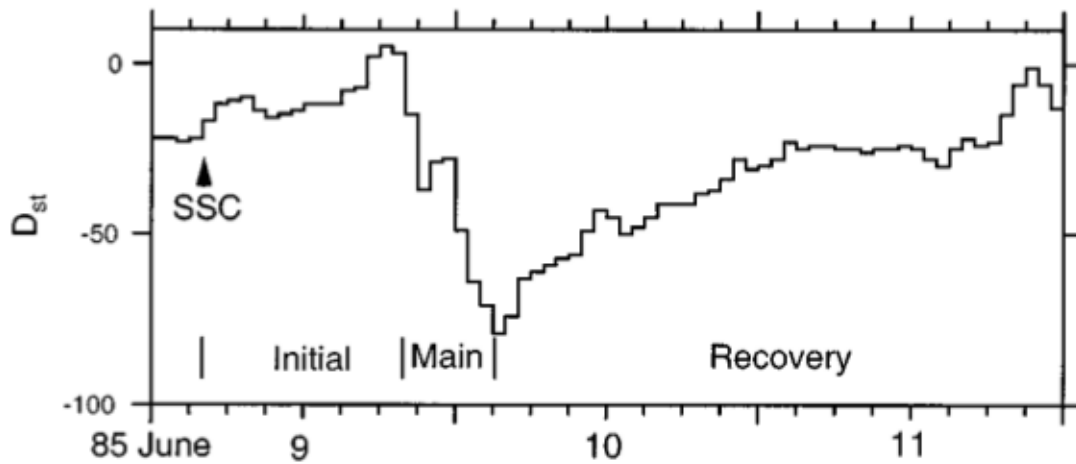


Figure 1.7: The Dst index shows the SSC, initial phase, main phase, and the recovery phase of a classic geomagnetic storm [Lui, 2000].

gradually recovers to its pre-storm condition (the recovery phase). The recovery phase generally takes several days. Figure 1.7 shows the Dst index during a classic geomagnetic storm with the storm phases as described. Note that not all storms have a well defined SSC and initial phase.

Magnetospheric Substorm

The magnetospheric substorm is another mode of geomagnetic activity that is characterized by the auroral electrojet magnetic indices (AE, AU, AL, AO) [Davis and Sugiura, 1966]. They are derived from geomagnetic variations in the H-component observed at 10-13 observatories along the auroral zone in the northern hemisphere. They are designed to provide a global, quantitative measure of auroral zone magnetic activity produced by enhanced ionospheric currents flowing below and within the auroral oval, and thus can be used to characterize substorms. The data are normalized by subtracting a base value for each station, which is calculated at each month by averaging all the data from the station on the five international quietest days. For the normalized data from all the stations as functions of UT, the upper and

lower envelopes of the superposed plots are defined as the AU and AL indices, respectively. The AU (AL) index express the strongest current intensity of the eastward (westward) auroral electrojets. The AE index is the difference between AU and AL, i.e., $AU - AL$, representing the overall activity of the electrojets. The AO index is the mean value of the AU and AL, i.e., $(AU+AL)/2$, representing a measure of the equivalent zonal current.

Substorms are associated with sudden release of the solar wind energy stored within the Earth's magnetotail toward the inner magnetosphere and high latitude ionosphere/atmosphere. They are usually manifested visually by a global development of auroras [Akasofu, 1964]. Substorms can be described by three phases: growth, expansion, and recovery. The growth phase typically begins with the start of an IMF southward turning, during which reconnection occurs at the dayside magnetopause. As magnetic flux is transferred from the dayside to the magnetotail (Figure 1.5), the tail magnetic field lines start to stretch forming a more tail-like field configuration and the central plasma sheet thinning develops. The energy stored in the magnetotail during the growth phase is suddenly released toward the Earth at the onset of the expansion phase, causing sudden auroral brightening and formation of ionospheric currents. The stretched field lines developed during the growth phase relax abruptly to a more dipolar field geometry, a process termed dipolarization. As the expansion phase proceeds, the region of dipolarization, bright aurora and ionospheric currents expand. Recovery phase begins when the poleward expansion of the auroral bulge halts and the intense ionospheric currents and auroral activity gradually die out. There are many theories to explain substorms, however, the actual sequence of processes during a substorm is still an unsolved problem despite more than half a century of research.

1.2 Ultra-Low Frequency Waves

The primary focus of this dissertation is to develop an improved understanding of ULF waves. In this section, we introduce early observations of ULF waves from a historical perspective, the MHD description of ULF waves, the ULF wave definition and categories, and their driving mechanisms.

1.2.1 Historical Background

ULF waves are ubiquitous in the solar-terrestrial environment and have been studied for over a century since the first published account of an observation of a ULF wave in the ground-based measurements of the 1859 great auroral event [Stewart, 1861]. Historically, ULF waves were called micropulsations or geomagnetic pulsations when observed in ground magnetometer data. The name represents how these oscillations were discovered through observations of the end of a very long compass needle with a microscope [McPherron, 2005]. An example of a photographic recording is shown in Figure 1.8.

The existence of electromagnetic-hydromagnetic waves was first pointed out by Alfvén [1942], in which the class of MHD waves now known as Alfvén waves (see next subsection) was described. Hannes Alfvén received the 1970 Nobel Prize in Physics for his work on magnetohydrodynamics. The first physical interpretation of geomagnetic pulsations was proposed by Dungey [1955] almost a century after Stewart’s report when Dungey proposed that these long-period pulsations might be standing Alfvén waves excited on geomagnetic field lines. With the growth in ULF wave research during the 1960’s, Dungey’s standing wave idea was verified by ground magnetometer observations [Nagata et al., 1963, Sugiura, 1961] as well as in space by satellites for the first time [Patel, 1965].

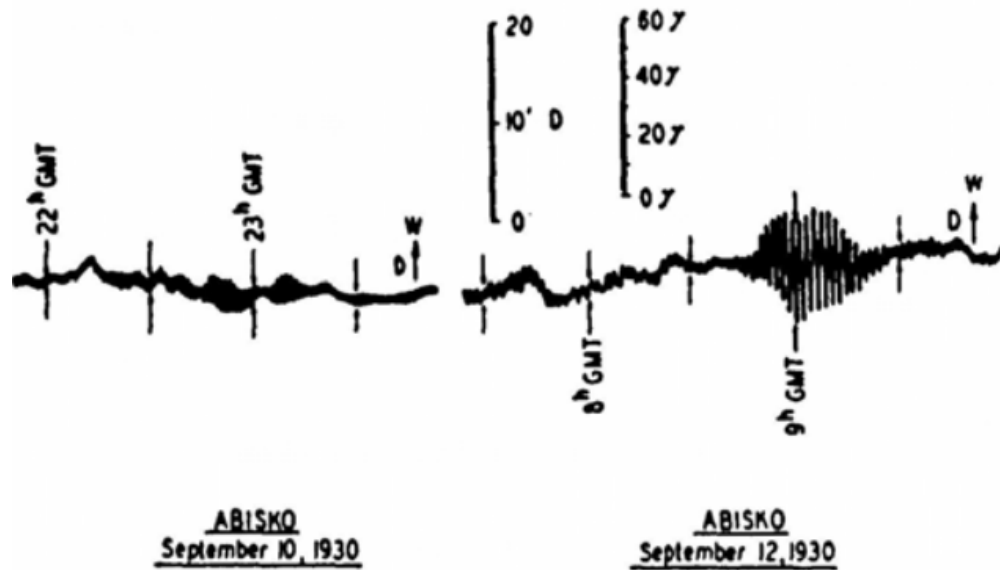


Figure 1.8: An example of a photographic recording of magnetic oscillations of a compass needle. From Figure 1 in [McPherron \[2005\]](#).

In recent years, much attention has been devoted to understanding the role and efficiency of ULF waves in acceleration of magnetospheric particles, particularly in the ring current and radiation belts [e.g., [Zong et al., 2009](#)]. On the one hand, ULF waves driven by external sources from the solar wind can accelerate magnetospheric particles. On the other hand, ULF waves observed on the ground provide a useful diagnostic probe of several magnetospheric properties [[Menk et al., 1999](#)]. Radar and magnetometer observations show that ionospheric parameters, including electron density, ionospheric conductance, and ion temperature, can be significantly modulated by global ULF waves during strong geomagnetic storms [[Pilipenko et al., 2014a](#)]. These effects may modify the Total Electron Content (TEC) along GPS signal paths and result in time delays and phase shifts in signals [[Karatay et al., 2010](#), [Pilipenko et al., 2014b](#)]. Moreover, the ionospheric ULF wave electric field perturbations can cause Joule heating, which in turn affects the temperature of the ionosphere and neutral atmosphere and can lead to thermosphere expansion and then enhanced satellite drag [[Crowley](#)

et al., 1985, Dessler, 1959]. Before we introduce more observations and properties of ULF waves, we review the MHD theory to describe the nature of ULF waves, i.e., MHD waves.

1.2.2 MHD Theory

The magnetosphere can be treated as a cavity of charged particles immersed in the Earth's magnetic field. Ultra-low frequency range covers the frequencies from roughly 1 mHz to several Hz, spanning from the lowest frequencies the magnetospheric cavity can support to the ion gyrofrequencies [Hughes, 1994]. Description of large-scale phenomena can be provided by MHD theory, which treats plasmas as electrically conducting fluids governed by the Navier-Stokes equations of fluid dynamics and Maxwell's equations of electromagnetism. The wave modes derived using MHD theory are called MHD waves. ULF waves are essentially MHD waves, since they have frequencies much smaller than the plasma frequency ($\sqrt{\frac{n_e e^2}{m \sigma_0}}$, the frequency with which plasmas oscillate) and can thus be described by MHD theory. The ideal MHD equations can be combined with the Maxwell's equations to form a closed set of equations:

$$\frac{\partial \rho}{\partial t} + \nabla \cdot (\rho \mathbf{V}) = 0 \quad (1.2)$$

$$\rho \frac{d\mathbf{V}}{dt} + \nabla p - \mathbf{J} \times \mathbf{B} = 0 \quad (1.3)$$

$$\frac{d}{dt} \left(\frac{p}{\rho^\gamma} \right) = 0 \quad (1.4)$$

$$\frac{\partial \mathbf{B}}{\partial t} + \nabla \times \mathbf{E} = 0 \quad (1.5)$$

$$\nabla \times \mathbf{B} - \mu_0 \mathbf{J} = 0 \quad (1.6)$$

$$\mathbf{E} + \mathbf{V} \times \mathbf{B} = 0 \quad (1.7)$$

where ρ is the mass density, \mathbf{V} is plasma bulk velocity field, p is plasma pressure, \mathbf{J} is the current density, \mathbf{B} is magnetic field, \mathbf{E} is electric field, and $\gamma = 5/3$ is the heat capacity ratio. Equation 1.7 is the general Ohm's law with the conductivity $\sigma \rightarrow \infty$, which describes the "frozen-in" condition mentioned before. We assume small perturbations which propagate through a uniform MHD plasma and start by linearizing the above equations and only keep zero and the first order terms. These equations can be combined to give the linearized wave equation:

$$\left[\omega^2 - \frac{(\mathbf{k} \cdot \mathbf{B}_0)^2}{\mu_0 \rho_0}\right] \mathbf{V}_1 = \left[\left(\frac{\gamma p_0}{\rho_0} + \frac{B_0^2}{\mu_0 \rho_0}\right) \mathbf{k} - \frac{(\mathbf{k} \cdot \mathbf{B}_0)}{\mu_0 \rho_0} \mathbf{B}_0\right] (\mathbf{k} \cdot \mathbf{V}_1) - \frac{(\mathbf{k} \cdot \mathbf{B}_0)(\mathbf{V}_1 \cdot \mathbf{B}_0)}{\mu_0 \rho_0} \mathbf{k} \quad (1.8)$$

where \mathbf{V}_1 is the perturbed fluid velocity, \mathbf{k} is the wave vector, and \mathbf{B}_0 is the background uniform magnetic field. Assuming the plane wave solution with $\exp[i(\mathbf{k} \cdot \mathbf{r} - \omega t)]$, the solution to the wave equation gives the dispersion relation:

$$[\omega^2 - k^2 V_A^2 \cos^2 \theta][\omega^4 - \omega^2 k^2 (V_A^2 + C_S^2) + k^4 V_A^2 C_S^2 \cos^2 \theta] = 0 \quad (1.9)$$

where

$$V_A = \frac{B_0}{\sqrt{\mu_0 \rho_0}} \quad (1.10)$$

is the Alfvén speed. $C_S = \sqrt{\frac{\gamma p_0}{\rho_0}}$ is the sound speed, and θ is the angle between \mathbf{k} and \mathbf{B}_0 .

There are three solutions to Equation 1.9, which correspond to three different types of MHD waves: shear Alfvén wave, fast MHD wave, and slow MHD wave. In the cold plasma limit, which lets the sound speed C_S tend to zero, only the shear Alfvén and fast mode exist. The shear Alfvén mode dispersion relation, $\omega^2 = k^2 V_A^2 \cos^2 \theta = k_{\parallel}^2 V_A^2$, shows that the shear Alfvén wave propagates along field lines and can carry a finite field-aligned current but carries no

pressure perturbations since the magnetic perturbations are always perpendicular to \mathbf{B}_0 . On the other hand, the fast mode dispersion relation, $\omega^2 = k^2 V_A^2$, shows that the fast MHD wave propagates isotropically. The fast mode has a component of magnetic perturbations parallel to \mathbf{B}_0 . It can thus transmit pressure variation and is also called a compressional mode.

1.2.3 Definition and Category

ULF waves are MHD waves in the frequency of 1 mHz to a few Hz. ULF pulsations are divided into two main types: pulsation continuous (Pc), which means quasi-sinusoidal waves lasting more than several cycles, and pulsation irregular (Pi), which means broad band or short-lived pulsations. They are further split into several subclasses (see Table 1.1) according to the wave period or frequency [Jacobs et al., 1964]. Each type was originally associated with morphological characteristics, but with the emergence of new observations particularly from spacecraft, this classification has become primarily an indication of frequency bands. However, a prominent exception is the Pi2 pulsations, which have long been recognized to be associated with substorms and auroral brightenings [Hughes, 1994].

Table 1.1: Classification of ULF Pulsations

Continuous Pulsations			Irregular Pulsations		
Type	Period (s)	Frequency	Type	Period (s)	Frequency
Pc1	0.2 - 5	0.2 - 5 Hz	Pi1	1 - 40	0.03 - 1 Hz
Pc2	5 - 10	0.1 - 0.2 Hz	Pi2	40 - 150	7 - 25 mHz
Pc3	10 - 45	22 - 100 mHz			
Pc4	45 - 150	7 - 22 mHz			
Pc5	150 - 600	1 - 7 mHz			

According to their polarization, ULF waves are categorized into three modes: compressional mode ($B_{//}, E_\varphi$), poloidal mode (B_r, E_φ), and toroidal (B_φ, E_r) mode. Here, B_r (E_r) is the radial, $B_{//}$ is the parallel or compressional, and B_φ (E_φ) is the azimuthal components in a local magnetic field system. Considering MHD waves in a more realistic dipole magnetic

field geometry [Allan and Knox, 1979, Singer et al., 1981], shear Alfvén waves in the Earth’s magnetosphere can be split into the toroidal and poloidal modes (Figure 1.9). They are usually coupled for a finite azimuthal wavenumber (i.e., $0 < |m| < \infty$), which is defined as the number of wave cycles surrounding the Earth in the azimuthal direction. The m value is also a good indicator of the wave driving source, which will be described in Section 1.2.4.

Field Line Resonances

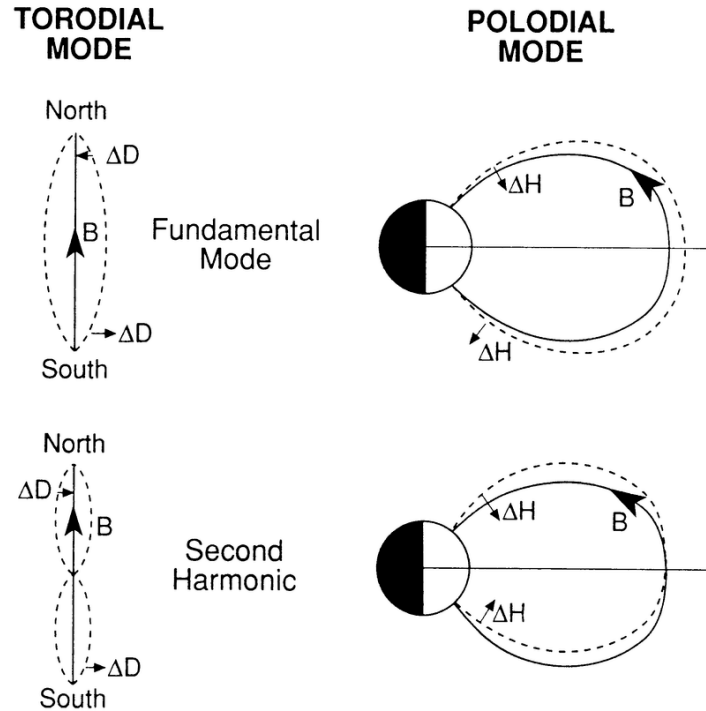


Figure 1.9: Fundamental (top) and second harmonic (bottom) perturbations looking earthward at a field line stretched from north to south for toroidal modes (left) and sketched in a meridional plane for poloidal modes (right) [Hughes, 1994]. ΔH and ΔD refer to north-south and east-west perturbations, respectively.

One prominent category of ULF pulsations is the field line resonance (FLR), which is a standing Alfvén wave on closed magnetic field lines analogous to vibrations on a stretched string. The fundamental and second harmonic toroidal (left) and poloidal (right) FLRs are

shown in Figure 1.9. Note that for the fundamental mode (top), the poloidal mode magnetic perturbations (ΔH) are in phase whereas the toroidal mode perturbations (ΔD) are out of phase. The opposite is true for the second harmonic mode (bottom). The fundamental period of a FLR or the eigen-frequency of a magnetic field line is determined by the length of the field line (l) and the Alfvén velocity along it:

$$T = 2 \int \frac{dl}{V_A} \quad (1.11)$$

Cavity/Waveguide Mode

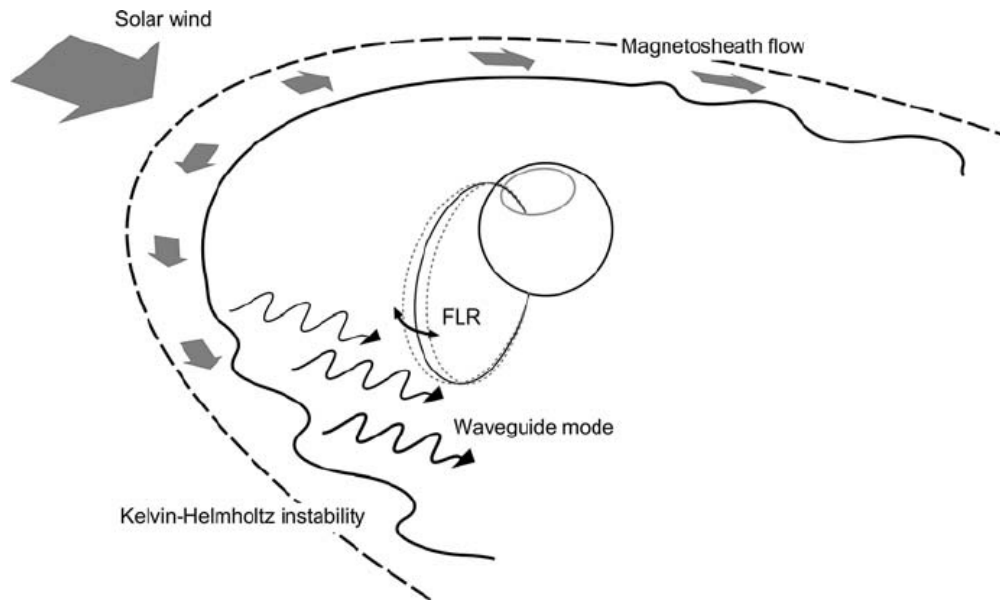


Figure 1.10: A schematic representation of the generation of a FLR by compressional waves of the waveguide mode excited via the Kelvin-Helmholtz instability at the magnetopause. [Adapted from [Rae et al., 2008](#)]

Another category of ULF waves is the cavity mode resonance. Boundaries of plasma mass density (e.g. magnetopause and plasmapause) inside the magnetosphere form cavities which can resonate in response to different driving sources [[Kivelson and Southwood, 1985](#)]. In effect, the magnetospheric or plasmaspheric cavity as a whole can “ring” at its own natural

eigen-frequencies analogous to striking a bell. However, due to the existence of the magnetotail, the magnetosphere is more like a wave-guide than a cavity, such that wave modes can be standing radially but propagating azimuthally and hence potentially lost down the tail. The cavity/waveguide mode is essentially the fast or compressional mode. They can be driven by various external sources such as interplanetary shocks [Takahashi et al., 2018a] and Kelvin-Helmholtz instability occurring when there is a velocity difference across the magnetopause [Miura, 1992]. The compressional waves are coupled to shear Alfvén waves when the cavity mode eigen-frequency matches the field line eigen-frequency and generate the FLRs as shown in Figure 1.10.

1.2.4 Driving Mechanisms

Extensive studies of ULF waves have been conducted using ground-based and space-borne measurements which improve our understanding of pulsation occurrence statistics and source mechanisms. While it has not been conclusively determined, a number of authors have postulated numerous possible excitation mechanisms for ULF waves, which are summarized in Table 1.2. For example, it has been shown that band-limited Pc3 pulsations are most often observed on the dayside and have an upstream source in the foreshock and magnetosheath, whereas poloidal Pc4 are most often seen in the afternoon sector and related to energetic particle injections [e.g., Shi et al., 2018a]. By contrast, compressional Pc5 waves are usually observed on the nightside and the flanks of the magnetosphere and are generally related to local sources such as the drift mirror instability in high β plasma [Hasegawa, 1969], where $\beta = \frac{p}{p_{mag}} = \frac{nK_B T}{B^2/(2\mu_0)}$ is the ratio of the plasma pressure to the magnetic pressure. Finally, toroidal Pc5 waves of fundamental mode FLRs are more often seen at the dawn and dusk flanks and are often associated with external driving sources, such as variations in the solar wind dynamic pressure and Kelvin-Helmholtz waves at the magnetopause. The external

driving waves mostly propagate anti-sunward with low azimuthal wave numbers while the internal sources are expected to generate sunward propagating poloidal waves with high azimuthal wave numbers. We summarize common external and internal driving sources in the following subsections.

Table 1.2: Category, location and source of different types of Pc3-5 oscillations [Anderson, 1994, 1993].

Category	Location	Source	Note
Compressional Pc3	dayside	upstream	ion cyclotron instability
Toroidal Pc3	dayside	upstream	FLR harmonics
Poloidal Pc4-5	afternoon, evening	local	related to particle injections
Compressional Pc5	nightside, dawn and dusk	local	related to high β plasma
Toroidal Pc5	dawn and dusk flanks	upstream	fundamental mode FLRs
Incoherent noise	everywhere	unknown	increases with magnetic activity

External Sources

The excitation of toroidal Pc5 pulsations are mainly due to external sources, i.e., energy source from the solar wind, magnetosheath, or magnetopause/boundary layer. Coherent oscillations in solar wind parameters can penetrate into the magnetosphere and directly drive ULF waves inside the magnetosphere [Kepko and Spence, 2003]. ULF waves can also be generated by buffeting of the magnetosphere in response to solar wind pressure perturbations, such as positive or negative dynamic pressure pulses [Zhang et al., 2010]. More recently, it has been shown that ion foreshock transients, such as hot flow anomalies, are important driving sources for compressional Pc5 waves and FLRs in the magnetosphere and ionosphere [Hartinger et al., 2013, Shen et al., 2018, Wang et al., 2018]. As mentioned before, Kelvin-Helmholtz instability [Miura, 1992] in the magnetosphere flanks is another external source for ULF wave generation. The generated compressional waves (waveguide mode) can be coupled to shear Alfvén waves (FLRs) as shown in Figure 1.10. The external

driving waves are mostly compressional and toroidal modes with low azimuthal wave numbers and propagating anti-sunward.

Internal Sources

Magnetospheric ULF waves can arise from various sources that are internal to the magnetosphere, such as localized instabilities [e.g., [Chen and Hasegawa, 1991](#), [Southwood and Kivelson, 1993](#)] and wave-particle interactions (see review by [Zong et al. \[2017\]](#)). The drift-bounce resonance [[Southwood et al., 1969](#)], a wave-particle interaction process involving the particle drift and bounce motions (Figure 1.11), is the focus of this dissertation and is identified as the driving mechanism of a long-lasting poloidal ULF wave event that will be described in Chapter 4.

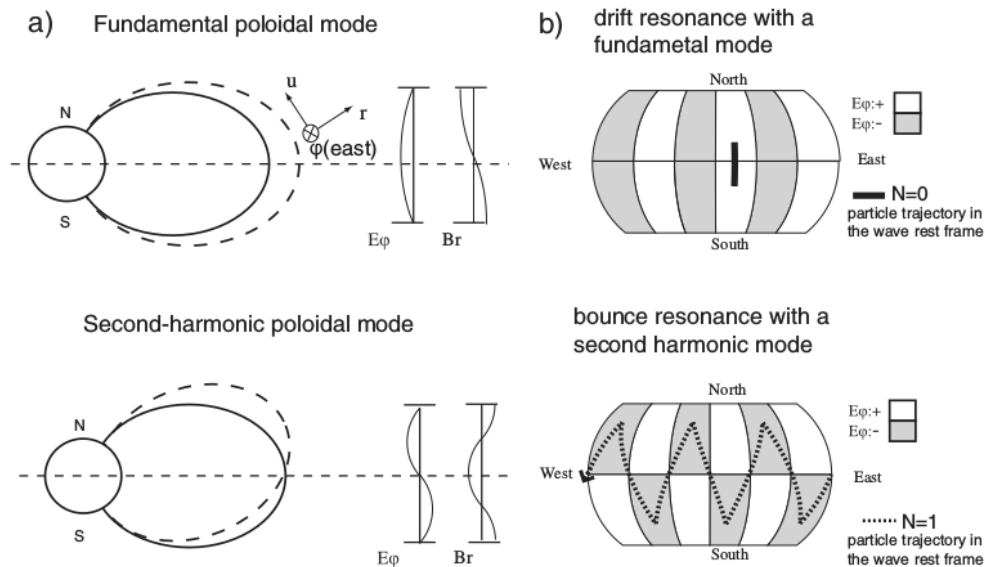


Figure 1.11: A schematic representation of standing poloidal Alfvén waves and wave-particle resonance interactions [[Dai et al., 2013](#)].

Since the azimuthal electric field associated with poloidal waves is aligned with the particle drift motion in the Earth's magnetosphere, a wave-particle interaction can occur.

Specifically, this drift-bounce resonance occurs when the wave frequency (ω_{wave}), particle drift frequency (ω_d) and bounce frequency (ω_b) meet certain resonance condition (e.g., $\omega_{wave} - m\omega_d = N\omega_b$). Figure 1.11 (top) illustrates the drift-resonance of a particle with a fundamental poloidal mode (E_ϕ anti-node and B_r node at the magnetic equator). Figure 1.11 (bottom) illustrates the bounce-resonance of a particle with a second-harmonic poloidal mode (E_ϕ node and B_r anti-node at the magnetic equator). Free energy for wave generation may come from a non-Maxwellian particle distribution which can be created by processes such as particle injections during substorms. These sources are expected to generate high- m waves, which are easily screened by the ionosphere [Hughes and Southwood, 1976], thus not well detectable by ground magnetometers.

Observations and modeling have shown that any of these mechanisms can be viable under certain conditions; however, positively identifying a source mechanism has proven to be rather difficult due to limitations in spatial coverage and temporal resolution of measurements. In-situ spacecraft measurements can help identify wave properties such as polarization and Poynting vector. And particle data from spacecraft if available can be used to examine wave-particle interaction signatures. However, it is very difficult to estimate the wave spatial distribution and propagation using limited spacecraft measurements. Multi-point SuperDARN high-time resolution data are a great tool for estimating the wave spatial extent and ionospheric electric fields in the Pc4-5 frequency range from the sub-auroral region to the polar cap. We make use of SuperDARN high-time resolution data as well as spacecraft-SuperDARN conjunctions for ULF wave studies in this dissertation.

1.3 Objectives and Dissertation Organization

This dissertation seeks to characterize the ionospheric ULF wave activities on a broad range of spatial and temporal scales and to understand the fundamental processes that drive them. The broad objective of this dissertation is to utilize the SuperDARN high-time resolution data to study the occurrence statistics of ionospheric ULF waves over a broad frequency range as well as extensive spatial and temporal coverage and their driving mechanisms. We propose to address the following science questions:

- 1) What is the occurrence probability of ionospheric ULF waves as a function of frequency, location (dayside/nightside; polar cap/high-latitude/mid-latitude), solar wind condition, geomagnetic activity level, and season?
- 2) What are the primary driving mechanisms of ionospheric ULF waves?

Answers to these science questions help us to understand the role of ULF waves in coupling energy and momentum from the solar wind to the magnetosphere and ionosphere and can provide better constraints on where and when they occur and how they affect magnetospheric particle dynamics. Research presented in this dissertation might conceivably improve future space weather forecasts because ULF waves are important for modulating energetic particle precipitation and accelerating radiation belt particles to relativistic energies and hence creating space weather hazards.

This dissertation is organized in five chapters. Chapter 1 has introduced the solar-terrestrial environment, ULF waves, data sets, and research objectives. Chapter 2 will present a case study of simultaneous observations of Pi2 pulsations from spacecraft, midlatitude SuperDARN radars, and ground magnetometers to characterize the pulsation properties and investigate the generation mechanism. Next, Chapter 3 will consider the statistical characterization of ionospheric ULF wave signatures in terms of spatial occurrence, frequency

characteristics, seasonal effects, and dependence on solar wind and geomagnetic conditions, using high-time resolution SuperDARN data from the northern hemisphere. Chapter 4 will report a long-lasting poloidal wave via multi-point observations of satellite and high-latitude SuperDARN conjunctions. Finally, Chapter 5 will summarize the conclusions and ideas for future work.

Chapter 2

Simultaneous Space and Ground-Based Observations of a Plasmaspheric Virtual Resonance

X. Shi¹, J. B. H. Baker¹, J. M. Ruohoniemi¹, M. D. Hartinger¹, N. A. Frissell², and Jiang Liu³

¹Department of Electrical and Computer Engineering, Virginia Tech, Blacksburg, VA, USA.

²Center for Solar-Terrestrial Research, New Jersey Institute of Technology, Newark, New Jersey, USA.

³Department of Earth, Planetary and Space Sciences, Institute of Geophysics and Planetary Physics, University of California, Los Angeles, California, USA.

Shi, X., Baker, J. B. H., Ruohoniemi, J. M., Hartinger, M. D., Frissell, N. A., and Liu, J. (2017), Simultaneous space and ground-based observations of a plasmaspheric virtual resonance, *J. Geophys. Res. Space Physics*, 122, 4190–4209, doi:10.1002/2016JA023583.

Abstract

We present simultaneous space and ground-based observations of Pi2 pulsations which occurred during a substorm on 25 September 2014. The timeline for this event starts at \sim 06:04 UT when the THEMIS probe D located inside the plasmasphere detected Pi2 pulsations in the electric and magnetic fields. Cross-spectral analysis shows the azimuthal electric field and compressional magnetic field oscillated nearly in quadrature, highly suggestive of a standing fast-mode wave. Simultaneous Pi2 observations from dayside and nightside ground magnetometers at low latitudes indicate a global wave mode. A latitudinal magnetometer chain on the nightside observed a phase reversal in the H component of the Pi2 pulsations when crossing the footprint of the plasmopause, estimated from THEMIS spacecraft measurements. Spectral analysis of data from ground magnetometers in this latitudinal chain showed fundamental and second harmonic spectral peaks in their H and D components. Similar pulsation signatures at comparable harmonic frequencies were observed by three mid-latitude SuperDARN HF radars, both poleward and equatorward of the plasmopause ionospheric footprint. Finally, the longitudinal polarization pattern and azimuthal phase propagation of mid-latitude Pi2 pulsations are consistent with previous observations of a plasmaspheric virtual resonance being excited by a longitudinally localized source near midnight.

2.1 Introduction

As a subclass of ultra-low frequency (ULF) waves, Pi2 pulsations are short-duration (5-15 min) damped geomagnetic field oscillations with periods of 40-150 s. These pulsations are mainly observed on the Earth's nightside and are often associated with substorm onset or auroral intensification [Liou et al., 2000, Rostoker et al., 1980] but have also been

observed during quiet geomagnetic conditions [Kwon et al., 2013, Sutcliffe, 1998]. Despite extensive studies for more than half a century, there is still no consensus on the generation mechanisms of Pi2 pulsations [Keiling and Takahashi, 2011]. At higher latitudes, Pi2 pulsations have larger amplitudes with a maximum in the auroral zone, irregular waveforms, and longer periods. At lower latitudes, they have smaller amplitudes, more regular damped sinusoidal waveforms, and shorter periods. Most high-latitude Pi2 pulsations are believed to be caused by Alfvén waves associated with the transient response of the substorm current wedge [Baumjohann and Glaßmeier, 1984] while low-latitude Pi2s are often attributed to cavity mode resonance [Kivelson and Southwood, 1985, Saito and Matsushita, 1968]. An outstanding open question concerns the generation mechanisms of Pi2s at mid-latitudes, especially pulsations observed near the plasmopause, where there is a marked transition between high- and low- latitude Pi2 pulsations [Teramoto et al., 2016].

Many studies have investigated Pi2 pulsations with ground-based or satellite-borne instrumentation [e.g., Fukunishi, 1975], and sometimes both [e.g., Keiling et al., 2008]. Several events have provided clear evidence of the Plasmaspheric Cavity Resonance (PCR) as a source of middle and low latitude Pi2 pulsations observed on the ground [Sutcliffe and Yumoto, 1991] and inside the plasmasphere by spacecraft [Luo et al., 2011, Takahashi et al., 1995]. Theoretical modeling [Allan et al., 1996] and numerical simulations [Zhu and Kivelson, 1989] suggest that low latitude Pi2 pulsations are generally cavity modes and should be generally confined to the plasmasphere. Due to their global extent, the PCR-associated Pi2 pulsations can be observed simultaneously over a wide range of magnetic local times (MLTs), including on the dayside.

An alternative to the PCR model is the Plasmaspheric Virtual Resonance (PVR) model [Lee and Kim, 1999, Lee and Lysak, 1999], in which wave energy is primarily confined to the plasmasphere but a small portion escapes beyond the plasmopause. This results in a

lowered but finite Pi2 amplitude outside the plasmasphere that decreases with distance. However, depending on the Alfvén speed profile, the amplitude of the Pi2 pulsations in the PVR model can sometimes increase immediately outside the plasmasphere [Takahashi et al., 2003]. Observational evidence for the PVR model was recently provided by Ghamry et al. [2015], who reported simultaneous Pi2 observations by the Van Allen Probes inside and outside the plasmasphere and earlier by Kim et al. [2005] and Teramoto et al. [2008]. Since the PCR and PVR models both invoke system eigenmodes of the plasmasphere, they share the characteristics of radially standing waves constrained by the plasmopause.

Pi2 pulsations can also be detected in the ionosphere by High Frequency (HF; 3-30 MHz) and Very High Frequency (VHF; 30-300 MHz) radars [Gjerloev et al., 2007]. The ionosphere is the region where transfer of wave energy from the magnetosphere to the upper atmosphere mainly occurs. In addition, the ionosphere controls the detectability, polarization, and decay of low frequency magnetohydrodynamic (MHD) waves [Ponomarenko and Waters, 2013]. Taking account of the modulating effect of the ionosphere is thus necessary when comparing spacecraft data with ground magnetometer observations. The first radar observations of ionospheric Pi2 pulsations near the plasmopause were made by Frisell et al. [2011] using the Blackstone radar of the Super Dual Auroral Radar Network (SuperDARN) [Chisham et al., 2007, and references therein]. These observations supported the Direct Response Bursty Bulk Flow model (DR-BBF), in which ground instruments directly sense compressional waves generated by BBF braking [Kepko and Kivelson, 1999]. By contrast, Teramoto et al. [2014] compared SuperDARN Hokkaido radar Pi2 observations with theoretical predictions and suggested that a cavity mode together with the contribution of an Alfvén wave can account for some mid-latitude Pi2s. More recently, Teramoto et al. [2016] used multipoint observations from three mid-latitude SuperDARN radars, three Time History of Events and Macroscale Interactions During Substorms (THEMIS) satellites, and ground magnetometers

to study the latitudinal dependence of Pi2 frequency near the plasmapause. They suggested that compressional waves can propagate duskward away from the midnight sector where the harmonic cavity mode is generated.

Despite numerous previous studies which have used both ground- and space-based instruments to analyze Pi2 pulsations at high, middle, and low latitudes, controversy remains regarding their origins. This can be partially attributed to the fact that comprehensive analysis of any particular Pi2 event requires extensive coverage in both latitude and local time to fully distinguish between competing theories. Indeed, it is a rare occurrence to have sufficient instrumental coverage to definitively determine the dominant wave mode characteristics of a Pi2 event, let alone its most likely driver. In addition, only a few studies have been able to investigate Pi2 pulsations using both space-borne and ground-based platforms in the vicinity of the plasmapause and its ionospheric footpoint [Frissell et al., 2011, Teramoto et al., 2016]. In this study, we analyze a Pi2 event that had sufficient coverage by ground- and space-based datasets in fortuitous locations to definitively determine its dominant wave mode characteristics. Specifically, two THEMIS spacecraft provided measurements of electromagnetic fields both inside and outside the plasmasphere while three mid-latitude SuperDARN radars provided high resolution latitudinal profiles of the ionospheric electric field straddling the plasmapause footpoint location. Also, broadly distributed ground magnetometers provided context regarding the global nature of the pulsations, as well as their amplitude and spectral characteristics inside and outside the plasmapause. Our analysis of these various datasets leads us to conclude that this particular Pi2 event is consistent with a predominant PVR mode being excited by a longitudinally localized source near midnight. To our knowledge, this is the first such study to definitively identify a PVR in measurements.

The paper is structured as follows: section 2 describes the ground- and space-based data sets; section 3 presents the observations and data analysis; section 4 discusses the observations

and results in the context of the PCR and PVR models; and finally, section 5 states the conclusions.

2.2 Data Sets

The primary data sets used in this study are magnetic and electric field observations from the THEMIS spacecraft, SuperDARN radar measurements of ionospheric convection, and widespread ground magnetometer data. The preparation of these data are described in the following subsections.

2.2.1 THEMIS Spacecraft

Data from THEMIS [[Angelopoulos, 2008](#)] D and E (THD and THE, respectively) spacecraft were used in this study to characterize the nature of the Pi2 pulsations inside and outside the plasmasphere. The magnetic field data came from the Fluxgate Magnetometer (FGM) instrument [[Auster et al., 2008](#)]. For studying magnetic oscillations, the FGE data (engineering, 8 Hz) were used to reduce digitization noise in the sub-nanotesla range. During the time period of interest, FGE data have the highest time resolution of any FGM data product, and, when averaged, appear similar to other lower resolution FGM data. The electric field and spacecraft potential data were obtained from the Electric Field Instrument (EFI) [[Bonnell et al., 2008](#)]. The electric field data are spin-fit, 3 s averaged vector samples constructed from spin-plane components by assuming no electric field along background magnetic fields. The EFI is affected by several sources of contamination which can be checked if the spacecraft is in fast survey mode. Although THD was in slow survey mode just before the interval of our interest, no contamination was found at 06:21 UT on 25 September 2014 when THD

entered fast survey mode. This suggests that the electric field measurements made during the interval of interest (~ 10 - 20 minutes earlier) were clean.

Magnetic and electric fields were expressed in local mean-field-aligned (MFA) coordinates with components denoted as B_x (outward, perpendicular to the mean magnetic field), B_y (eastward, perpendicular to the mean magnetic field), and B_z (parallel to the mean magnetic field) [Takahashi et al., 1990]. We first averaged the FGE data into 3 s intervals to keep the same time resolution with the EFI data, then took a boxcar running average over 300 s to get the mean magnetic field. After rotating to the MFA coordinate system, the magnetic and electric field oscillations were obtained by (i) subtracting the 300 s averaged background magnetic field data from the 3 s averaged magnetic field data, and, (ii) high-pass filtering with 150 s period.

2.2.2 SuperDARN Radars

SuperDARN HF radars measure the line-of-sight (LOS) velocity component of the F-region drift of ionospheric plasma when decameter-scale electron density irregularities are present and oriented favorably to produce backscatter. The irregularity motion is due to $\mathbf{E} \times \mathbf{B}$ drift, where \mathbf{E} is the ionospheric electric field and \mathbf{B} is the geomagnetic field. When ULF waves pass through the ionosphere, the associated electric field imposes an oscillation in the Doppler velocity component measured by HF radars. The mid-latitude radars provide an extension of the global SuperDARN network to $\sim 50^\circ$ magnetic latitude (MLAT) [Baker et al., 2007]. Normally, the SuperDARN radars are scheduled for 1-min or 2-min azimuthal sweeps in the “normalscan” mode, but sometimes they are scheduled to operate in a special mode called “THEMIS” mode. Every radar operating in THEMIS mode includes a camping beam sampled at a higher rate (\sim once every six seconds) by interleaving soundings on the

camping beam with successive beams of the normal azimuthal scan. The step in azimuth between adjacent beams of the radar is $\sim 3.3^\circ$. The range resolution in the measurements is ~ 45 km. For this study, THEMIS mode data from three mid-latitude SuperDARN radars - Fort Hays West (FHW), Fort Hays East (FHE), and Blackstone (BKS) - were used to analyze ionospheric Pi2 signatures.

2.2.3 Other Data Sets

Ground magnetometers from the following networks were used to analyze Pi2 ground signatures: THEMIS [Mann et al., 2008, Russell et al., 2008], Institute for Space-Earth Environmental Research (ISEE), and INTERMAGNET. The original 0.5 s or 1 s sampled ground magnetometer data were first detrended, then resampled at exactly 1 s time step and high-pass filtered with 150 s period. The interplanetary and geomagnetic data from the OMNI database [King and Papitashvili, 2005] and the World Data Center for Geomagnetism were used to provide context regarding the interplanetary and geomagnetic conditions of this event.

The locations of the various space and ground instruments used in this study are shown in Figure 2.1. The upper panels show the locations of the THE and THD spacecraft in the X-Y plane (Figure 2.1a) and X-Z plane (Figure 2.1b), respectively, in Solar Magnetic (SM) coordinates. The asterisks identify the locations of the satellites at 06:04 UT and the start of the interval when THD started to see Pi2 pulsations. The curves of spacecraft locations end at 06:45 UT. The lower panel (Figure 2.1c) shows a map in Altitude Adjusted Corrected Geomagnetic (AACGM) coordinates [Baker and Wing, 1989] with the positions of the space and ground instruments indicated. Included are selected nightside ground magnetometers (black dots); four THEMIS all-sky imagers (green dots); SuperDARN radar

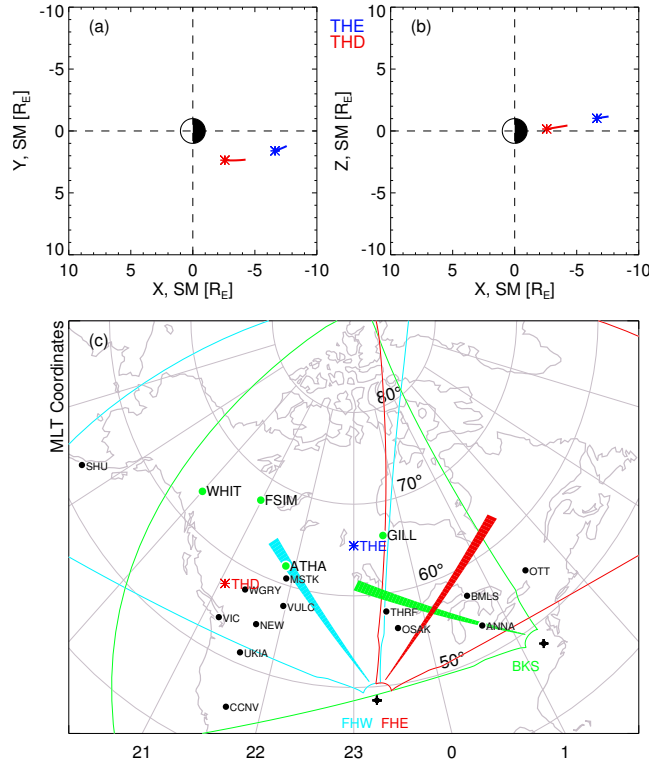


Figure 2.1: Locations of various space and ground instruments. The upper panels show the locations of THE (blue curve) and THD (red curve) spacecraft in (a) the X-Y plane and (b) the X-Z plane in SM coordinates. The asterisks identify the starting time at 06:04 UT on 25 September 2014. The lower panel (c) shows the locations of ionospheric footprints of THE (blue asterisk) and THD (red asterisk), ground magnetometers (black dots), THEMIS all-sky imagers (green dots), and SuperDARN radar FOV and camping beams of FHW (cyan), FHE (red), and BKS (green) in AACGM coordinates at 06:04 UT.

fields of view (FOV) and camping beams of FHW (cyan), FHE (red), and BKS (green); and ionospheric footprints of THE (blue asterisk) and THD (red asterisk) using the Tsyganenko 96 (T96) magnetic field model [Tsyganenko and Stern, 1996] at 06:04 UT. Unless specified, the magnetic coordinates used hereafter are AACGM.

The locations of the ground stations used in this study are listed in Table 2.1. Geographic latitudes and longitudes, magnetic latitudes and longitudes, and MLT values are shown in the second to the last columns, respectively. Note that the bottom two rows show the locations of sample range gates for the camping beams of two SuperDARN mid-latitude radars; i.e.,

BKS (G38) indicates gate 38 in the camping beam of BKS radar.

Table 2.1: Coordinates of Ground Stations

Station Name	Station Code	GLAT ($^{\circ}$)	GLON ($^{\circ}$ E)	MLAT ($^{\circ}$)	MLON ($^{\circ}$)	MLT ^a (h)
Addis Ababa	AAE	9.03	38.76	0.78	110.72	8.79
Apia	API	-13.80	188.20	-15.61	-97.34	18.92
Ann Arbor	ANNA	42.42	276.10	53.21	-10.80	0.69
Athabasca	ATHA	54.71	246.69	61.99	-53.52	21.85
Bay Mills	BMLS	46.24	275.31	56.94	-11.83	0.62
Carson City	CCNV	39.19	240.22	45.08	-56.66	21.64
Kourou	KOU	5.21	307.27	9.51	23.58	2.98
Kototabang	KTB	-0.20	100.32	-9.08	172.15	12.89
Mbour	MBO	14.39	343.04	1.83	57.82	5.27
Ministik Lake	MSTK	53.35	247.03	60.70	-52.64	21.90
Newport	NEW	48.30	242.88	54.81	-56.15	21.67
Osakis	OSAK	45.87	264.92	56.06	-26.99	23.61
Ottawa	OTT	45.40	284.45	55.58	1.50	1.51
Pamatai	PPT	-17.56	210.42	-16.69	-74.56	20.44
Shumagin	SHU	55.40	199.50	53.10	-100.98	18.68
Thief River Falls	THRF	48.03	263.63	58.05	-29.02	23.48
Ukiah	UKIA	45.13	241.07	51.24	-57.33	21.59
Victoria	VIC	48.50	236.58	53.68	-63.37	21.19
Vulcan	VULC	50.37	247.02	57.72	-51.76	21.96
Wells Gray	WGRY	51.88	239.97	57.80	-60.68	21.37
Blackstone ^b	BKS (G38) ^c	48.65	265.64	59.12	-26.14	23.67
Fort Hays East ^b	FHE (G30) ^c	48.07	273.97	58.93	-13.81	0.49
Fort Hays West ^b	FHW (G30) ^c	50.61	251.58	59.11	-45.99	22.35

^aThe MLT values are calculated at 06:04 UT.

^bSuperDARN mid-latitude HF radar.

^cGate number in the camping beam of SuperDARN mid-latitude HF radar.

2.3 Observations and Analysis

In this section, the Pi2 event that occurred on 25 September 2014 between 06:00 and 06:15 UT is described in detail and analyzed using the data sets described in the previous section.

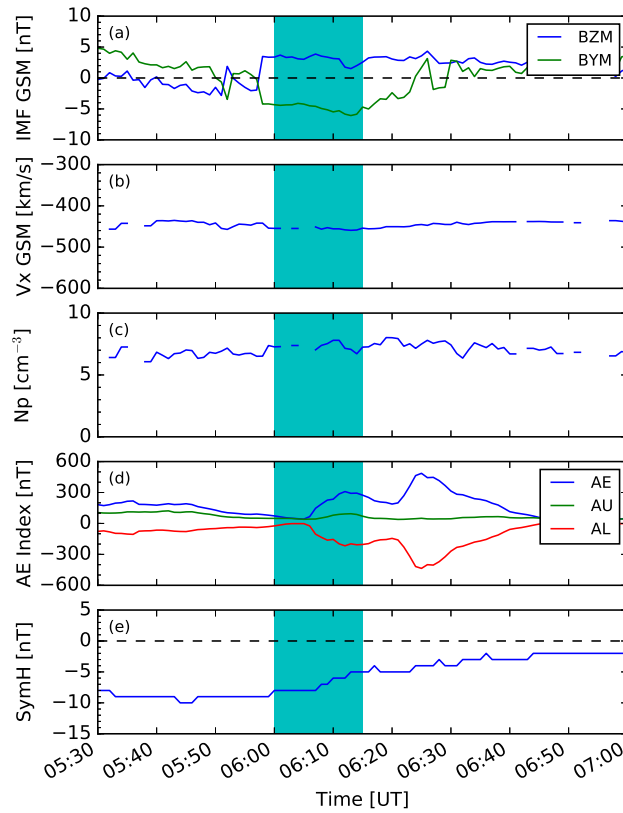


Figure 2.2: Interplanetary and geomagnetic conditions on 25 September 2014: (a) OMNI IMF By and Bz components and (b) solar wind speed V_x in the Geocentric Solar Magnetospheric (GSM) coordinate system, (c) solar wind proton density N_p , (d) AE (blue), AU (green), and AL (red) indices, and (e) SymH index. The cyan shaded region identifies the time interval of interest.

2.3.1 Interplanetary and Geomagnetic Conditions

Figure 2.2 provides an overview of the interplanetary and geomagnetic conditions from 05:30 to 07:00 UT. The cyan shaded region identifies the interval of interest. Of particular note is the intensification in the Auroral Electrojet (AE) index (Figure 2.2d) at $\sim 06:04$ UT which occurred a few minutes after the IMF (Figure 2.2a) turned northward at the bow shock as determined by OMNI analysis. This is consistent with a substorm onset which was indeed observed in auroral activity (not shown) by several THEMIS all-sky imagers whose locations are shown in Figure 2.1c as green dots. We can further conclude that this substorm was an

isolated non-storm event based on the weak SymH index (Figure 2.2e) during this period and through out the preceding day, as well as the absence of storm features in the solar wind particle data (Figure 2.2b and 2.2c).

2.3.2 THEMIS Spacecraft Observations

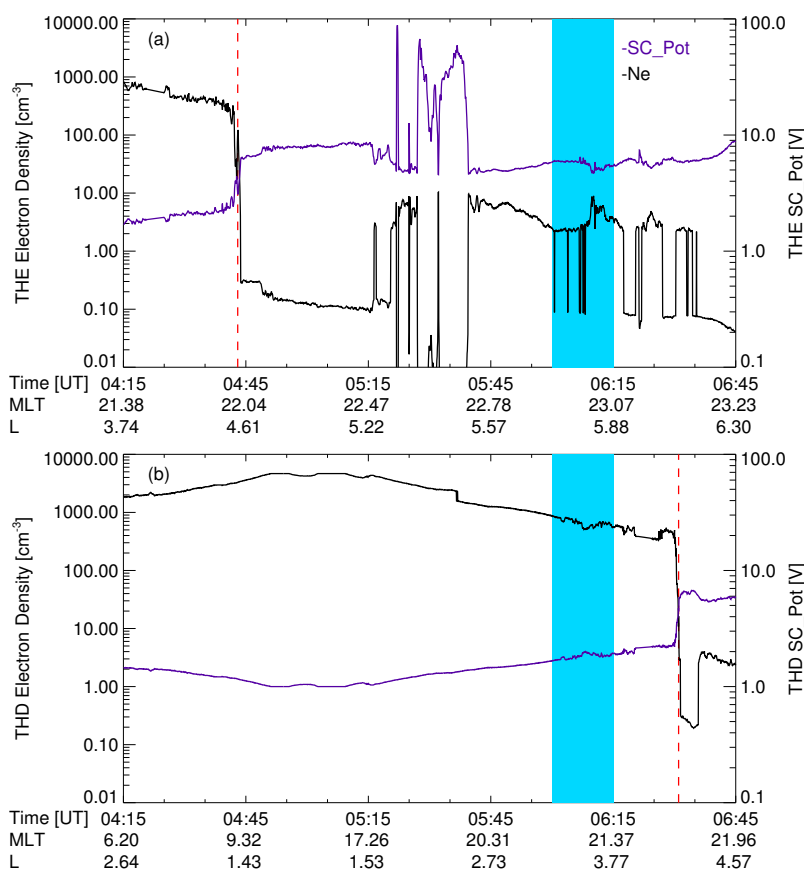


Figure 2.3: Plasmaspheric context of two THEMIS spacecraft during the time interval of Pi2 activity. Each panel shows profiles of spacecraft potential (blue) and electron density (black) for (a) THE and (b) THD. The cyan shaded region identifies the time interval of interest. Vertical dashed red lines identify sharp gradients indicative of plasmopause crossings.

Before we can analyze the THD and THE spacecraft measurements in detail, it is important to first identify whether or not they were inside the plasmasphere. Figure 2.3 shows THE (upper) and THD (lower) profiles of spacecraft potential (blue) and electron density (black)

from 04:15 to 06:45 UT. The electron density parameter was derived from the spacecraft potential. Vertical dashed red lines identify sharp gradients in the electron density and spacecraft potential suggesting THE made an outbound crossing of the plasmapause at \sim 04:43 UT ($L \sim 4.5$ and MLT ~ 22.0) while THD exited the plasmasphere somewhat later at \sim 06:31 UT ($L \sim 4.2$ and MLT ~ 21.7). Similar to Figure 2.2, cyan shaded regions identify the 06:00 to 06:15 UT time interval of interest allowing us to conclude that THD was inside the plasmasphere but THE was outside during this interval.

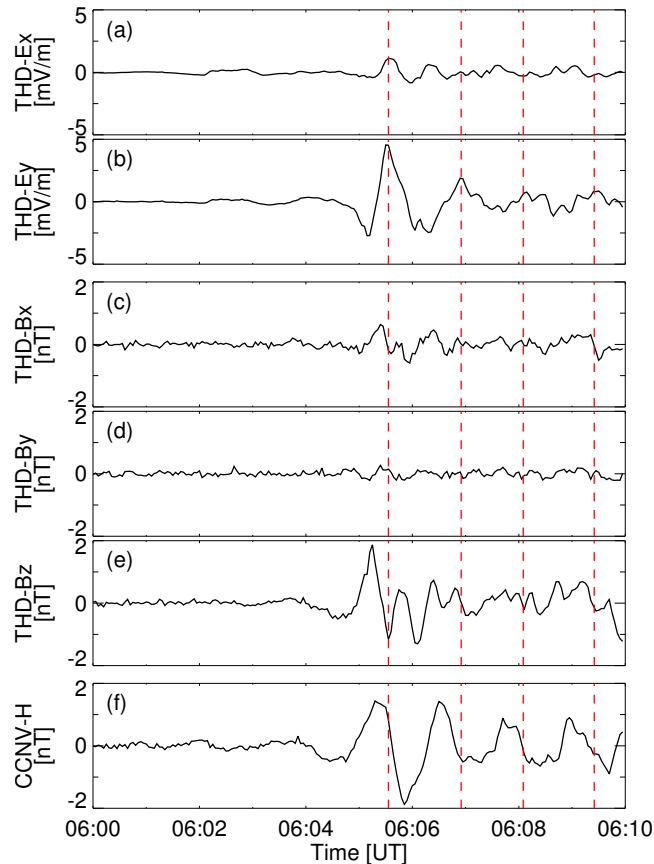


Figure 2.4: Time series of Pi2 pulsations observed inside the plasmasphere. The upper five panels show THD measurements of (a) Ex, (b) Ey, (c) Bx, (d) By, and (e) Bz components, while the bottom panel (f) shows the CCNV ground magnetometer H component. Vertical dashed red lines indicate prominent peaks in the THD Ey component.

Figure 2.4 shows time series of Pi2 pulsations observed inside the plasmasphere by THD and

a representative ground magnetometer. The upper five panels show the THD E_x , E_y , B_x , B_y , and B_z components, respectively. The bottom panel shows the H component from the CCNV ground magnetometer station located at $L \sim 2.0$ and MLT ~ 21.6 (see Figure 2.1c). The ground magnetometer data were resampled at 3 s step in order to have the same time resolution as the spacecraft measurements. Strong oscillations in the Pi2 band are clearly identifiable in the azimuthal component of the electric field (E_y) and the field-aligned component of the magnetic field (B_z) measured by THD, as well as the CCNV H component. The toroidal components (E_x , B_y) have much smaller amplitudes than the poloidal components (E_y , B_x , and B_z), which indicates a predominant fast-mode wave [Takahashi et al., 2003] observed at the location of THD inside the plasmasphere.

To further investigate the radial structure of the fast-mode wave seen by THD, we perform cross-spectral analysis to calculate the coherence and phase shift between the THD E_y and B_z components (Figure 2.5) and the THD E_y and CCNV H components. (Figure 2.6). The time interval for the cross-spectral analysis is 06:00 - 06:10 UT because the FGE data from THD is missing after 06:10 UT. The left three panels in Figure 2.5 show the THD E_y and B_z auto spectra and cross-spectrum, likewise in Figure 2.6. The right two panels show the coherence and phase shift as a function of frequency between the two components. It can be seen in Figure 2.5e that the THD E_y component oscillated nearly in quadrature ($\sim -100^\circ$ out of phase) with the THD B_z component at the cross-spectral dominant frequency ~ 13.4 mHz (Figure 2.5c), as indicated by the vertical dashed red lines. The coherence (Figure 2.5d) between the E_y and B_z pulsations at 13.4 mHz is ~ 0.65 . Similarly, Figure 2.6 shows strong coherence (~ 0.93) between the THD E_y and CCNV H components at the same peak frequency ~ 13.4 mHz with a cross phase value of $\sim -95^\circ$. These phase relationships and high coherence between the THD E_y , THD B_z , and CCNV H components are expected for a radially standing wave of the fundamental mode and thus are consistent with both the PCR

and PVR models [e.g., [Ghamry et al., 2015](#), [Luo et al., 2011](#)].

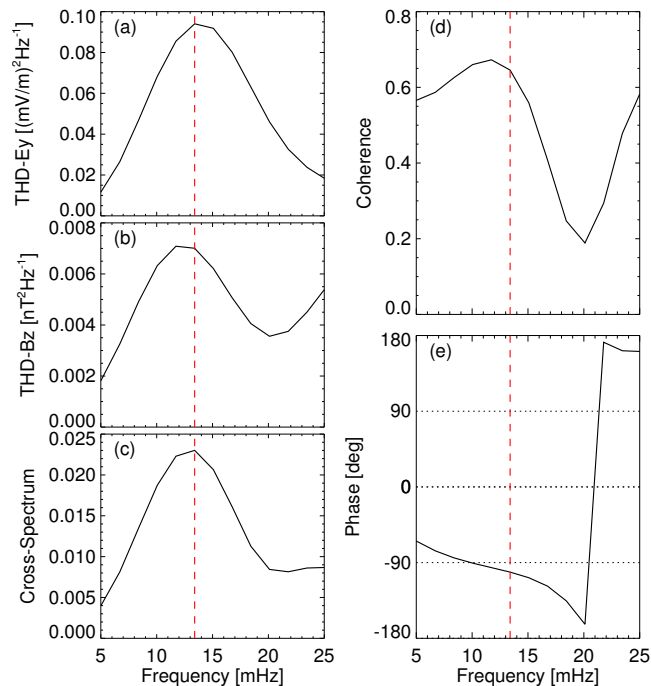


Figure 2.5: Cross-spectral analysis of THD Ey and Bz components: (a) Auto spectrum of the Ey component from THD, (b) Auto spectrum of the Bz component from THD, (c) Cross spectrum of the Ey and Bz components, (d) Coherence between the Ey and Bz components, and (e) Ey-Bz phase shift as a function of frequency. Vertical dashed red lines indicate the dominant cross-spectral frequency peak at ~ 13.4 mHz.

In order to fully distinguish between the PCR and PVR models, simultaneous observations outside the plasmasphere are needed. As indicated in [Figure 2.3](#), THE was located outside the plasmasphere during this period. It observed some wave activity signatures (not shown). However, the waveforms of the electric and magnetic field are more complicated. Several field components have multiple power spectral density peaks instead of one dominant frequency peak in the Pi2 band, and the pulsations generally show very small coherence with the ground magnetometer observations. Using these observations alone, we cannot differentiate between PCR and PVR. Next we proceed to examine the ground-based data sets for global characteristics of the pulsations and for evidence that favors one mechanism.

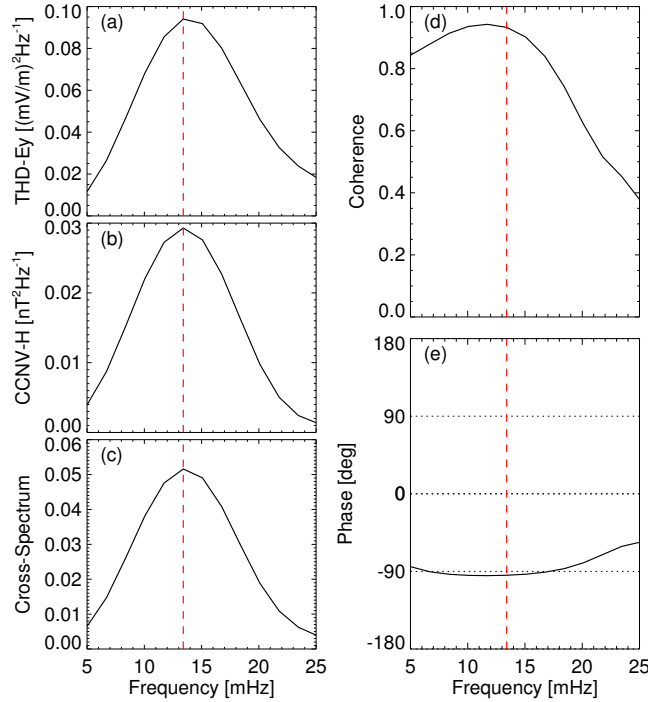


Figure 2.6: Cross-spectral analysis of THD Ey and CCNV H components (same format as Figure 2.5).

2.3.3 Ground Magnetometer Measurements

After examining the wave mode of the Pi2 pulsations in space, we search for Pi2 signatures on the ground. First, we examine the day-night structure of the pulsations at low latitudes. Magnetic field oscillations from a longitudinal chain of ground magnetometers (i.e., stations at about the same L shell but varying with magnetic longitude) are shown in Figure 2.7. The left axes identify the station names. The relevant L and MLT values are labeled at the upper right-hand corner in each panel. In all cases, Pi2 pulsations are clearly seen in the H (solid black) components with a similar waveform on the nightside and dayside at nearly the same time. While the amplitude of oscillations in the D (dashed blue) component is generally smaller than those in the H component. The vertical dashed red lines correspond to the peaks in the THD Ey pulsations identified in Figure 2.4. The similarity in waveforms and the fact that Pi2 pulsations were almost simultaneously observed on both dayside and

nightside at low latitudes lend further credence to the idea that the observed pulsations were associated with a plasmaspheric standing wave [Nosé et al., 2006, Sutcliffe and Yumoto, 1991].

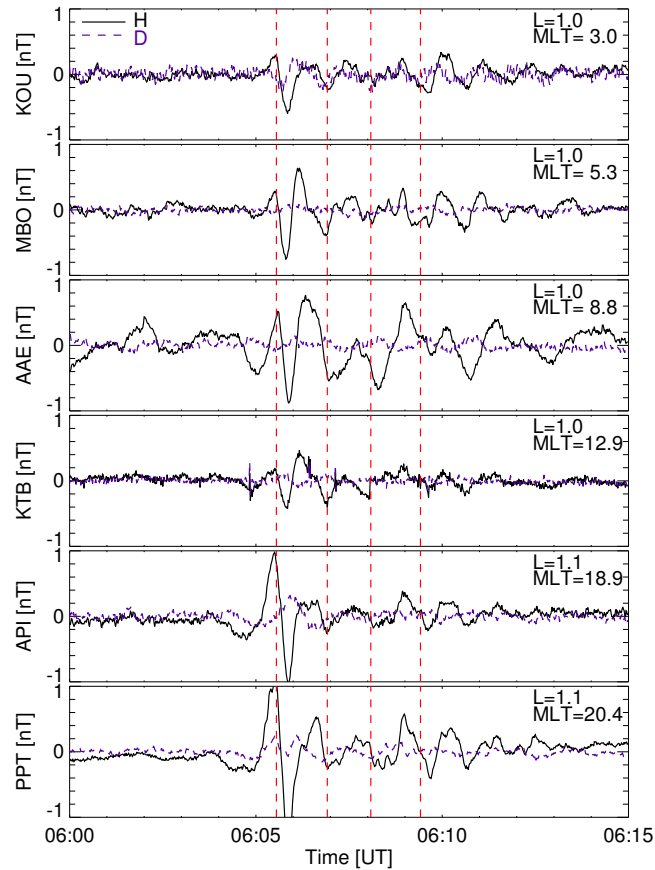


Figure 2.7: Magnetic local time variation of pulsations seen by several low latitude ground magnetometers. Filtered magnetic field H (solid black) and D (dashed blue) components are shown. Station identifiers are on the left axes and the relevant L and MLT values are labeled at the upper right-hand corner in each panel. Vertical dashed red lines identify the same times as those shown in Figure 2.4.

Next, we examine the radial structure of the pulsations using observations from a latitudinal chain of ground magnetometers (i.e., stations at about the same magnetic longitude but varying with magnetic latitude) straddling the footprint of the plasmapause. Recall from Figure 2.3 that THD made an outbound crossing of the plasmapause at $\sim 06:31$ UT corresponding to $L \sim 4.2$ and $MLT \sim 21.7$. Figure 2.8 shows a stack plot of six ground magnetometers

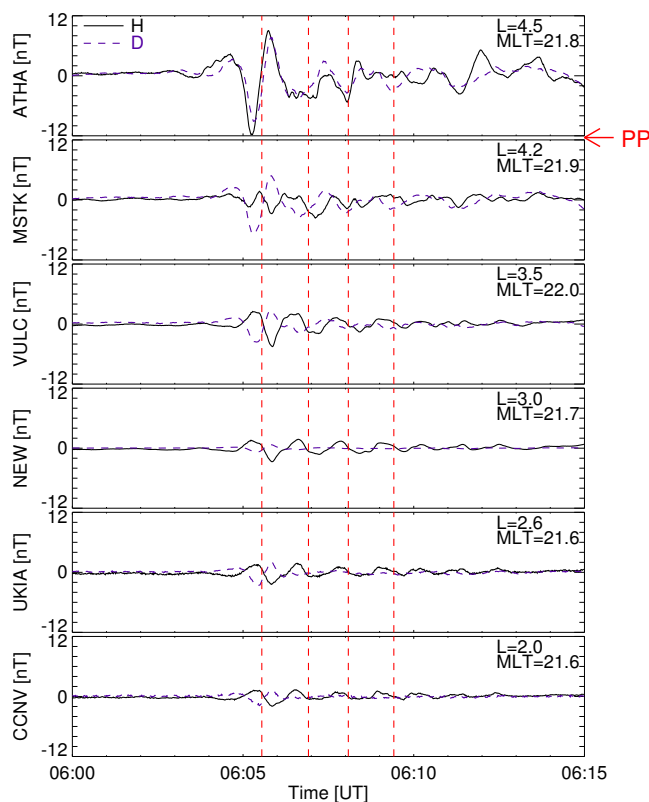


Figure 2.8: Latitudinal variation of pulsations seen by several nightside ground magnetometers straddling the footprint latitude of the plasmapause (similar format to Figure 2.7).

in this MLT sector spanning L values of 2.0 - 4.5. The THD measurements indicate the plasmapause was situated somewhere very close to the MSTK station ($L \sim 4.2$ and $MLT \sim 21.9$), as identified by the red arrow labeled “PP”. It can be seen that the station that observed the pulsations with the largest amplitude was located outside the plasmasphere and that the amplitude of the pulsations generally decreased with decreasing latitude. Also, the pulsations seen by the stations inside the plasmasphere were highly coherent in both H and D components, while those near the plasmapause (MSTK) and just outside of it (ATHA) had more complicated waveforms. Finally, it is also noteworthy that the D component pulsations were in phase at all latitudes whereas the H component experienced a phase reversal across the plasmapause between the MSTK and ATHA stations, which indicates a change in polarization.

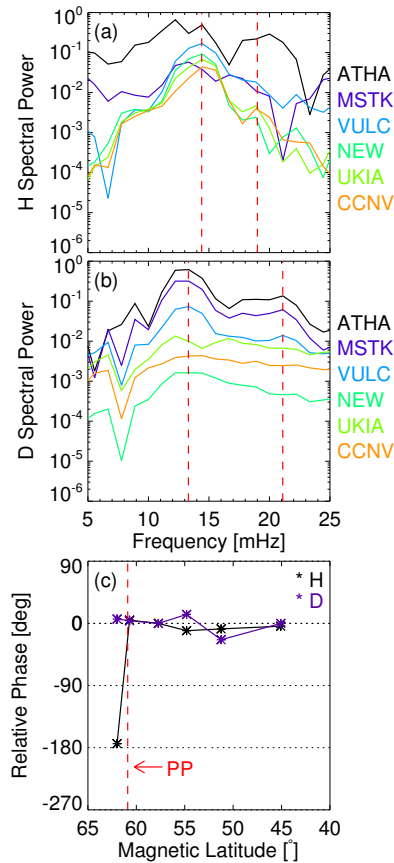


Figure 2.9: Spectral analysis of ground magnetometer data shown in Figure 2.8: auto spectral power density of (a) H and (b) D components, and (c) relative phase from cross-spectral analysis. In (a) and (b), the stations are color coded as shown at right; vertical dashed red lines identify the dominant spectral peaks. In (c), the H (D) component is shown in black (blue); vertical dashed red line identifies the magnetic latitude of the plasmopause footprint.

To further quantify how the frequency and phase of the Pi2 pulsations vary across the plasmopause, we apply Fast Fourier Transform (FFT) and cross-spectral analysis to the time series data shown in Figure 2.8. The time interval for both analyses is 06:00 - 06:15 UT. The results are shown in Figure 2.9. The VULC station was chosen as the reference to calculate the relative phase shift. The first two panels show the spectral power density of the H (Figure 2.9a) and D (Figure 2.9b) components color coded by station at right. Vertical dashed red lines identify the leading two peaks which occurred at ~ 14.4 mHz and ~ 19.0 mHz in the H component, but slightly shifted to ~ 13.3 mHz and ~ 21.1 mHz in the D component. There

is a general trend for the spectral power to increase with latitude with the secondary peaks, in particular, being much more prominent in the vicinity of the plasmopause. Figure 2.9c shows the relative phase variation across the stations as a function of magnetic latitude. The D components (blue asterisks) are highly coherent across all latitudes while the H component (black asterisks) reversed phase between ATHA and MSTK stations. As noted previously, the THD measurements placed the plasmopause very close to the MSTK station.

Thus far, the ground magnetometer observations are more consistent with the PVR model, considering that the Pi2 pulsations were observed outside the plasmopause as well as inside (Figure 2.8). Moreover, the ground magnetometer phase relationships are consistent with those found in previous observational studies of PVR [Takahashi et al., 2009]. However, for pulsations observed near and just outside the plasmopause, we cannot rule out the possibility of a field line resonance (FLR) which has been reported to show polarization change associated with the plasmopause in previous studies [e.g., Fukunishi, 1975]. To examine this possibility and characterize the pulsations at higher spatial resolution across the plasmopause, we next analyze the simultaneous SuperDARN HF radar observations.

2.3.4 SuperDARN HF Radar Measurements

The Pi2 pulsations were also detected on the camping beams of three mid-latitude SuperDARN radars operating in high time resolution THEMIS mode during the interval of interest. Figure 2.10 shows the spatial context of the radar measurements from 06:04 to 06:06 UT. LOS Doppler velocities are color coded according to the scale at right and the camping beams of the FHW, FHE, and BKS radars are overlaid in blue. Also shown, are the footprints of THD and THE indicated by black and blue asterisks respectively, and the magnetic latitude of the plasmopause footprint (dashed black curve) estimated from THD measurements at

06:31 UT. The overall sense of the Doppler velocities is positive (blue-green) on eastward pointing beams but negative (orange-red) on beams oriented to the west. This is consistent with a prevailing westward convection. Of particular note is the intensification of these flows in the narrow region immediately poleward of the THD estimated plasmopause. This is similar to the behavior expected for subauroral ion drifts (SAID) [Smiddy et al., 1977].

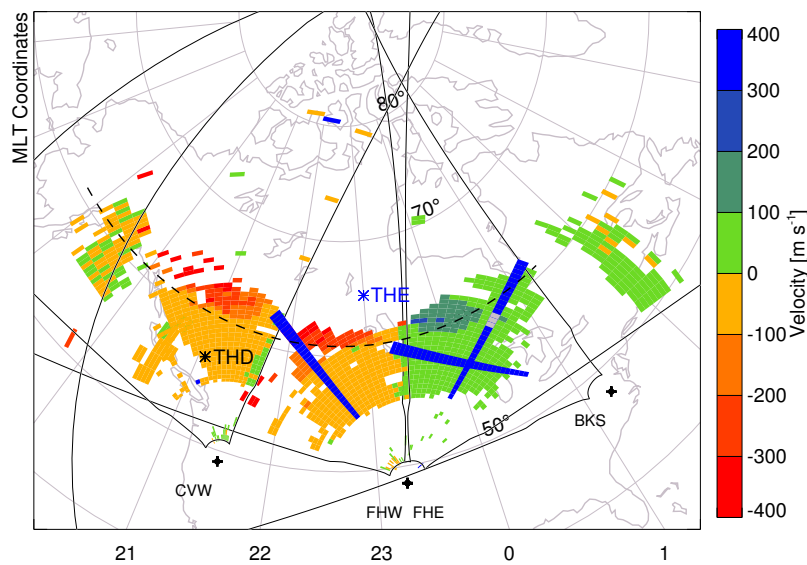


Figure 2.10: LOS Doppler velocities measured by three mid-latitude SuperDARN radars (CVW, FHW and FHE) at 06:04 - 06:06 UT, color coded according to the scale at right with positive (blue-green) values being toward the radar. Three camping beams (blue) of the FHW, FHE and BKS radars operating in THEMIS mode and footprints of THE (blue asterisk) and THD (black asterisk) at the same time are overlaid. The dashed black curve indicates the magnetic latitude of the plasmopause footprint.

Figure 2.11 shows the camping beam measurements as time series of color coded Doppler velocity and backscatter power versus magnetic latitude. Pi2 pulsations (alternating colored stripes between two vertical lines in the Doppler velocity time series at left panels were clearly observed in the camping beams of FHW (upper), FHE (middle), and BKS (lower) radars during the same interval as the THD and ground magnetometer Pi2 observations. The strongest ionospheric pulsations were observed by the FHW radar (peak to peak ~ 1 km/s) at $\sim 61.5^\circ$ MLAT corresponding to the SAID-like structure identified in Figure 2.10. The

FHE and BKS radars saw similar pulsations but at smaller amplitude (note different scales in the velocity color bars at right). Of the three, FHE observed the pulsations most clearly over a wider range of latitudes. Also noteworthy is the fact that FHW and BKS observed the pulsations against a background of mostly westward flows, while FHE saw flows which were eastward at higher latitudes and westward at lower latitudes. This region of sheared flows observed by FHE at $\sim 59.5^\circ$ MLAT is most likely the so-called Harang discontinuity [Koskinen and Pulkkinen, 1995, Zou et al., 2009].

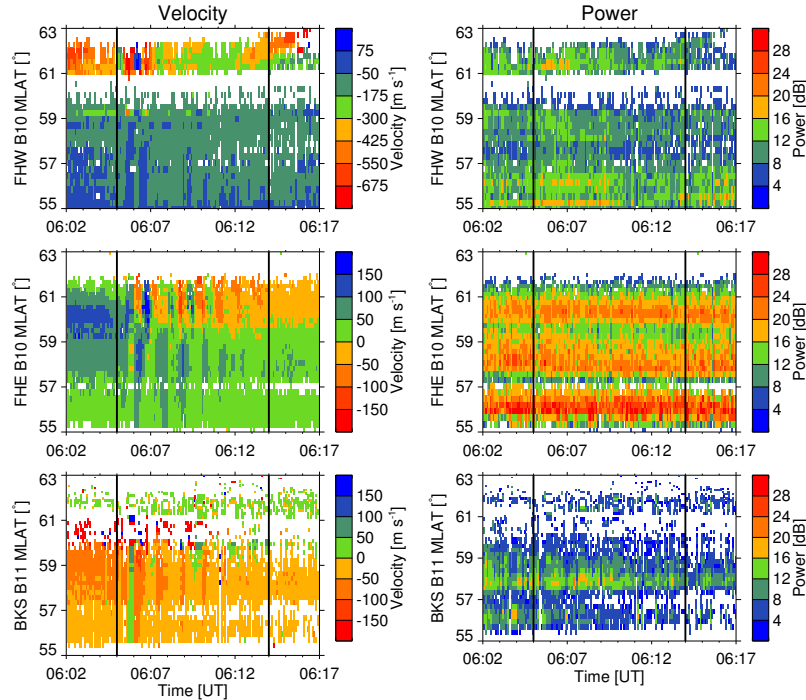


Figure 2.11: Left (Right) panels show time series of Doppler velocity (backscatter power) versus magnetic latitude measured on the camping beams of the FHW, FHE, and BKS SuperDARN radars. Two vertical black lines identify the interval of interest when Pi2 pulsations were observed during the early stages of the substorm.

Figure 2.12 shows a more detailed view of the FHE camping beam data shown in Figure 2.11. These data have been resampled to 6 s resolution and then high-pass filtered with 150 s period. Figure 2.12a shows a time series stack plot of the data measured at gates 23 - 42. The following features are particularly noteworthy: (i) a pronounced minimum in

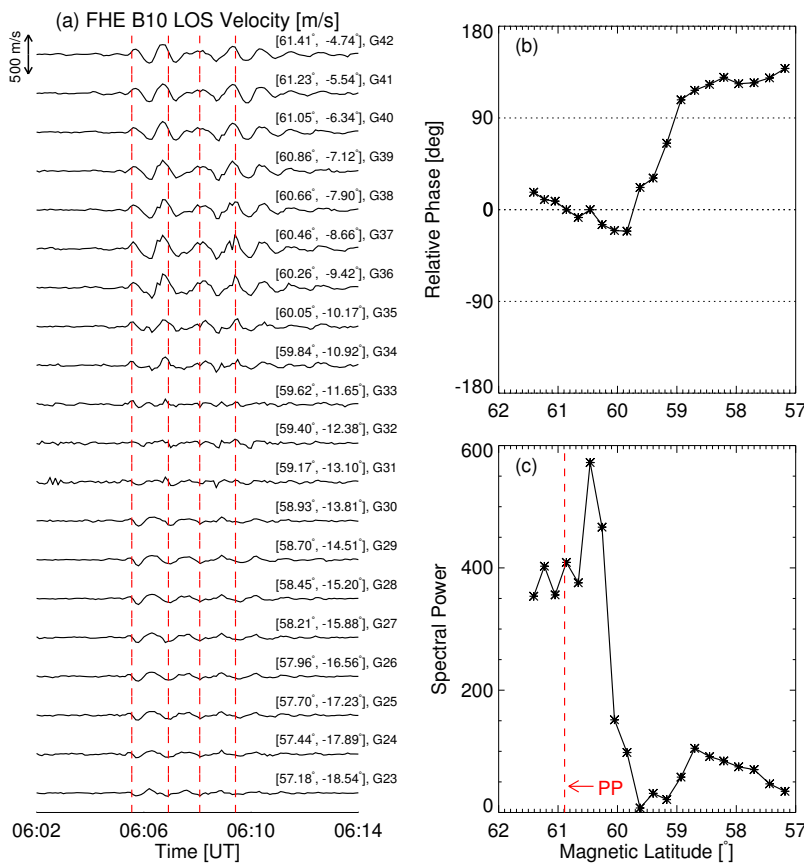


Figure 2.12: Latitudinal variation of pulsations observed on the camping beam of the FHE radar: (a) Time series stack plot for range gates 23 - 42; (b) Relative phase versus magnetic latitude; and (c) Spectral power versus magnetic latitude.

amplitude of the pulsations exists between gates 31 - 33 (59.17° - 59.62° MLAT) separating stronger pulsations at higher latitudes with weaker pulsations at lower latitudes, and, (ii) phase shifts exist between the pulsations at higher latitude and those at lower latitudes. These features are explored further in Figure 2.12b and 2.12c which show the variation in relative phase and spectral power, respectively, as a function of magnetic latitude. The range gate 37 with the largest spectral power (Figure 2.12c) was used as the reference to calculate the relative phase (Figure 2.12b). Figure 2.12c confirms that there is a softening in spectral power centered at $\sim 59.40^\circ$ MLAT with an upward trend equatorward of this location and a pronounced peak poleward of it at $\sim 60.5^\circ$ MLAT. Note that the softening,

denoted by gray cells in Figure 2.10 inside the FHE camping beam, was co-located with the Harang discontinuity ($\sim 59.5^\circ$) and the location of the pronounced spectral power peak was situated $\sim 0.5^\circ$ MLAT equatorward of the magnetic latitude of the plasmopause estimated from the THD spacecraft measurements at 06:31 UT. At first glance this phase variation and latitudinal behavior of the spectral power of the pulsations seem to point to the possibility of a FLR. However, Figure 2.12b shows that the rapid phase shift occurred at the spectral power minimum which was equatorward of the spectral power peak. Thus the pulsations are not consistent with a FLR which would require the amplitude enhancement to be centered on the rapid phase variation across the resonant shell that is usually no more than 1° or 2° in extent [Ruohoniemi et al., 1991]. In contrast, this kind of phase shift across the amplitude minimum may be consistent with the radial standing wave structure expected for PVR as reported by previous investigations [Lee and Takahashi, 2013].

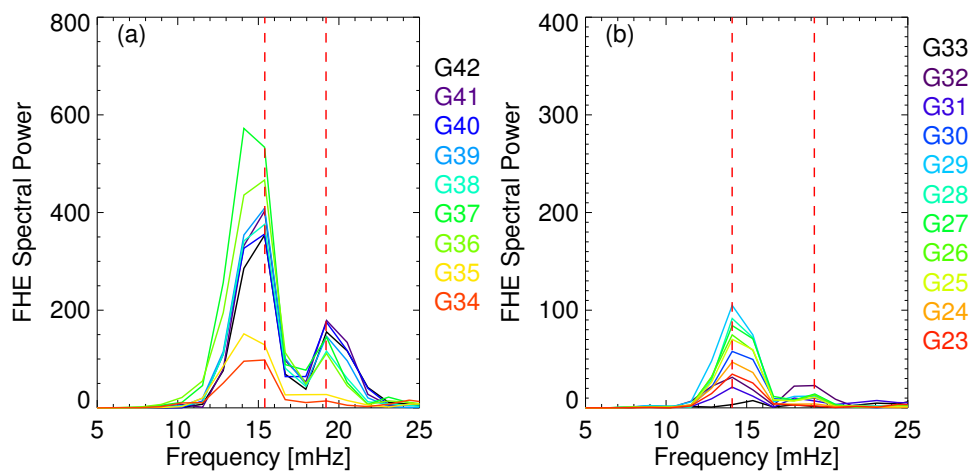


Figure 2.13: Spectral analysis of FHE radar camping beam measurements for (a) range gates 34 - 42 nominally near or poleward of the plasmopause, and (b) range gates 23 - 33 well inside the plasmasphere. Vertical dashed red lines identify the dominant spectral peaks.

Putting aside ambiguities in the precise location of the plasmopause, we analyze the range gates of the FHE camping beam in two categories: those situated near or poleward of the plasmopause versus those well inside the plasmasphere. Spectra for these two categories of

Pi2 pulsations are shown in Figure 2.13. The time interval for the spectral analysis is 06:02 - 06:15 UT because SuperDARN FHE radar missed the first two minutes of the interval. For range gates 34 - 42 (Figure 2.13a) nominally near or poleward of the plasmapause footprint, the Pi2 pulsations have much larger power than the range gates 23 - 33 (Figure 2.13b) that were well inside the plasmasphere (note the different scales). Two spectral peaks indicated by vertical dashed red lines were present both inside (~ 14.1 MHz and ~ 19.2 MHz) and outside (~ 15.4 MHz and ~ 19.2 MHz) the plasmasphere. These frequencies are similar to those observed by the ground magnetometers in Figure 2.9.

2.3.5 Polarization and Propagation Analysis

The evidence presented thus far is very suggestive of a global standing wave mode. However, except for the compressional wave components (E_y and B_z), the other electric field and magnetic field components (E_x , B_x , and B_y) from THD oscillated with much smaller amplitudes, as can be seen in Figure 2.4. Therefore, a mixture of other wave modes, such as propagating fast waves and/or shear Alfvén waves, together with a predominant standing fast wave, is a plausible scenario [Lysak et al., 2015, Teramoto et al., 2014].

Many previous investigations have used polarization analysis of ground magnetometer measurements to help identify the location of the Pi2 source at high latitudes [Gelpi et al., 1987, Takahashi and Liou, 2004]. Figure 2.14 shows filtered ground magnetometer data from two longitudinal magnetometer chains ($L \sim 3.5$ and $L \sim 2.9$) and associated hodograms. It can be seen that pulsations in the ~ 21 -22 MLT sector (WGRY and VULC in Figure 2.14c and VIC and NEW in Figure 2.14f) are linearly polarized with their major axes pointing northwest whereas those further eastward (THRF, BMLS, OTT, OSAK, and ANNA) have dominant D components and are left-handed polarized (counterclockwise arrows in the hodograms).

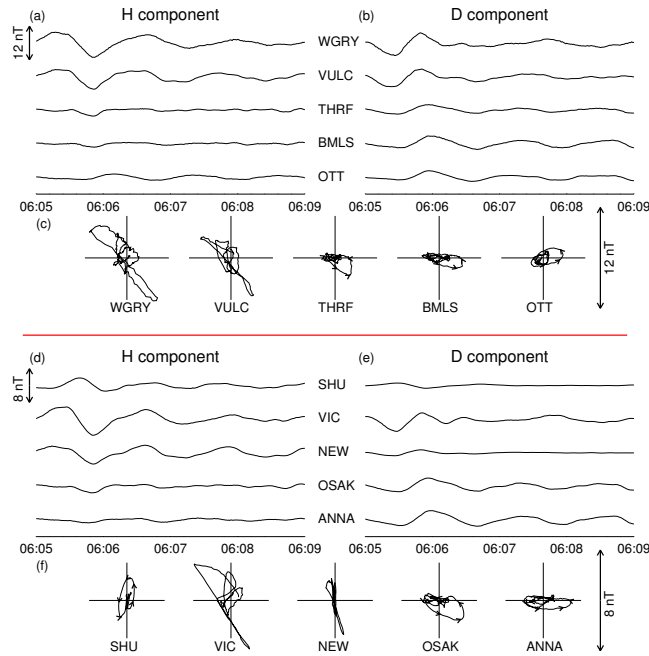


Figure 2.14: Filtered ground magnetic field data between 06:05-06:09 UT from two longitudinal magnetometer chains at $L \sim 3.5$ (upper panels a, b, c) and $L \sim 2.9$ (lower panels d, e, f). Panels (a) and (d) show the H component while panels (b) and (e) show the D component. Panels (c) and (f) are corresponding hodograms with arrows showing the sense of polarization.

The SHU station located at the duskside also has a counterclockwise sense of polarization with its major axis slightly pointing northeast. This longitudinal polarization pattern is indicative of a substorm current wedge configuration [e.g., Lester et al., 1984]. Accordingly, we suggest that the center of the substorm current wedge was located east of the SHU station (MLT=18.68) and west of the VIC station (MLT = 21.19). Furthermore, the longitudinal variation of magnetic bays (not shown) are also consistent with a substorm current wedge configuration. Specifically, negative (positive) bays in the D components of mid-latitude stations east (west) of the VIC station support the idea that all the mid-latitude stations shown in Figure 2.14 (except for SHU) were located inside a downward field-aligned current (FAC) region spanning at least 4 MLT hours.

To investigate the azimuthal propagating property of the Pi2 pulsations, we apply both

cross-spectral and cross correlation analyses to data from selected radar gates and ground magnetometers to calculate the wave number, coherence, and time lag. The locations can be found in Table 2.1. For the ground magnetometer data, we use both H and D components for the calculation. For the radar data, we interpolated the data into 1 s resolution for both analyses. When analyzing data from the BKS and FHE radars, we change the sign of FHE data to take account of the different pointing directions (westward (eastward) for BKS (FHE)). The interval of radar (ground magnetometer) data for both analyses is 06:02-06:15 (06:00-06:15) UT. Location pairs were chosen to have small difference in magnetic latitude and longitude. The results are shown in Table 2.2. The third column shows the L value, the fourth column is the phase shift ($\Delta\varphi$) from cross-spectral analysis, and the fifth column shows the magnetic longitude separation ($\Delta\theta$) between the two sites. The m value from the cross-spectral analysis (m_{cs}) in the sixth column is calculated as the phase shift divided by the magnetic longitude difference. The seventh and eighth columns show the cross-spectral peak frequency and coherence, respectively. The last three columns show the cross correlation coefficient, time lag in seconds, and m value (m_{cc}) which is calculated as $(T_{cc} \times 2 \times 360 \times f_{cs})/\Delta\theta$. Note that the upper three location pairs are from the pre-midnight sector, while the lower three pairs are east of 23 MLT (see Table 2.1 for location details). Location 1 is always westward of Location 2. Thus, a negative value in the phase shift ($\Delta\varphi$), m value, and time lag (T_{cc}) indicates that the pulsations in Location 1 lag those in Location 2, which suggests westward propagation.

From Table 2.2 we can see that the pre-midnight location pairs show westward propagation of pulsations from both methods, though the cross correlation analysis generally produces larger m number values. The coherence of the magnetic field H components for two pairs of pre-midnight ground magnetometers calculated from both methods are high, while the coherence of D components from the cross-spectral analysis are relatively low (0.57 and 0.41). Of

Table 2.2: Cross-spectral and cross correlation analyses of midlatitude Pi2 pulsations (See text for details)

Location 1	Location 2	L	$\Delta\varphi$ ($^\circ$)	$\Delta\theta$ ($^\circ$)	m_{cs}	f_{cs} (mHz)	Coh	C_{occ}	T_{cc} (s)	m_{cc}
FHW (G30)	BKS (G38)	~ 3.8	-101.45	19.85	-5.11	14.12	0.60	0.68	-18	-9.22
WGRY (H)	VULC (H)	~ 3.5	-28.56	8.92	-3.20	13.35	0.81	0.86	-4	-4.31
WGRY (D)	VULC (D)	~ 3.5	-14.68	8.92	-1.64	12.24	0.57	0.86	-2	-1.97
VIC (H)	NEW (H)	~ 2.9	-12.07	7.22	-1.67	13.35	0.84	0.90	-2	-2.66
VIC (D)	NEW (D)	~ 2.9	-47.25	7.22	-6.54	12.24	0.41	0.82	-3	-3.66
BKS (G38)	-FHE (G30)	~ 3.8	5.64	12.33	0.46	14.12	0.92	0.88	1	0.82
THRF (H)	BMLS (H)	~ 3.5	-18.18	17.19	-1.06	12.24	0.61	0.80	0	0
THRF (D)	BMLS (D)	~ 3.5	10.02	17.19	0.58	13.35	0.81	0.88	2	1.12
OSAK (H)	ANNA (H)	~ 3.0	-39.12	16.19	-2.42	13.35	0.76	0.80	-4	-2.37
OSAK (D)	ANNA (D)	~ 3.0	8.07	16.19	0.50	13.35	0.94	0.95	2	1.19

particular note is the mixing of azimuthal propagations (predominantly eastward) and very small m number calculated from the eastern stations. Contrary to the pre-midnight ground magnetometer stations, the coherence of H components from the cross-spectral analysis are lower than their D component counterparts. The very small value of the m number and mixed azimuthal propagation directions at the 23-01 MLT sector suggest that the Pi2 energy source was located on the same meridian. According to [Takahashi and Liou \[2004\]](#), a cavity mode excited by longitudinally localized disturbances can produce a longitudinal polarization pattern consistent with the substorm current wedge model with the center of the Pi2 energy source located to the east of the auroral surge and probably close to the center of the substorm current wedge. The longitudinal polarization pattern of the mid-latitude Pi2 pulsations in our study implies that the center of the substorm current wedge was located to the west of the 21 MLT sector, which is roughly 2-3 MLT hours west of the Pi2 energy source region near midnight.

2.4 Discussion

In the previous section, we analyzed the Pi2 pulsations both in space and on the ground. The THD spacecraft inside the plasmasphere observed Pi2 pulsations that were consistent with a predominant standing fast-mode wave. The similarity of Pi2 observations from dayside and nightside ground magnetometers at low latitudes indicates a global wave mode. The harmonic frequency peaks of these pulsations further confirm the plasmaspheric standing wave property. Similar wave signatures were observed by three SuperDARN mid-latitude radars and also showed harmonic properties. Pi2 pulsations were observed by both the SuperDARN radars and ground magnetometers poleward of the footprint of the plasmopause. Finally, polarization and propagation analysis of mid-latitude Pi2 pulsations suggest the energy source of these pulsations was located roughly 2-3 MLT hours east of the center of the substorm current wedge, with westward propagation in the pulsations west of the source region and mixing azimuthal propagations near (or just east of) the source region.

After analyzing the observations from space to the ground, we now speculate on the possible generation mechanism for the observed Pi2 pulsations. The PVR and PCR models are two likely source mechanisms of the observed mid-latitude and low latitude Pi2 pulsations in this study. The essential difference between these two models is that pulsations can be observed outside of the plasmasphere in the PVR model, while in the PCR model, pulsations are confined to the plasmasphere. In this particular case, ground magnetometers and radar gates poleward of the plasmopause footprint also observed Pi2 pulsations, which indicates that the pulsations were not strictly localized to the plasmasphere. We thus argue that the evidence supports the PVR model over the PCR model, although there is some ambiguity as to the precise location of the plasmopause in these observations.

In the fundamental mode of the PVR, the Bz node (or Bz amplitude minimum) can be located

just equatorward of the plasmopause [see Figure 12 in [Takahashi et al., 2003](#)]. Crossing this Bz node, a 180° phase shift in the Bz component can be observed. During this event, the pulsations in the Bz component from THD at $L \sim 3.4$ show little phase shift with those in the H component from CCNV ($L \sim 2.0$) at the fundamental frequency. The pulsations observed by ground magnetometers at and below the VULC station ($L \sim 3.5$) are highly coherent without significant phase shift (Figure 2.9c). Therefore, it is very likely that the Bz node was located somewhere between $L \sim 3.5$ and the plasmopause ($L \sim 4.2$), which is consistent with the scenario in Figure 12 from [Takahashi et al. \[2003\]](#).

In the PVR model, one would expect to see Pi2 pulsations outside of the plasmasphere in space as well. However, as noted in section 3.2, the THE spacecraft was located outside the plasmasphere at $L \sim 6.0$ but observed some wave activity signatures which were more complicated than the THD pulsations (not shown). Specifically, several field components had multiple power spectral density peaks instead of one dominant frequency peak in the Pi2 band, and the pulsations generally showed very small coherence with the ground magnetometer observations. THE did see some pulsations in the Pi2 frequency range, but they were probably not the PVR mode, or perhaps, some small amplitude of PVR mixed with other wave modes. It is our contention that THE did not observe clear signatures of the PVR mode outside the plasmopause because it was far enough away from the plasmopause location ($L \sim 4.2$ at \sim MLT 21.7) for the amplitude of the PVR oscillations to have decayed away. On the other hand, unlike the radar and ground magnetometer observations, there is no second harmonic frequency peak in the Pi2 frequency range in the space observations (E_y/B_z components at THD in Figure 2.5). The second harmonic frequency from the ground observations is more evident near the plasmopause. This inconsistency between the space and ground observations of harmonic structure in the Pi2 pulsations is a topic for further study. Additionally, the role of some other mid-latitude structures which were located near

to the plasmopause, such as the Harang discontinuity and SAID-like velocity feature, in modulating the pulsations in amplitude and phase is a direction for future study.

Moreover, one can argue that the Pi2 pulsations could be caused by other mechanisms other than eigenmodes of the plasmasphere. [Teramoto et al. \[2016\]](#), also using THEMIS satellites, mid-latitude SuperDARN radars, and ground-based magnetometers, investigated the spatial characteristics and generation mechanisms of a Pi2 event in the vicinity of the plasmopause. In their study, earthward and duskward propagating waves were observed inside the plasmasphere by THEMIS spacecraft which led them to suggest that a plasmaspheric cavity resonance with harmonic structures was localized at midnight and leaking energy earthward and duskward via propagating compressional waves. They also suggested the pulsations observed outside and inside the plasmopause were from different sources because the frequencies of the Pi2 pulsations from these two regions were different based on the SuperDARN radar observations. By contrast, for our event, we suggest Pi2 pulsations observed just outside and inside the plasmopause are from the same source (PVR mode). Recall that dayside magnetometers observed Pi2 pulsations simultaneously with nightside magnetometers at low latitudes ([Figure 2.7](#)) and that Pi2 pulsations with fundamental and second harmonic frequencies were observed by both ground magnetometers and SuperDARN radars. It is difficult to see how another mechanism, such as propagating fast waves or FLRs, could generate globally coherent waves at harmonic frequencies without significant time delays.

Finally, Pi2 pulsations observed at subauroral latitudes have been reported to be associated with high-latitude phenomena, such as the substorm current wedge and westward traveling waves [[Takahashi and Liou, 2004](#), [Yeoman et al., 1990](#)]. The longitudinal polarization pattern and azimuthal propagation of mid-latitude Pi2 pulsations in our study imply a connection with high latitude phenomena as well. Many previous papers found that the major axis of Pi2 pulsations at mid- and sometimes even low-latitudes points towards the center of

the substorm current wedge and the source region of the Pi2 pulsations [Gelpi et al., 1987, Takahashi and Liou, 2004]. Our results indicate that the source of the Pi2 pulsations in this event was located at the downward FAC region which is roughly 2-3 MLT hours east of the center of the substorm current wedge. Westward propagation was observed in the pulsations west of the source region while small eastward phase propagation was observed by mid-latitude ground magnetometers (D component) just east of the source region (Table 2.2). These features are consistent with a PVR mode being excited by a longitudinally localized source. Some other studies [Li et al., 1998, Yeoman et al., 1990] have found a predominant westward phase propagation of Pi2 pulsations at most longitudes. It has also been suggested that the westward phase propagation and longitudinal polarization pattern of mid-latitude Pi2 pulsations could be explained by superposition of a westward traveling wave at higher latitudes and an eastward propagating wave of smaller amplitude at lower latitudes [Southwood and Hughes, 1985]. Recently, Keiling [2012] found that high-latitude Pi2 pulsations can be driven by the ballooning instability in the near-Earth plasma sheet before auroral breakup. The observational evidence for the ballooning mode was identified using conjugate spacecraft and ground data, however, the manner of mode coupling to the ionosphere/ground and propagation towards lower latitudes is still far from being understood. It is therefore possible that the mid- and low-latitude Pi2 pulsations seen in our study were likewise modulated by (or mixed with) pulsations from high latitudes generated by other sources such as the ballooning instability. Confirmation of this specific scenario would require additional spacecraft measurements.

Therefore, different observational evidence and generation mechanisms indicate that the mid-latitude region is indeed a complicated transition region which requires further statistical investigations of Pi2 pulsations observed near the plasmopause over a wider range in the magnetosphere and on the ground. Effects from the substorm current wedge, possi-

ble westward (or eastward) traveling wave at high latitudes and the radially standing wave from low latitudes need to be taken into account when studying mid-latitude Pi2 pulsations. Many previous papers have suggested that the PVR/PCR mode waves are radially standing waves bouncing between the ionosphere and the plasmopause, but they can propagate in the azimuthal direction with a small value of the azimuthal wave number [Li et al., 1998, Liou et al., 2000, Nosé et al., 2006]. In our study, we suggest the observed Pi2 pulsations are a predominant PVR mode, a radial standing wave being excited globally by a longitudinally localized source with westward phase propagation west of the source region and mixed propagation directions (but predominantly eastward) east of the source region.

2.5 Conclusions

In this study, we provide evidence of the PVR model as the source mechanism for the Pi2 pulsations observed simultaneously by space and ground-based instruments during a substorm on 25 September 2014. We have examined the amplitude, frequency, polarization, and phase variations of these Pi2 pulsations across various data sets. The observations and conclusions are summarized as follows: (1) High coherence and phase relationship of Pi2 pulsations observed in the THD Ey, THD Bz and CCNV H components indicate the presence of a predominant standing fast-mode wave inside the plasmasphere. (2) Simultaneous Pi2 observations from dayside and nightside ground magnetometers at low latitudes indicate the global nature of this event. (3) The fundamental and second harmonic frequency peaks from the FFT analysis of these pulsations confirm the standing wave property. (4) A change in the polarization of the pulsations observed by nightside ground magnetometers straddling the ionospheric footprint of the plasmopause is consistent with previous observations of PVR. (5) Similar wave signatures observed by three SuperDARN mid-latitude radars inside as well

as beyond the footprint of the plasmopause with harmonic properties further favor the PVR model over the PCR model as the source mechanism. (6) Longitudinal polarization pattern of mid-latitude Pi2 pulsations is consistent with previous observations. (7) Westward phase propagation of mid-latitude Pi2 pulsations was observed in the pre-midnight while mixing azimuthal propagations were observed near the source region. Therefore, we conclude that the space and ground-based observations presented in this study can be explained by a predominant PVR mode excited by a longitudinally localized source near midnight.

Acknowledgments

The Virginia Tech authors acknowledge the support of the NSF under grants AGS-1341918 and AGS-1342968. N. A. Frissell is supported by NSF grant PLR-1443507. J. Liu is supported by NASA grant NNX14AC17G, NASA contract NAS5-02099, and NSF grant 1401822. The authors acknowledge the use of SuperDARN data, which are freely available through the SuperDARN website at Virginia Polytechnic Institute and State University (<http://vt.superdarn.org/>). SuperDARN is a collection of radars funded by national scientific funding agencies of Australia, Canada, China, France, Japan, South Africa, United Kingdom, and United States of America. We acknowledge NASA contract NAS5-02099 and V. Angelopoulos for use of data from the THEMIS Mission (<http://themis.ssl.berkeley.edu/>). Specifically J. W. Bonnell and F. S. Mozer for use of EFI data; K. H. Glassmeier, U. Auster and W. Baumjohann for the use of FGM data; S. Mende and C. T. Russell for use of the GMAG data and NSF for support through grant AGS-1004814; I.R. Mann, D.K. Milling and the rest of the CARISMA team for use of GMAG data (<http://carisma.ca/>). The authors also thank the ISEE, Nagoya University for providing the ground magnetometer data. The results presented in this paper rely on data collected at magnetic observatories. We

thank the national institutes that support them and INTERMAGNET for promoting high standards of magnetic observatory practice (www.intermagnet.org).

Chapter 3

Survey of Ionospheric Pc3-5 ULF Wave Signatures in SuperDARN High Time Resolution Data

X. Shi¹, J. M. Ruohoniemi¹, J. B. H. Baker¹, D. Lin¹, E. C. Bland^{2, 3}, M. D. Hartinger¹, and
W. A. Scales¹

¹Department of Electrical and Computer Engineering, Virginia Tech, Blacksburg, VA, USA.

²Department of Arctic Geophysics, University Centre in Svalbard, Longyearbyen, Norway.

³Birkeland Centre for Space Science, Bergen, Norway.

Shi, X., Ruohoniemi, J. M., Baker, J. B. H., Lin, D., Bland, E. C., Hartinger, M. D., & Scales, W. A. (2018). Survey of ionospheric Pc3-5 ULF wave signatures in SuperDARN high time resolution data. *Journal of Geophysical Research: Space Physics*, 123, 4215–4231. <https://doi.org/10.1029/2017JA025033>

Abstract

Ionospheric signatures of ultralow frequency (ULF) wave in the Pc3-5 band (1.7-40.0 mHz) were surveyed using ~ 6 s resolution data from Super Dual Auroral Radar Network (SuperDARN) radars in the Northern Hemisphere from 2010 to 2016. Numerical experiments were conducted to derive wave period dependent thresholds for automated detection of ULF waves using the Lomb-Scargle periodogram technique. The spatial occurrence distribution, frequency characteristics, seasonal effects, solar wind condition and geomagnetic activity level dependence have been studied. Pc5 wave events were found to dominate at high and polar latitudes with a most probable frequency of 2.08 ± 0.07 mHz while Pc3-4 waves were relatively more common at midlatitudes on the nightside with a most probable frequency of 11.39 ± 0.14 mHz. At high latitudes, the occurrence rate of Pc4-5 waves maximizes in the dusk sector and during winter. These events tend to occur during low geomagnetic activity and northward interplanetary magnetic field (IMF). For the category of radially bounded but longitudinally extended Pc4 events in the duskside ionosphere, an internal driving source is suggested. At midlatitudes, the Pc3-4 occurrence rate maximizes premidnight and during equinox. This tendency becomes more prominent with increasing auroral electrojet (AE) index and during southward IMF, which suggests many of these events are Pi2 and Pc3-4 pulsations associated with magnetotail dynamics during active geomagnetic intervals. The overall occurrence rate of Pc3-5 wave events is lowest in summer, which suggests that the ionospheric conductivity plays a role in controlling ULF wave occurrence.

3.1 Introduction

Ultralow frequency (ULF) waves are magnetohydrodynamic (MHD) plasma waves in the frequency band of roughly 1 mHz to several hertz. They are ubiquitous and have been observed in geospace and on the ground for over 50 years [e.g., [Dungey, 1955](#), [Saito, 1969](#)]. ULF waves were originally called micropulsations or magnetic pulsations since they were first observed by ground magnetometers. ULF pulsations are classified into two types: pulsations continuous (Pc) and pulsations irregular (Pi) with several subclasses (Pc1-5 and Pi1-2) according to their frequencies and durations [[Jacobs et al., 1964](#)]. With respect to polarization, ULF waves can be categorized into three modes: poloidal ($\Delta B_r, \Delta E_\varphi$), compressional ($\Delta B_{//}, \Delta E_\varphi$), and toroidal ($\Delta B_\varphi, \Delta E_r$). Here, B_r (E_r), $B_{//}$, and B_φ (E_φ) are the radial, parallel (or compressional), and azimuthal components in the local magnetic field system, respectively. ULF waves are believed to play important roles in magnetospheric plasma energization and loss and energy transfer from the solar wind to the Earth's magnetosphere and ionosphere [[Elkington et al., 1999](#), [Mathie and Mann, 2000](#), [Zong et al., 2009](#)].

Numerous studies have used ground magnetometer and spacecraft measurements to study ULF pulsation occurrence statistics and source mechanisms [e.g., [Anderson, 1994](#)]. Several theories have been proposed for the excitation mechanisms of ULF waves observed in the Earth's magnetosphere. For example, it has been shown that poloidal Pc4 (6.7-22.2 mHz) waves, which are believed to be an example of a second harmonic field line resonance (FLR) [[Hughes and Grard, 1984](#), [Takahashi and McPherron, 1984](#)], are most often seen in the afternoon sector and are associated with localized sources [e.g., [Anderson et al., 1990](#)]. Compressional and poloidal Pc5 (1.7-6.7 mHz) waves are usually observed on the night-side and flanks of the magnetosphere and are related to internal driving sources such as the drift mirror instability [[Hasegawa, 1969](#)] and the drift/drift-bounce resonance instability [[Dai et al., 2013](#), [Southwood and Kivelson, 1982](#), [Southwood et al., 1969](#)]. The internal

sources are expected to generate poloidal waves with high azimuthal wave numbers (high- m). Toroidal Pc5 waves of fundamental mode FLR are more often seen on the dawn and dusk flanks and are often associated with external driving sources such as variations in the solar wind dynamic pressure [Hudson et al., 2004, Kepko and Spence, 2003] and Kelvin-Helmholtz waves at the magnetopause [Anderson et al., 1990, Lin et al., 2014]. The externally driven waves mostly propagate antisunward with low azimuthal wave numbers (low- m). Modeling has shown that many external or internal mechanisms can be viable under appropriate conditions [Kivelson and Southwood, 1985, Lee and Lysak, 1989, Ozeke and Mann, 2001]; however, positively identifying a source mechanism has proven to be rather difficult due to limited measurements.

ULF waves in the ionosphere have been studied using radars. The Super Dual Auroral Radar Network (SuperDARN) is a global network of ground-based high frequency (HF: 3-30 MHz) radars designed primarily for studying ionospheric plasma convection [Chisham et al., 2007]. The line-of-sight velocity measured by SuperDARN radars can be used to detect and monitor ionospheric ULF wave signatures with both high- and low- m [Fenrich et al., 1995, James et al., 2013] and with a total geographical coverage area that cannot be achieved with any other ground- or space-based instrumentation. Based on a new data display technique developed by Ponomarenko et al. [2003], SuperDARN detected ULF wave signatures have been characterized in a few recent studies [e.g., Bland et al., 2014, Norouzi-Sedeh et al., 2015, Sakaguchi et al., 2012]. These studies have been largely limited to the Pc5 range since SuperDARN radars are normally scheduled for 1-min azimuthal sweeps in the common mode [e.g., Bland et al., 2014, Sakaguchi et al., 2012]. ULF wave studies using higher time resolution SuperDARN data have been either case studies [e.g., Shi et al., 2017] and/or statistical studies using one or two radars covering a limited range of latitudes [e.g., Norouzi-Sedeh et al., 2015]. The lack of comprehensive studies could be partially attributed

to the absence of a database of high time resolution observations and no efficient way to identify ULF wave signatures in the SuperDARN data set. Recently, [Bland et al. \[2014\]](#) presented a method for automatically detecting signatures of ULF waves in SuperDARN radar data, which used the Lomb-Scargle periodogram to identify periodic fluctuations in the Doppler velocity. In this study we improve upon this method and apply it to 7 years of high time resolution data from 17 SuperDARN radars in the Northern Hemisphere. We investigate the occurrence and frequency characteristics of ULF wave signatures in the Pc3-5 band and discuss possible source mechanisms for these waves.

3.2 Instrumentation and Event Detection Method

3.2.1 SuperDARN

SuperDARN is an international network consisting of more than 30 low-power HF (8-20 MHz) coherent scatter radars at middle to polar latitudes in both hemispheres that look into Earth's ionosphere [[Baker et al., 2007](#), [Chisham et al., 2007](#)]. The radars measure Doppler shifts of ionospheric irregularities at F region altitudes undergoing $\mathbf{E} \times \mathbf{B}$ plasma drift. When ULF waves pass through the ionosphere, the associated electric field produces a Doppler velocity oscillation that can be measured by the radars.

Normally, the SuperDARN radars are scheduled for 1-min azimuthal sweeps in the “common” mode. The step in azimuth between adjacent beams is 3.24° and the range resolution is 45 km. Sometimes, radars are scheduled to operate in a special mode called “THEMIS” mode, in which a camping beam is sampled at a higher rate of ~ 6 s by interleaving soundings on the camping beam with successive beams of the normal scan. [Figure 3.1](#) shows the fields of view of seventeen Northern Hemisphere SuperDARN radars in Altitude Adjusted Corrected

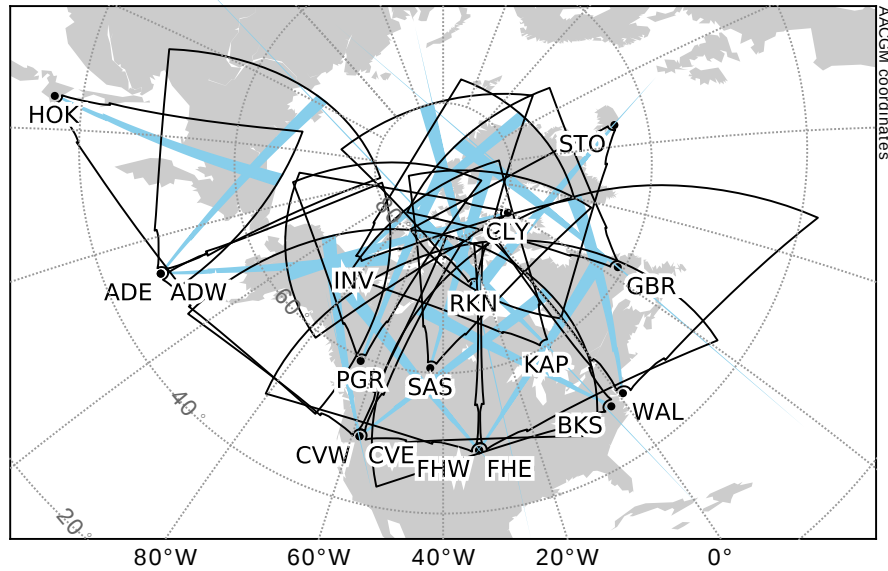


Figure 3.1: Fields of view of seventeen Northern Hemisphere SuperDARN radars in AACGM coordinates. Cyan highlighted beams indicate the camping beams.

Geomagnetic (AACGM) coordinates [Baker and Wing, 1989]. Only radars which have been operated regularly in the THEMIS mode in channel A during the interval 2010-2016 are shown, and the camping beam for each radar is highlighted in cyan. An example period of THEMIS mode observations from beam 6 of the Saskatoon (SAS) radar during 03:30 - 04:30 UT on 16 February 2015 is shown in Figure 3.2. ULF signatures manifest themselves as alternating red and blue stripes in the range-time intensity (RTI) plot in Figure 3.2a with positive (blue-green) values corresponding to motion toward the radar. Figure 3.2b shows the time series of Doppler velocity measured in range gate 13, where wave-like signatures with a few gaps are visible.

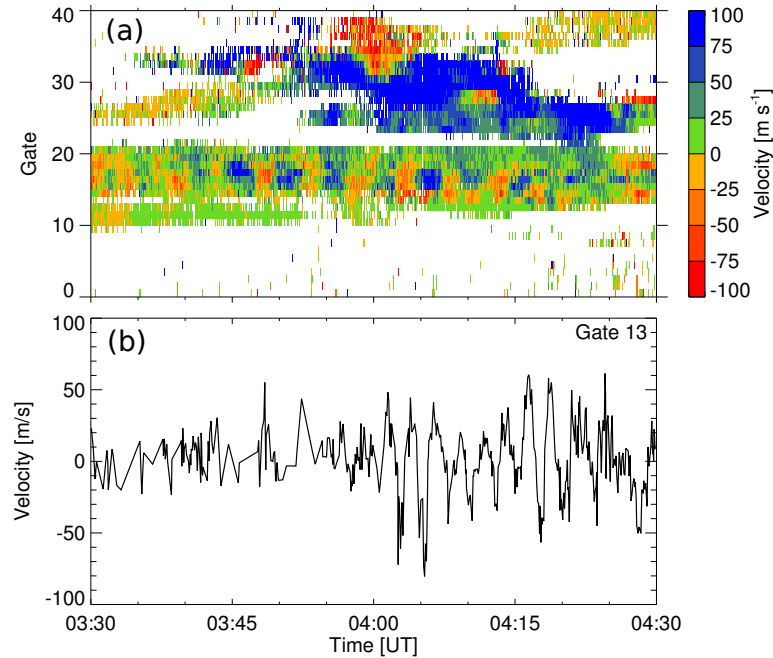


Figure 3.2: Time series of THEMIS mode data measured on beam 6 of the SAS radar on 16 February 2015 from 03:30-04:30 UT: (a) RTI plot of Doppler velocity; (b) Time series of Doppler velocity for range gate 13.

3.2.2 Data Processing and Event Selection

The data processing procedures are similar to those in [Bland et al. \[2014\]](#). First, we select for ionospheric backscatter and reject ground scatter by requiring backscatter to satisfy one of the following conditions: (1) Doppler velocity $|V| \geq 50 \text{ m/s}$; (2) spectral width $W \geq 50 \text{ m/s}$; (3) backscatter is flagged as ionospheric backscatter by the standard SuperDARN ground/ionospheric condition [[Blanchard et al., 2009](#)]. Next, poor quality data are filtered out if backscatter power is less than 3 dB or errors in Doppler velocity or spectral width is greater than 100 m/s. Data from ranges less than 765 km are excluded to minimize contamination from meteor and E region scatter. To search for Pc5 (Pc3-4) signatures, a 1-h (0.5-h) interval is used which is incremented by 15 (7.5) min iteratively. The ionospheric backscatter time series is high-pass filtered by subtracting the median value of a sliding

window of 10 (5) min length for Pc5 (Pc3-4). Further restrictions are applied to the candidate intervals to weaken large data gap effects: (1) the largest time step between consecutive records should be less than 10% of the time interval (i.e., 6 min for Pc5 and 3 min for Pc3-4); (2) the number of measurements should be no less than 400 for Pc5 and 200 for Pc3-4 (i.e., two thirds of the total number assuming a 6 s sampling rate). Qualified intervals are selected as valid ionospheric backscatter measurements and tested for periodic behavior in the Doppler velocity.

Data gaps occur in the radar time series complicating the application of Fourier spectral analysis. While data interpolation can be applied, spurious spikes in the spectrogram are likely to mislead the identification of wave period. We instead applied the Lomb-Scargle periodogram technique for ULF wave signature identification, which is especially advantageous for unevenly sampled signals [Lomb, 1976, Scargle, 1982]. A sufficiently high value of the normalized peak power (NPP) of a Lomb-Scargle periodogram indicates the existence of a wave signature at the associated period. In order to establish the significance of spectral peaks resulting from the Lomb-Scargle periodogram analysis and implement the automated algorithm to search wave signatures, wave period-dependent spectrum thresholds are derived based on a series of numerical experiments. Details about the derivation of threshold NPP can be found in the Appendix.

A ULF wave event is identified if the returned NPP is above the threshold listed in Table 3.1. The event is classified as Pc5 waves if the frequency is within 1.7-6.7 mHz and Pc3-4 waves if within 6.7-40.0 mHz. ULF wave event examples detected by the automated algorithm are shown in Figure 3.3. Left panels are measurements from beam 12 of the Prince George (PGR) radar during 01:00 - 01:30 UT on 25 January 2016 and right panels are measurements from beam 6 of the SAS radar during 03:30 - 04:30 UT on 16 February 2015. Comparing the first two rows shows that the ULF signatures are highlighted after median filtering and

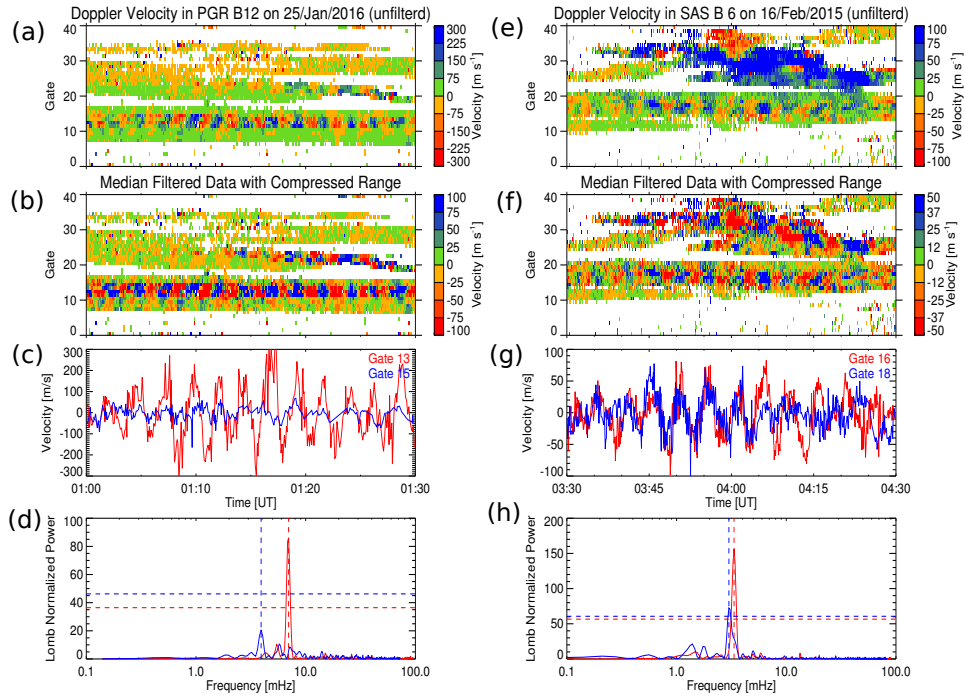


Figure 3.3: Event examples identified by the automatic detection algorithm using data collected on beam 12 of the PGR radar at 01:00-01:30 UT on 25 January 2016 (left) and beam 6 of the SAS radar at 03:30-04:30 UT on 16 February 2015 (right). (From top to bottom) RTI plots of unfiltered Doppler velocity; RTI plots of median filtered Doppler velocity; time series of filtered Doppler velocity for two particular range gates (red and blue); Lomb-Scargle periodograms of data shown in (c) and (g).

expansion of the color scale [Ponomarenko et al., 2003]. The filtered Doppler velocity time series are illustrated for two range gates of each radar in the third row and the Lomb-Scargle periodograms of these signals are shown in the fourth row. ULF oscillations are visible in PGR range gate 13 with ~ 300 m/s amplitude (red) but are not obvious in range gate 15 (blue) as shown in Figure 3.3c. Dimensionless NPP values of 85.95 and 20.70 are returned at frequencies of 6.98 mHz and 3.92 mHz for range gate 13 (red) and range gate 15 (blue) in Figure 3.3d. The horizontal dashed lines indicate the threshold NPPs for these two frequencies, which are 36.45 and 46.25 according to Table 3.1. A Pc4 event is therefore reported for PGR range gate 13 while a null event is reported for range gate 15. Similarly in Figure 3.3h, the Lomb-Scargle periodogram for the SAS radar range gate 16 returns an

NPP of 156.43 which is much greater than the threshold value of 56.61 at 3.34 mHz, while gate 18 returns an NPP of 72.50 which is slightly greater than the threshold of 60.66 at 3.00 mHz. A Pc5 event is therefore reported for SAS range gate 16 and a marginal Pc5 event for range gate 18. These examples illustrate how the algorithm works and the sensitivity of event determination.

Table 3.1: Empirical equations of threshold NPP dependence on wave period with signal length from 66.7% to 133.3% of ideally even sampled length in the Pc3-4 and Pc5 range.

N_{pts}	Pc3-4	N_{pts}	Pc5
200	$NPP = 0.72\tilde{T}_{sin} + 6.8$	400	$NPP = 0.49\tilde{T}_{sin} + 16.7$
250	$NPP = 0.94\tilde{T}_{sin} + 6.3$	500	$NPP = 0.60\tilde{T}_{sin} + 19.0$
300	$NPP = 1.09\tilde{T}_{sin} + 6.5$	600	$NPP = 0.71\tilde{T}_{sin} + 21.2$
350	$NPP = 1.25\tilde{T}_{sin} + 6.6$	700	$NPP = 0.82\tilde{T}_{sin} + 23.8$
400	$NPP = 1.40\tilde{T}_{sin} + 7.0$	800	$NPP = 0.95\tilde{T}_{sin} + 25.0$

A few factors should be noted before statistically analyzing Pc3-5 oscillations in the Doppler velocity with the automated detection algorithm. First, the algorithm searches overlapping 1-h or 0.5-h intervals for ULF wave signatures from each individual range gate of every radar. Events with a long duration and/or a large spatial scale size will be counted multiple times. Second, only ionospheric scatter is analyzed because of difficulties in correctly identifying ground/sea backscatter. This produces a bias toward nightside events when ionospheric backscatter is dominant. Third, this method cannot distinguish between pulsation irregular and pulsation continuous. Finally, large amplitude short-lived Doppler velocity fluctuations other than ULF wave activity are another potential source of contamination.

3.3 Statistical Results

The automated detection algorithm was applied to THEMIS mode measurements collected with SuperDARN radars in the Northern Hemisphere from 2010 to 2016 to identify Pc3-4

events (0.5-h intervals) and Pc5 events (1-h intervals) separately. In total, we identified 5182 Pc3-4 events, 2518 events (48.6%) of which had NPP values greater than 1.2 times their NPP thresholds. For Pc5 events, 7419 out of 17580 events (42.2%) had NPP values greater than 1.2 times their NPP thresholds. In this section, we present statistical results regarding spatial occurrence of the observed ionospheric Pc3-5 ULF signatures, their frequency characteristics, seasonal effects, and dependence on solar wind and geomagnetic conditions.

3.3.1 Spatial Occurrence Distribution

Figure 3.4 shows the Pc3-4 (upper panels) and Pc5 (lower panels) occurrence statistics as a function of magnetic latitude (MLAT) and magnetic local time (MLT) in the Northern Hemisphere. The geomagnetic location of each event is obtained from standard ionospheric backscatter mapping in the AACGM coordinate system, assuming a virtual reflection height of 300 km. The MLAT-MLT maps are organized into bins of 1° MLAT and 0.5 h MLT. Areas where no ionospheric backscatter was observed are shown in white, while black identifies regions where ionospheric backscatter was observed but the observation time in each MLAT-MLT cell was less than 50 h. We exclude those black regions from further analysis due to insufficient backscatter echoes. The left, middle, and right panels show the distributions of ionospheric backscatter occurrence, ULF event occurrence, and the ULF occurrence probability, respectively. Here the ULF occurrence probability is defined as the ULF event occurrence normalized by the ionospheric backscatter occurrence. The upper panels show the results for Pc3-4 events and lower panels show Pc5 events.

Considering first the occurrence of ionospheric backscatter, measurements from 0.5 h intervals (Figure 3.4a) and 1 h intervals (Figure 3.4d) clearly show the coverage provided by the tiers of radars at polar, high, and middle latitudes. Ionospheric backscatter covers most

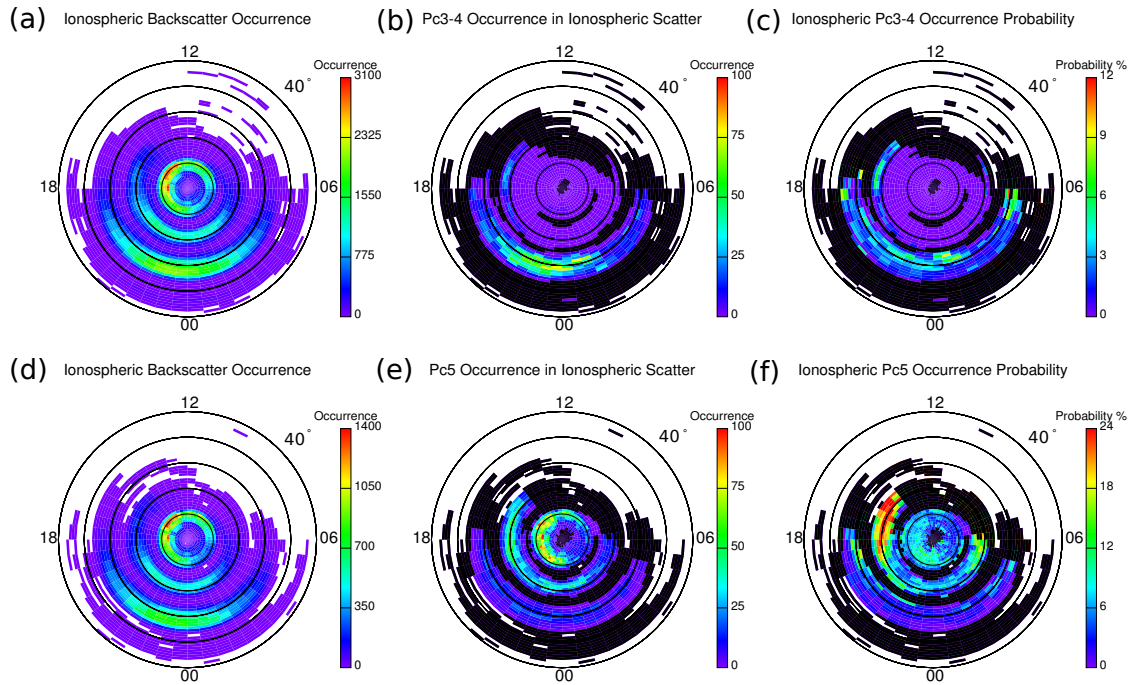


Figure 3.4: MLAT-MLT maps of ionospheric backscatter occurrence (left), occurrence (middle), and occurrence rate (right) of Pc3-4 (upper panels) and Pc5 events (lower panels).

MLTs in the polar region but is mostly seen on the nightside at midlatitudes with an extension to the afternoon sector at high latitudes. Turning now to consideration of ULF wave occurrence, Pc3-4 waves occurred predominantly at midlatitudes on the nightside and at high latitudes on the duskside (Figure 3.4b). Very few events were observed at polar latitudes despite the presence of sufficient ionospheric backscatter there (Figure 3.4a). In contrast to the Pc3-4 events, Pc5 events are detected mostly at high and polar latitudes (Figures 3.4e). Note that Pc5 events (Figure 3.4e) at high latitudes mainly occur in the afternoon and nightside and have a larger longitudinal and latitudinal extent than Pc3-4 events at high latitudes (Figure 3.4b). Finally, the occurrence probability suggests that Pc3-4 events (Figure 3.4c) at high latitudes have a peak occurrence probability of $\sim 7\%$ on the duskside (16-18 MLT) at $67\text{-}68^\circ$ MLAT. While the occurrence rate of Pc3-4 events above 70° is essentially zero at almost all MLTs. At midlatitudes, the occurrence rates of Pc3-4 events are generally greater premidnight than postmidnight, except there is a peak right after midnight above

60° MLAT and another peak at predawn. For Pc5 events, the occurrence probability peaks at $\sim 70^\circ$ MLAT on the duskside (Figure 3.4f). While in the polar region, the Pc5 occurrence rate peaks at $\sim 80\text{-}83^\circ$ MLAT in the premidnight sector. The overall occurrence rate of Pc5 events is much higher than that of Pc3-4 (note different occurrence probability color scales in Figures 3.4c and 3.4f).

3.3.2 Frequency Characteristics

Previous studies suggested that certain ULF frequencies show up more often than others and the variation of frequency with latitude can be used to identify FLR [Fenrich et al., 1995]. We applied the Lomb-Scargle periodogram with an oversampling rate of 4, which leads to a frequency resolution of ~ 0.07 mHz for 1-h intervals and ~ 0.14 mHz for 0.5-h intervals. While the Lomb-Scargle Periodogram technique could be used to identify multiple wave components, in this study we focus on the single component corresponding to the strongest spectrum power for a given time interval and range gate. Since we identify the Pc3-4 and Pc5 events separately with different high-pass filter windows, it is thus possible that a single time interval with multiple frequencies (e.g., harmonic frequencies) could be identified as separate events (e.g., Pc5 and Pc3-4).

The frequency distribution of Pc3-4 events within 6.7-40.0 mHz is shown in Figure 3.5a with the most probable frequency of 11.39 ± 0.14 mHz. The Pc3-4 frequency distribution also shows a steep rise with decreasing frequency below 8 mHz. The lower panels of Figure 3.5 show distributions of the frequency versus MLT (Figure 3.5b) and MLAT (Figure 3.5c). Pc3-4 events preferentially occur on the duskside and nightside (Figure 3.5b) and cover a broader frequency range at midlatitude than at high latitudes where the most probable frequency is ~ 7 mHz (Figure 3.5c). For Pc3-4 events at midlatitudes, a dominant 11 mHz peak exists

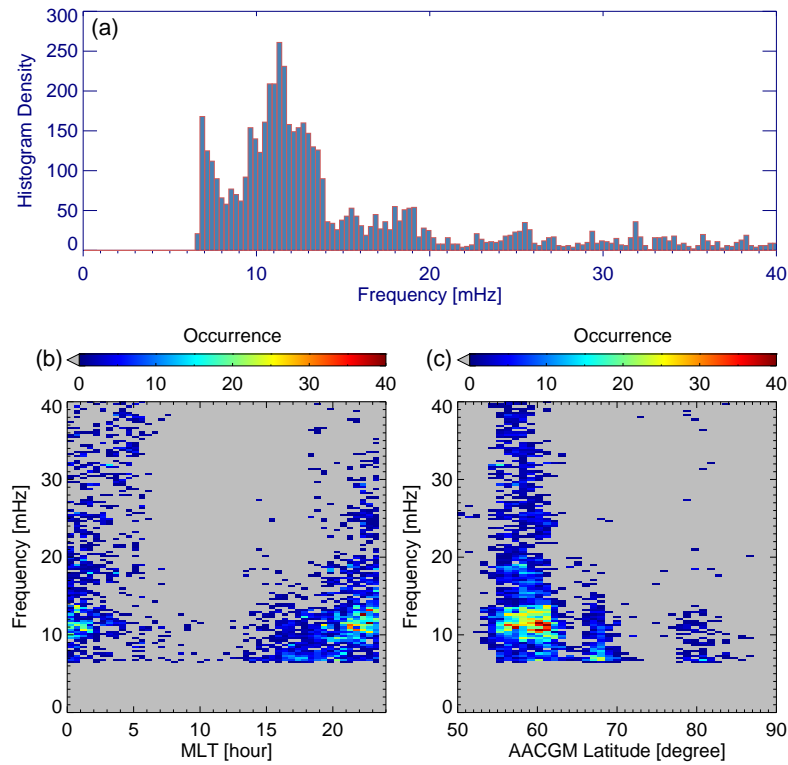


Figure 3.5: Frequency distribution of Pc3-4 events. Upper panel (a) shows the histogram of event frequencies while the lower panels show two-dimensional histograms of (b) frequency versus MLT and (c) frequency versus AACGM latitude.

from 54° to 62° MLAT with no obvious frequency variation with latitude. However, Pc3-4 events observed from high-latitude radars generally have lower frequencies (< 15 mHz) than those from midlatitude radars (Figure 3.5c). We thus put the Pc3-4 events from high-latitude radars into the category of Pc4 events.

Figure 3.6 shows the frequency distribution of Pc5 events in a similar format to Figure 3.5 but in the frequency range of 1.7-6.7 mHz. The most probable frequency is 2.08 ± 0.07 mHz (Figure 3.6a). The majority of Pc5 events were seen with frequencies below 4 mHz and in almost all MLT sectors and at middle, high, and polar latitudes. While the Pc5 events with frequencies above 4 mHz were more often observed on the duskside (Figure 3.6b) at high and middle latitudes (Figure 3.6c). For Pc5 events at high latitudes, the occurrence of lower

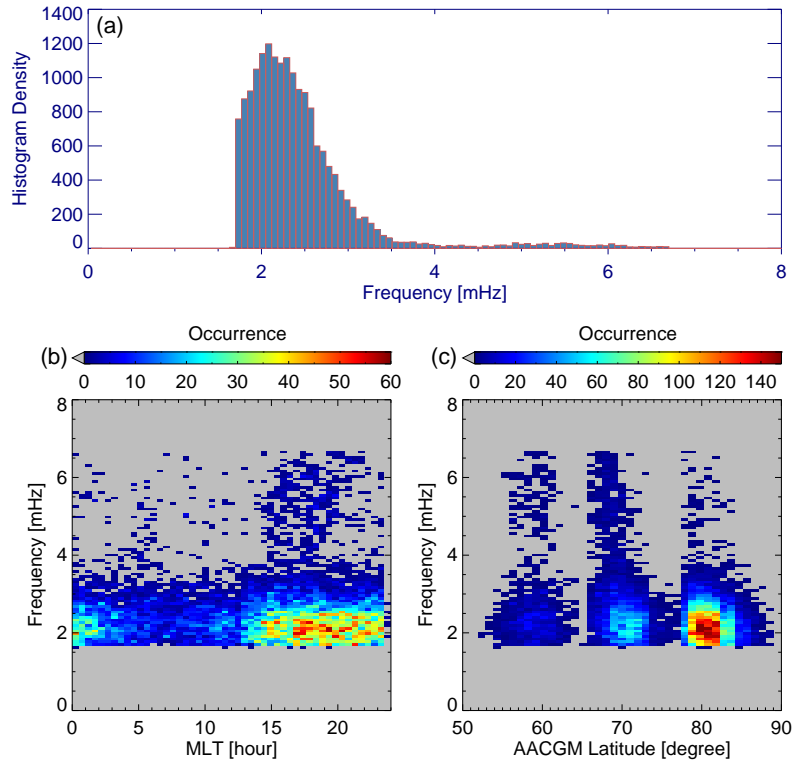


Figure 3.6: Frequency distribution of Pc5 events. Same format as Figure 3.5.

frequency events around 2 mHz peaks above 70 degrees with a clear trend towards lower latitudes as the frequency increases. The 0.07 mHz frequency resolution should be sufficient to resolve discrete frequencies in the Pc5 range, however, we do not find strong evidence of preferred frequencies except perhaps the 2.36 ± 0.07 mHz when considering 506 Pc5 events with NPP values greater than 1.8 times the lower threshold (not shown).

3.3.3 Seasonal Effects

The ionospheric conductivity varies with season and may affect the ionospheric backscatter and ULF wave occurrence. To investigate these effects, ULF events were categorized by season: summer (May-August), equinox (March-April and September-October), and winter

(November-February). Figure 3.7 shows the seasonal dependence of Pc3-4 (upper panels) and Pc5 (lower panels) occurrence rate. The overall spatial coverage of ionospheric backscatter is highest in winter and lowest in summer. The premidnight peak in occurrence of Pc3-4 events at midlatitudes becomes much more prominent at equinox (Figure 3.7b). While the predawn and postmidnight occurrence rate peaks of Pc3-4 events at midlatitudes appear to be features in winter (Figure 3.7c). Turning now to the Pc5 events, the duskside occurrence of Pc5 events peaks at high latitudes and becomes most prominent in winter (Figure 3.7f). For Pc5 events at polar latitudes, the overall occurrence rate is lowest in summer.

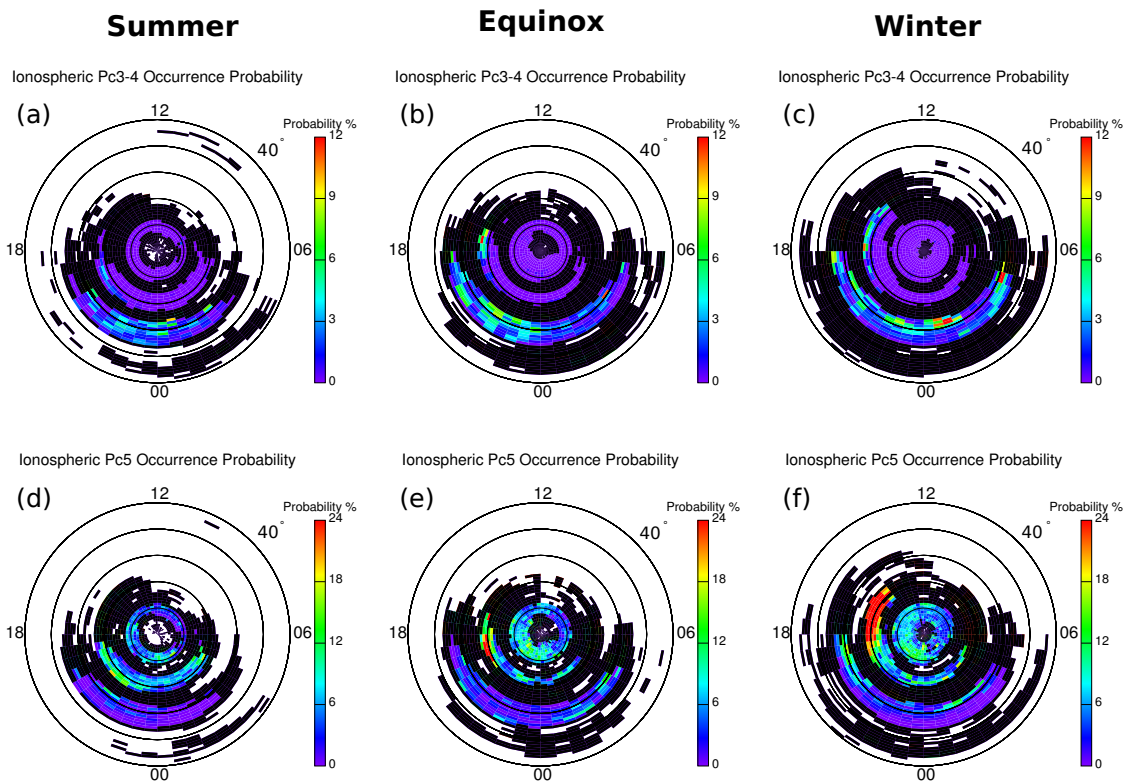


Figure 3.7: MLAT-MLT maps of Pc3-4 (upper panels) and Pc5 (lower panels) event occurrence rate at different seasons: summer (left), equinox (middle), and winter (right).

To better visualize the seasonal behaviors, line plots of Pc3-4 and Pc5 occurrence rate at specific latitudes are shown in Figure 3.8. The overall occurrence rate of polar latitude Pc5 events increases from summer to equinox and winter (Figure 8a). Figure 8b shows an

occurrence rate peak of high latitude Pc5 events during winter (red curve) reaching $\sim 30\%$ at about 15 MLT and another peak during equinox (blue curve) reaching $\sim 18\%$ at dusk. The premidnight occurrence rate peak of Pc3-4 at midlatitudes during equinox is clearly seen from the blue curve in Figure 3.8c.

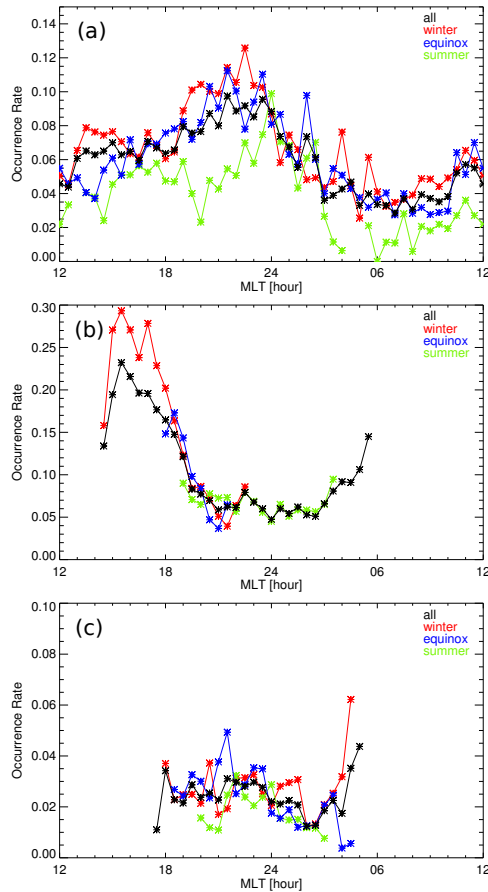


Figure 3.8: Occurrence rate variation as a function of MLT at specific latitudes color coded by season. Occurrence rate variation of (a) Pc5 at polar latitudes ($79-83^\circ$), (b) Pc5 at high latitudes ($66-74^\circ$), and (c) Pc3-4 at midlatitudes ($54-62^\circ$). Black curves indicate data from all seasons.

3.3.4 Solar Wind and Geomagnetic Disturbance Dependencies

The manner in which ULF occurrence varies with solar wind and geomagnetic conditions can provide information about possible generation mechanisms. The Pc3-4 and Pc5 occurrence

rate distributions are sorted by 0.5 h and 1 h average AE index and IMF B_Z . Figure 3.9 shows that Pc4 events at high latitudes tend to occur during low geomagnetic activity as characterized by the AE index and have a higher occurrence rate during northward IMF than southward IMF. At midlatitudes, the premidnight peak in occurrence rate of Pc3-4 events becomes more prominent with increasing AE index value and during southward IMF. Figure 3.10 shows the dependence for Pc5 events in a similar format. Pc5 events at high latitudes tend to occur during low geomagnetic activity and northward IMF, which is similar to Pc4 events at high latitudes as shown in Figure 3.9.

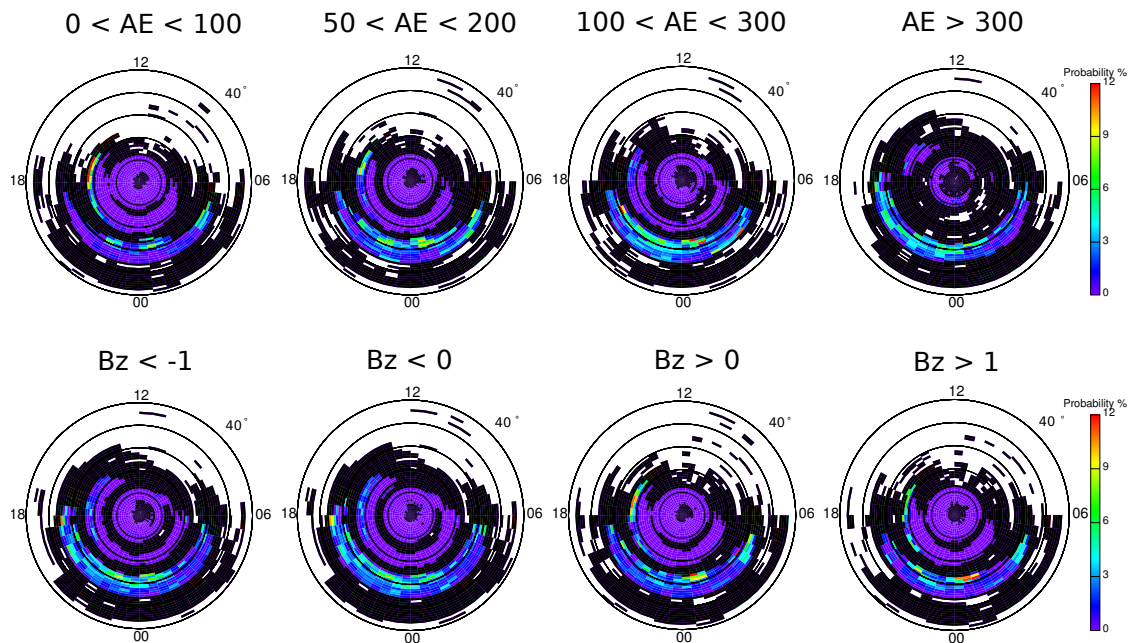


Figure 3.9: MLAT-MLT maps of Pc3-4 event occurrence rate sorted by 0.5 h average AE index (upper panels) and IMF B_Z (lower panels).

To further help identify sources that generate categories of ULF waves, we show the time evolution of average AE index, SYM-H index, and IMF B_Z before and after the occurrence time of ULF wave events in Figure 3.11. The results are shown in histograms color coded by count of the Pc3-4 events (left, 4274 0.5-h intervals) at midlatitudes ($54\text{--}64^\circ$) on the nightside ($\text{MLT} \geq 18$ or $\text{MLT} \leq 6$), the Pc4 events (middle, 409 0.5-h intervals) at $64\text{--}70^\circ$ MLAT and

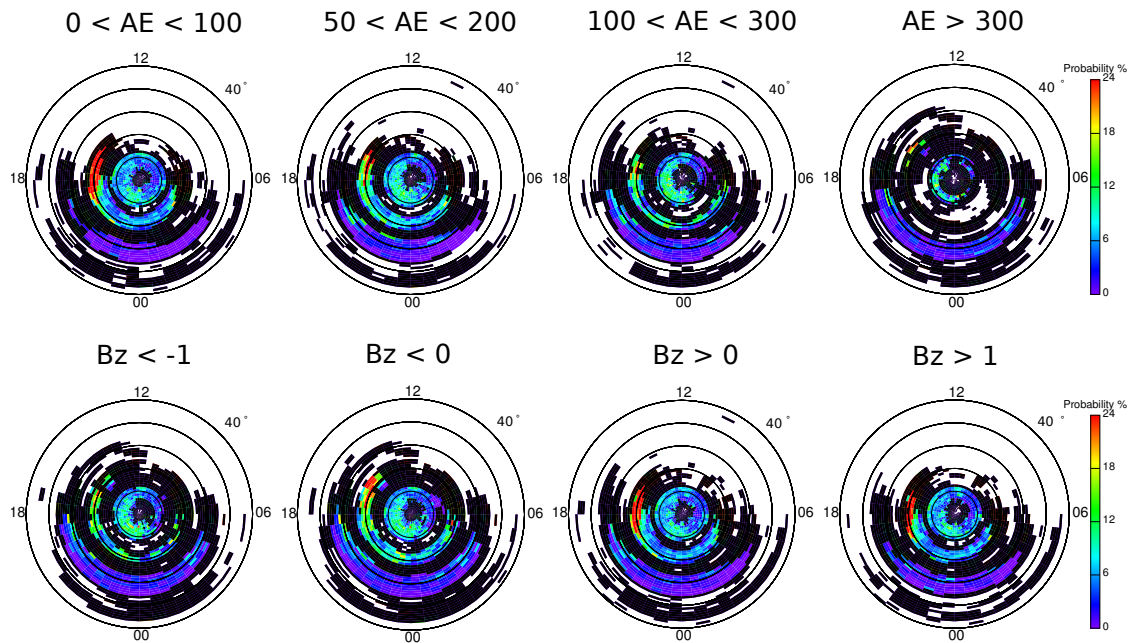


Figure 3.10: MLAT-MLT maps of Pc5 event occurrence rate sorted by 1 h average AE index (upper panels) and IMF B_Z (lower panels).

14-20 MLT, and the Pc5 events (right, 2249 1-h intervals) at high latitudes ($65-75^\circ$) in the dusk sector (14-20 MLT). Solid black lines show the variation with time of the median values of AE index (top row), SYM-H index (middle row), and IMF B_Z (bottom row). Note that the time span in Figure 3.11 varies with category of ULF wave depending on the type of geomagnetic activity that appears to be most relevant to it, e.g., substorms, storms. Nightside Pc3-4 events (left) tend to occur at a sharp increase of AE index, a decrease of SYM-H index, and during southward IMF, which suggests that substorm activity favors their occurrence. By contrast, Pc4 events (middle) tend to occur at an AE minimum with a sharp AE drop several hours before the events and during positive IMF B_Z . The gradual increase of SYM-H index suggests that these events occur during the recovery phase of geomagnetic storms. Pc5 events (right) mostly occur during quiet geomagnetic intervals as characterized by the AE and SYM-H indices and during positive IMF B_Z . These quiet conditions usually occur long before the events and last several hours after the events.

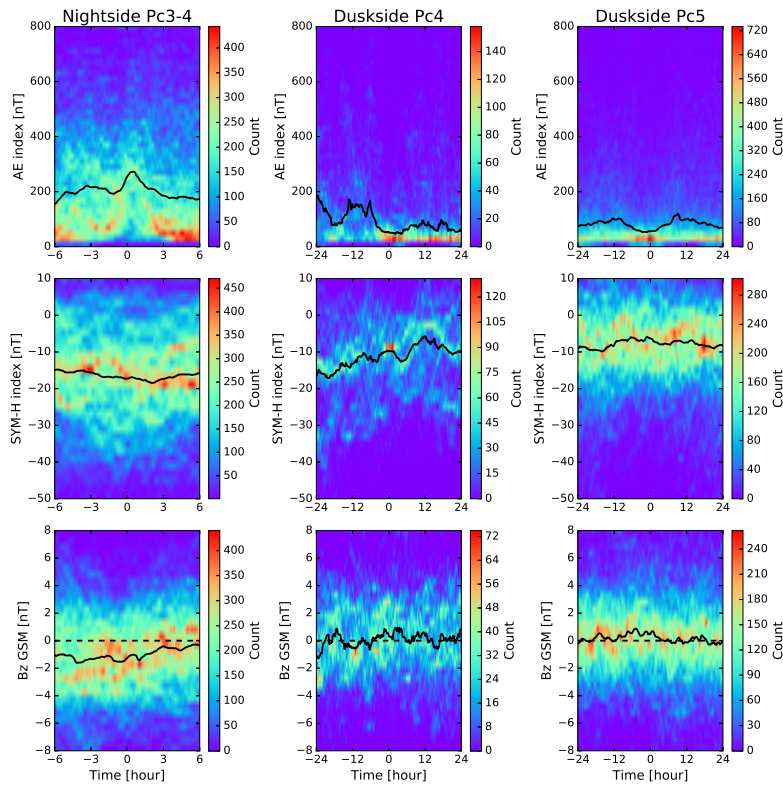


Figure 3.11: Time evolution of histograms of average AE index (top row), SYM-H index (middle row), and IMF B_Z (bottom row) for Pc3-4 events at midlatitudes on the nightside (left column), Pc4 (middle column) and Pc5 (right column) events at high latitudes on the duskside. Zero hour indicates the ULF wave event occurrence time. Solid black lines show the median AE (top row), SYM-H index (middle row), and IMF B_Z (bottom row) values. Dashed black lines in the bottom row indicate zero IMF B_z .

3.4 Discussion

In this study, an automated detection algorithm has been used to identify ionospheric signatures of Pc3-4 and Pc5 waves in seven years of high time resolution SuperDARN radar data. Pc5 events were found to occur predominantly at high and polar latitudes with a most probable frequency of 2.08 ± 0.07 mHz while Pc3-4 events were relatively more common at midlatitudes on the nightside with a most probable frequency of 11.39 ± 0.14 mHz. At high latitudes, Pc4-5 wave occurrence probability peaks in the dusk sector and in winter

during low geomagnetic activity and under northward IMF. At midlatitudes, the occurrence probability of Pc3-4 events peaks premidnight and during equinox with this tendency being more prominent with increasing AE index value and under southward IMF.

For Pc5 events in the polar region, classical Pc5 waves observed at lower latitudes on closed field lines are rarely observed beyond the auroral oval inside the polar cap by ground magnetometers [Kozyreva et al., 2016]. Since our algorithm cannot distinguish between irregular and continuous pulsations, it is likely that these events are distinct polar cap pulsations of ~ 2 mHz, designated as $\text{Pi}_{cap}3$ pulsations [Yagova et al., 2004]. These polar Pc5/ $\text{Pi}_{cap}3$ events show a seasonal effect with the lowest occurrence rate in summer (Figure 3.8a). At high latitudes, Pc5 events were observed from afternoon to postmidnight (Figure 3.4e) with a peak occurrence rate in the duskside ionosphere (Figure 3.4f). This diurnal variation is generally consistent with a recent study using data from the SuperDARN Tasman International Geospace Environment Radars (TIGER) and the magnetometers located on Macquarie Island by Norouzi-Sedeh et al. [2015]. The majority of ULF signatures seen in the radar data from a beam pointing toward the southern AACGM pole were detected between 15 and 21 local time in their study. The duskside occurrence rate peak of Pc5 events in our study becomes most prominent in winter as shown in Figure 3.7 and Figure 3.8b. Both the diurnal and seasonal behaviors of Pc5 occurrence at high and polar latitudes imply that decreased ionospheric conductivity leads to increased amplitude of wave electric fields in the ionosphere [Pilipenko et al., 2012, Sakaguchi et al., 2012]. The occurrence of ULF waves as measured by ground magnetometers is also sensitive to ionospheric conductivity, but in the opposite sense with HF radar measurements [see Figure 11 in Sakaguchi et al., 2012], i.e., the occurrence peak is on the dayside [Baker et al., 2003].

Most Pc5 events in this study occurred in the range 1.7-4.0 mHz with a most common frequency of ~ 2 mHz, which is consistent with previous statistical results using SuperDARN

data [Bland et al., 2014, Norouzi-Sedeh et al., 2015]. Discrete frequencies at 1.6, 2.1, 2.9, and 3.3 mHz were reported by Norouzi-Sedeh et al. [2015] and earlier at 1.3, 1.9, 2.6, and 3.4 mHz by Samson et al. [1991] and Ruohoniemi et al. [1991]. However, in this study the frequency distribution is continuous in the Pc5 range and no discrete frequencies were observed. The source of ~ 2 mHz dominance at almost all latitudes is unclear, but possible source mechanisms include linkage to dominant frequencies in solar wind perturbations [Kepko and Spence, 2003, Stephenson and Walker, 2002], and magnetospheric cavity/waveguide modes of natural frequencies varying with changes in the cavity topology [Baker et al., 2003, Kivelson and Southwood, 1985].

Pc4 events were mostly observed at 66-70° MLAT from the afternoon to the premidnight sector (Figure 3.4b). The radially bounded but longitudinally extended Pc4 events observed during quiet geomagnetic intervals have been reported previously and were attributed to localized instabilities [Anderson et al., 1990, Engebretson et al., 1992]. The sharp AE drop several hours before the Pc4 events and gradual increase of SYM-H index are consistent with ULF waves occurring during the late recovery phase of geomagnetic storms [Dai et al., 2015, Engebretson et al., 1992]. This indicates a connection between the occurrence of Pc4 events with prior substorm activity and the decay of the ring current. Numerous studies have shown that poloidal ULF waves are capable of efficiently interacting with energetic particles in the ring current and the radiation belt during both geomagnetically quiet and active times [Chi and Le, 2015, Dai et al., 2015, Hudson et al., 2004, James et al., 2013]. A small convection electric field at quiet times and plasmaspheric refilling during the recovery phase of geomagnetic storms might play roles in the generation of internal instabilities that drive these waves. Localized effects such as the drift or drift-bounce resonance instability are suggested to be possible sources of Pc4 pulsations at high latitudes in the duskside ionosphere.

Pc3-4 events at midlatitudes were seen on the nightside with a premidnight peak in the occurrence rate. The left column of Figure 3.11 shows that they occurred at a sharp increase of AE index, a decrease of SYM-H index and southward IMF. This evidence indicates that they are most likely Pi2 and Pc3-4 pulsations associated with magnetotail dynamics during geomagnetically active times such as substorm onsets or intensification. The fact that the premidnight occurrence rate peak becomes most prominent during equinox also supports this idea [Russell and McPherron, 1973]. Multiple frequency peaks in the frequency histogram shown in Figure 3.5 and no obvious frequency variation at midlatitudes from 54° to 62° MLAT suggest they might be associated with plasmaspheric cavity mode/virtual resonances as reported by Teramoto et al. [2016] and Shi et al. [2017].

Finally, it is possible that some of the identified Pc3-5 events in this study are ionospheric plasma drift fluctuations [Cousins and Shepherd, 2012] which are not related to MHD waves, because our algorithm cannot differentiate between them. To definitely determine whether these events are MHD waves, we would need nearby ground magnetometer and/or conjugate spacecraft measurements, which is beyond the scope of this study and will be explored in future studies.

3.5 Summary and Conclusions

In this study, ionospheric ULF wave signatures in the Pc3-5 band (1.7-40.0 mHz) were surveyed in the SuperDARN THEMIS mode data from 2010 to 2016 by means of the Lomb-Scargle periodogram. Empirical relationships between the Lomb-Scargle periodogram NPP and associated wave period are derived based on a series of numerical experiments to guide automated detection of ULF signatures. Statistics regarding the occurrence and frequency distributions, seasonal effects, solar wind condition and geomagnetic activity level depen-

dence have been studied. The main results are summarized as follows: (1) Pc5 events occur predominantly at high and polar latitudes while Pc3-4 are relatively more common at mid-latitudes on the nightside; (2) The most probable Pc5 (Pc3-4) frequency is ~ 2 (11) mHz; (3) At high latitudes, Pc4-5 occurrence probability peaks in the dusk sector and in winter and is elevated during northward IMF and quiet geomagnetic intervals with decreasing geomagnetic activity; (4) At midlatitudes, Pc3-4 occurrence probability peaks at premidnight and becomes most prominent at equinox with a preference for southward IMF conditions and increasing geomagnetic disturbance level. An internal wave-particle interaction source is suggested for Pc4 events at high latitudes in the duskside ionosphere and a source associated with the magnetotail dynamics during active geomagnetic times for Pc3-4/Pi2 events at midlatitudes in the nightside ionosphere. Our results also emphasize the role of ionospheric conductivity in controlling ULF wave occurrence.

Acknowledgments

X. Shi was supported by NSF grant AGS-1341918 and NASA Headquarters under the NASA Earth and Space Science Fellowship Program - Grant 80NSSC17K0456 P00001. E. C. Bland was supported by the Research Council of Norway/CoE under contract 223252/F50. M. D. Hartinger was supported by NASA NNX17AD35G. The authors acknowledge the use of SuperDARN data, which are freely available through the SuperDARN website at Virginia Polytechnic Institute and State University (<http://vt.superdarn.org/>). SuperDARN is a collection of radars funded by national scientific funding agencies of Australia, Canada, China, France, Italy, Japan, Norway, South Africa, United Kingdom and the United States of America.

Chapter 4

Long-Lasting Poloidal ULF Waves Observed by Multiple Satellites and High-Latitude SuperDARN Radars

X. Shi¹, J. B. H. Baker¹, J. M. Ruohoniemi¹, M. D. Hartinger¹, K. R. Murphy², J. V. Rodriguez^{3, 4}, Y. Nishimura^{5, 6}, K. A. McWilliams⁷, and V. Angelopoulos⁸

¹Department of Electrical and Computer Engineering, Virginia Tech, Blacksburg, VA, USA.

²NASA Goddard Space Flight Center, Greenbelt, Maryland, USA.

³Cooperative Institute for Research in Environmental Sciences, University of Colorado Boulder, Boulder, CO, USA.

⁴National Centers for Environmental Information, National Oceanic and Atmospheric Administration, Boulder, CO, USA.

⁵Department of Electrical and Computer Engineering and Center for Space Sciences, Boston University, Boston, MA, USA

⁶Department of Atmospheric and Oceanic Sciences, University of California Los Angeles, CA, USA

⁷Institute of Space and Atmospheric Studies, University of Saskatchewan, Saskatoon, Saskatchewan, Canada

⁸Department of Earth, Planetary and Space Sciences, University of California Los Angeles, CA, USA

Shi, X., Baker, J. B. H., Ruohoniemi, J. M., Hartinger, M. D., Murphy, K. R., Rodriguez, J. V., et al. (2018). Long-lasting poloidal ULF waves observed by multiple satellites and high-latitude SuperDARN radars. *Journal of Geophysical Research: Space Physics*, 123, 8422–8438. <https://doi.org/10.1029/2018JA026003>

Abstract

Poloidal ultra-low frequency (ULF) waves between 5-10 mHz were observed by multiple satellites and three high-latitude Super Dual Auroral Radar Network (SuperDARN) radars during the recovery phase of a moderate geomagnetic storm on Jan 24-27, 2016. The long-lasting ULF waves were observed in the magnetic field and energetic particle flux perturbations during three successive passes by two Geostationary Operational Environmental Satellites (GOES) through the dayside magnetosphere, during which plasmasphere expansion and re-filling were observed by two Time History of Events and Macroscale Interactions during Substorms (THEMIS) probes. The radial magnetic field oscillation was in phase ($\sim 180^\circ$ out of phase) with the northward (southward) moving proton flux oscillation at 95 keV, consistent with high-energy drift-bounce resonance signatures of protons with second harmonic poloidal standing Alfvén waves. The longitudinal extent of the waves approached 10 hours in local time on the dayside and gradually decreased with time. High-time resolution (~ 6 s) data from three high-latitude SuperDARN radars show that the wave intensification region

was localized in latitude with a radial extent of ~ 135 - 225 km in the subauroral ionosphere. No signature of these waves were observed by ground-based magnetometers colocated with the GOES satellites suggesting that the poloidal waves were high- m mode and thus screened by the ionosphere. During this interval one of the THEMIS probes observed a bump-on-tail ion distribution at 1-3 keV which we suggest is the source of the long-lasting second harmonic poloidal ULF waves.

4.1 Introduction

Ultra-low frequency (ULF) oscillations in the radial magnetic field (B_r) and azimuthal electric field (E_φ) are known as poloidal waves. Since the azimuthal electric field of poloidal waves is aligned with the particle drift motion, they are capable of efficiently interacting with particles in the ring current and the radiation belt [e.g., [Murphy et al., 2014](#), [Zong et al., 2009](#)]. Among the harmonics of poloidal standing Alfvén waves, the second harmonic mode is among the most frequently observed ULF waves in the Earth’s magnetosphere [[Hughes and Grard, 1984](#), [Takahashi and McPherron, 1984](#)]. The second harmonic standing Alfvén waves are usually observed in the Pc4 band (6.7-22.2 mHz) and are most often seen in the afternoon sector during both geomagnetically quiet and active times [[Dai et al., 2015](#), [Min et al., 2017](#)]. Statistical surveys of these waves show that they are usually radially bounded but longitudinally extended [[Anderson et al., 1990](#), [Engebretson et al., 1992](#)].

ULF waves with a strong toroidal component (B_φ and E_r) are usually believed to be driven by external sources such as periodic variations or sudden changes in the solar wind dynamic pressure [[Hudson et al., 2004](#)] and Kelvin-Helmholtz (KH) waves at the magnetopause [e.g., [Claudepierre et al., 2008](#), [Lin et al., 2014](#)]. Poloidal Alfvén waves with high azimuthal wave numbers (high- m) are often attributed to internal localized instabilities such as the drift-

bounce resonance instability [e.g., [Southwood and HUGHES, 1983](#)]. For the drift-bounce resonance instability as a source of ULF waves, free energy usually comes from two sources: (1) unstable particle populations in the ring current (bump-on-tail distribution) [[Baddeley et al., 2004](#), [Liu et al., 2013](#), [Takahashi et al., 2018b](#)] and (2) a radial gradient of particle phase space density [[Dai et al., 2013](#), [Min et al., 2017](#), [Oimatsu et al., 2018](#)].

One category of poloidal ULF waves is characterized by their long lifetime from several hours to days [e.g., [Korotova et al., 2016](#), [Le et al., 2017](#), [Sarris et al., 2009](#)]. Most previous studies on the long-lasting poloidal ULF waves were focused on wave properties in the magnetosphere [[Korotova et al., 2016](#), [Le et al., 2017](#), [Min et al., 2017](#), [Takahashi et al., 2018b](#)]. Interestingly, the waves were usually monochromatic and observed during low geomagnetic activity after a geomagnetic storm or within the storm recovery phase, as summarized in [Table 4.1](#). It is thought that a small convection electric field and plasmaspheric refilling during the recovery phase play key roles in the generation of the internal instabilities that drive these waves during these periods [[Anderson et al., 1990](#), [Dai et al., 2015](#), [Liu et al., 2013](#), [Sarris et al., 2009](#), [Shi et al., 2018b](#)]. Generally ground-based magnetometers are unable to detect these high- m waves due to ionospheric screening effects [[Hughes and Southwood, 1976](#)]; hence, simultaneous observations of these waves in the magnetosphere and conjugate ionosphere are rare, perhaps also in part owing to their localized radial extent and low occurrence rate [[Anderson et al., 1990](#), [Shi et al., 2018b](#)].

In this study, we analyze a long-lasting poloidal ULF wave using multi-point satellite and Super Dual Auroral Radar Network (SuperDARN) high frequency (HF) radars during the recovery phase of a storm on Jan 24-27, 2016. We characterize the radial and azimuthal extent of the waves observed in the magnetosphere and ionosphere and provide evidence of the wave excitation source.

4.2 Instrumentation and Analysis

The primary instruments used in this study are the GOES 13 ($\sim 75^\circ$ west geographic longitude) and GOES 15 ($\sim 135^\circ$ west geographic longitude) geostationary satellites, Time History of Events and Macroscale Interactions during Substorms (THEMIS) D and E (THD and THE, respectively) spacecraft [Angelopoulos, 2008], three high-latitude SuperDARN radars [Chisham et al., 2007], and two ground magnetometers from the Canadian Array for Realtime Investigations of Magnetic Activity (CARISMA) ground-based North America magnetometer array [Mann et al., 2008]. The solar wind and interplanetary magnetic field (IMF) data are obtained from the WIND satellite and OMNI database [King and Papitashvili, 2005]. The geomagnetic data are from the World Data Center for Geomagnetism in Kyoto.

4.2.1 Satellite Missions

The GOES data used in this study are the measurements of the magnetic field vector and energetic particle fluxes. The magnetic field data are from the Fluxgate Magnetometer (FGM) with a sampling rate 0.512 s [Singer et al., 1996]. The magnetic field vector is expressed in local mean-field-aligned (MFA) coordinates with components denoted as B_r (outward, perpendicular to the mean magnetic field), B_ϕ (eastward, perpendicular to the mean magnetic field), and $B_{//}$ (parallel to the mean magnetic field) [Takahashi et al., 1990]. The mean magnetic field data are obtained by a boxcar running average over 30 min. After rotating into the MFA coordinates, the magnetic field perturbations in the parallel direction ($\Delta B_{//}$) are obtained by subtracting the 30 min-averaged mean magnetic field data. The GOES proton flux data come from the Magnetospheric Proton Detector (MAGPD) which measures protons at five differential energy channels centered at 95, 140, 210, 300, and 575 keV. We especially draw on the data collected with the detector telescopes mounted in the

north/south direction with field-aligned pitch angles [Rodriguez, 2014]. In order to clearly see the ULF wave modulation in the particle flux j , we use the residual fluxes defined by $\delta j = (j - j_{average})/j_{average}$, where $j_{average}$ is the 20 min running average of j , similar to previous studies [e.g., Claudepierre et al., 2013].

The electron density inferred from THEMIS spacecraft potential data are used to provide the plasmaspheric context. Magnetic and electric field data expressed in MFA coordinates from the THD and THE spacecraft are used in this study. The magnetic field data are provided by the FGM instrument [Auster et al., 2008]. The electric field and spacecraft potential data are obtained from the Electric Field Instrument (EFI) [Bonnell et al., 2008]. The electric field data are spin-fit, 3 s-averaged vector samples constructed from the spin-plane components by assuming no electric field along the background magnetic field.

4.2.2 Ground-based Instruments

For ionospheric wave observations, we use the line-of-sight (LOS) velocity data from SuperDARN HF coherent scatter radars. SuperDARN is an international network consisting of more than 30 low-power radars operating at 8-20 MHz from middle to polar latitudes in both hemispheres that look into Earth’s ionosphere [Baker et al., 2007, Chisham et al., 2007]. The radars measure Doppler shifts of ionospheric irregularities at F region altitudes undergoing $\mathbf{E} \times \mathbf{B}$ plasma drift. When ULF waves pass through the ionosphere, the associated electric field produces a Doppler velocity oscillation that can be measured by the radars. Normally, the SuperDARN radars are scheduled for 1-min azimuthal sweeps in the “common” mode. The step in azimuth between adjacent beams is 3.24° and the range resolution is 45 km. Sometimes the radars are scheduled to operate in higher cadence “THEMIS” mode, in which a camping beam is sampled at a higher rate of ~ 6 s by interleaving soundings on the camp-

ing beam with successive beams of the normal scan. For this study, THEMIS mode data from three high-latitude SuperDARN radars - Prince George (PGR), Saskatoon (SAS), and Kapuskasing (KAP) - are used to analyze ionospheric ULF wave signatures.

Two ground magnetometers with a sampling rate of 0.5 s are used in this study; one located at Fort Simpson (FSIM) from the CARISMA magnetometer array, and the other at Sanikiluaq (SNKQ) from the CANadian Magnetic Observatory System (CANMOS). In order to check on wave activity in the 5-10 mHz band, the ground magnetometer data were detrended by subtracting the 30 min running average.

4.2.3 Signal Processing

Dynamic power spectra of magnetic and electric field data from satellites, Doppler velocity data from SuperDARN radars, and magnetic field data from ground magnetometers are used in this study for wave analysis in the frequency domain. The dynamic power spectra are obtained by applying a running 30 min Fast Fourier Transform (FFT) with 25 min window overlap. The frequency resolution is about 0.56 mHz and the Nyquist frequency is 83.3 mHz from the lowest time resolution (~ 6 s) across all the data sets. Prior to taking the FFT, the data are interpolated for regular spacing at the specified time step and a Hanning window is applied to reduce spectral leakage.

4.2.4 Instrument Locations

The locations of the various space and ground instruments used in this study are shown in Figure 4.1. The upper panels show the locations of the GOES (black), THE (blue) and THD (red) spacecraft in the X-Y plane (Figure 4.1a) and X-Z plane (Figure 4.1b), in Solar Magnetic (SM) coordinates. The diamonds (GOES) and asterisks (THEMIS) identify

the locations of the satellites at 23:00 UT on Jan 24, 2016. As can be seen in Figure 4.1b, all measurements from four satellites were made above the magnetic equator with GOES 15 located at about 4° and GOES 13 at $\sim 10^\circ$ off the magnetic equator. The lower panel (Figure 4.1c) shows a map in Altitude Adjusted Corrected Geomagnetic (AACGM) coordinates [Baker and Wing, 1989, Shepherd, 2014] with the positions of the spacecraft and ground instruments indicated. Included are the two selected ground magnetometers (black dots); SuperDARN radar fields of view (FOV) and camping beams of PGR (cyan), SAS (green), and KAP (orange); and ionospheric footprints of the GOES satellites (black diamonds), THE (blue asterisk) and THD (red asterisk) using the Tsyganenko 1996 (T96) magnetic field model [Tsyganenko and Stern, 1996] at 23:00 UT. The red regions inside the radar camping beams indicate the range gates where ULF wave signatures were most frequently observed in this study. Unless specified, the magnetic coordinates used hereafter are AACGM.

4.3 Observations

In this section, we describe the interplanetary and geomagnetic conditions during the wave event and analyze the wave properties in the magnetosphere and ionosphere to obtain the spatial extent and spectral features of long-lasting poloidal ULF waves observed by multiple satellites and high-latitude SuperDARN radars. This event was initially identified in the ULF event data base from SuperDARN high time resolution data which was built using an automated detection method based on the Lomb-Scargle periodogram technique described by Shi et al. [2018b].

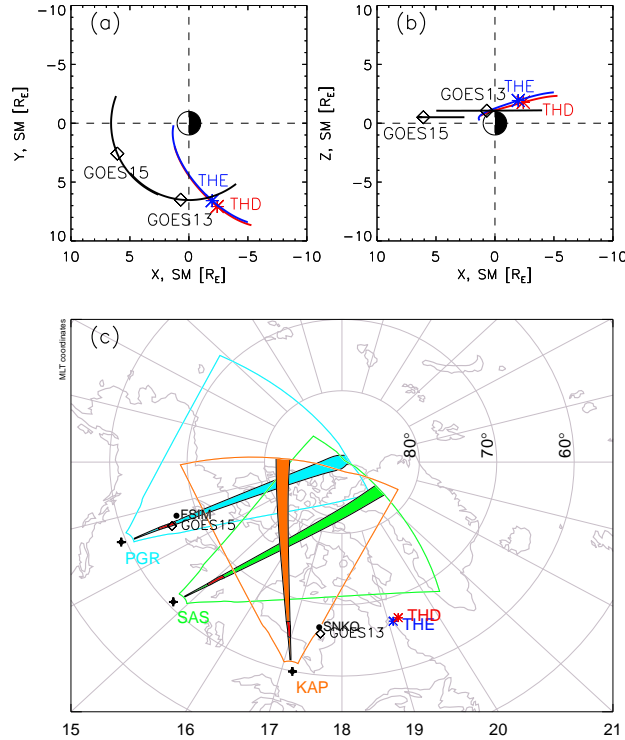


Figure 4.1: Locations of various space and ground instruments. The upper panels show the locations of GOES 13 and 15 (black curve), THE (blue curve) and THD (red curve) spacecraft in (a) the X-Y plane and (b) the X-Z plane in Solar Magnetic coordinates from 20:00 UT on 24 January 2016 to 02:00 UT on 25 January 2016. The lower panel (c) shows the locations of ionospheric footprints of GOES 13 and 15 (black diamonds), THE (blue asterisk) and THD (red asterisk), ground magnetometers (black dots), and SuperDARN radar FOV and camping beams of PGR (cyan), SAS (green), and KAP (orange) in AACGM coordinates at 23:00 UT on 24 January 2016.

4.3.1 Event Overview

Figure 4.2 provides an overview of the interplanetary and geomagnetic conditions covering the wave event during a moderate geomagnetic storm with a minimum SymH value of ~ -100 nT. The interplanetary data come from OMNI and are overlaid with 1 h-shifted data (dashed purple curves) from the Wind satellite to fill in data gaps in OMNI. The cyan shaded regions identify the time intervals of interest, when GOES satellites observed monochromatic poloidal ULF waves in the dayside magnetosphere. Note that approximately two hours before

the start of the wave event there was a substorm onset at $\sim 18:00$ UT on 24 January 2016. The AE index reached a maximum of ~ 1000 nT at $\sim 19:00$ UT and gradually decreased to ~ 250 nT at 20:00 UT. The onset of the wave event appears to coincide with a solar wind dynamic pressure pulse at 20:00 UT. It was geomagnetically quiet ($AE < 100$ nT) during the second pass of the dayside magnetosphere by the GOES satellites, the IMF was slightly northward and dominated by a positive B_x at ~ 6 nT.

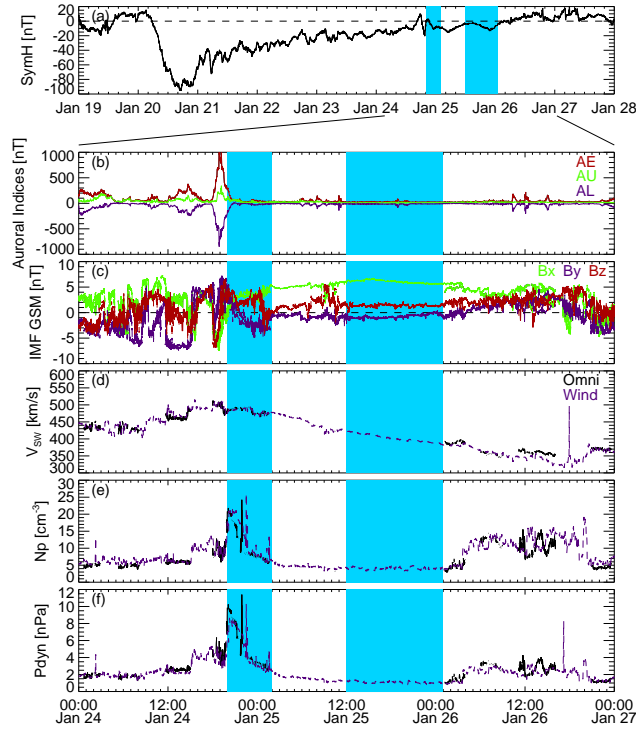


Figure 4.2: Geomagnetic indices and interplanetary parameters covering the wave event: (a) SymH index on 19-28 January 2016; (b) AE (red), AU (green), and AL (blue) indices, (c) OMNI/WIND IMF Bx, By and Bz components in the Geocentric Solar Magnetospheric coordinate system, (d) solar wind speed, (e) solar wind proton density, and (f) solar wind dynamic pressure on 24-27 January 2016. The cyan shaded regions identify the time intervals of interest.

Before we analyze ULF wave properties in the magnetosphere, it is important to know whether and how the magnetospheric plasma density varies during the course of the wave event, as changes in the plasma density will result in changes in the eigenfrequency of the

magnetic field lines and the associated wave frequency. Figure 4.3 shows profiles of the electron density inferred from the spacecraft potential versus L shell value during four successive outbound passes from 23-27 January 2016. Figure 4.3 shows evidence of both plasmasphere expansion and refilling from THD (Figure 4.3a) and THE (Figure 4.3b) observations during the recovery phase of the geomagnetic storm. Plasmaspheric boundary layer (PBL) or plume structure was observed during the second outbound pass on Jan 24-25, 2016 (red curve) by both satellites as a bump in the electron density profile reaching $\sim 100 \text{ cm}^{-3}$ around $L \sim 5.5$.

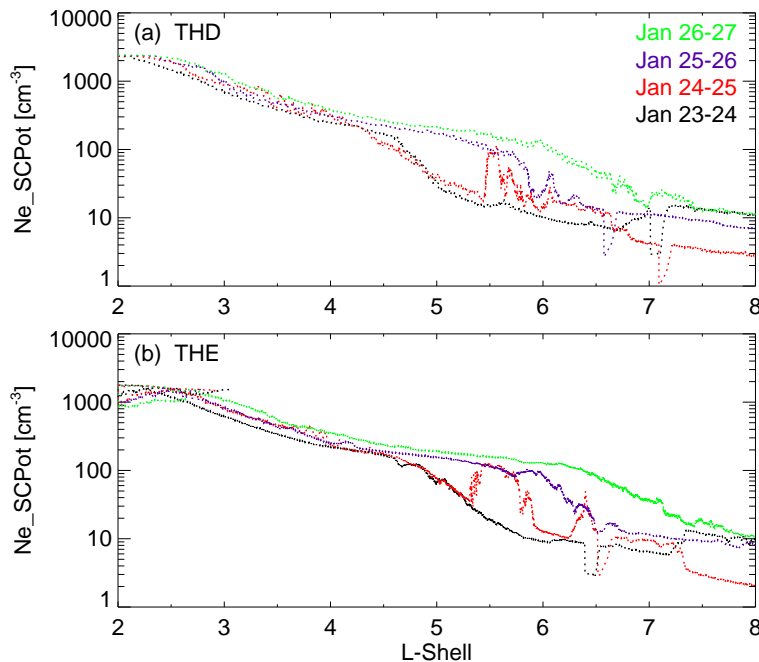


Figure 4.3: Plasmaspheric context from two THEMIS spacecraft during the recovery phase of the geomagnetic storm. Each panel shows profiles of electron density inferred from spacecraft potential versus L shell value during four successive outbound passes of (a) THD and (b) THE from 23 to 27 January 2016.

4.3.2 Wave Properties in the Magnetosphere

We first examine waves observed by geostationary satellites as shown in Figure 4.4 (GOES 13) and Figure 4.5 (GOES 15). The red (black) vertical lines identify local noon (midnight). The green (yellow) vertical lines identify local dawn (dusk). Episodes of monochromatic ULF waves between 5-10 mHz were observed in the dayside magnetosphere by both satellites over 2-3 days. The wave power is strongest in the radial magnetic field (B_r) consistent with a poloidal mode. At the onset of this wave event ($\sim 20:00$ UT), GOES 13 was located in the afternoon sector and GOES 15 was located at ~ 10.5 MLT. The azimuthal extent of these waves was up to 10 hours in MLT on the dayside as can be seen from the second pass on 25-26 January and gradually decreased to a few hours around noon in the third pass. The wave frequency generally decreases as the satellites move from the morning sector and into the noon and dusk sectors and from the first pass to the third pass of the dayside magnetosphere. Both the diurnal and daily frequency decreases can be explained by the mass density change. The afternoon sector often has a higher plasma density than the morning sector. In addition, in this event plasmaspheric plume structure was observed around dusk (Figure 4.3). The refilling of the plasmasphere evident in Figure 4.3 resulted in an increase in electron density which may account for the steady decrease in wave frequency. While heavy ion mass loading during plasmasphere refilling may also contribute to the wave frequency change [Fraser et al., 2005], the mass loaded plasma density data is not available from spacecraft measurements in this study.

Note that a higher harmonic was observed during the second pass of GOES 13 and is more clearly seen in the toroidal component (B_φ). The fact that the azimuthal magnetic field has strong wave power at similar frequencies to the radial magnetic field suggests coupling of the poloidal and toroidal modes, which is common in the inhomogeneous media of the Earth's magnetosphere. The differences in wave frequency and spatial extent of the monochromatic

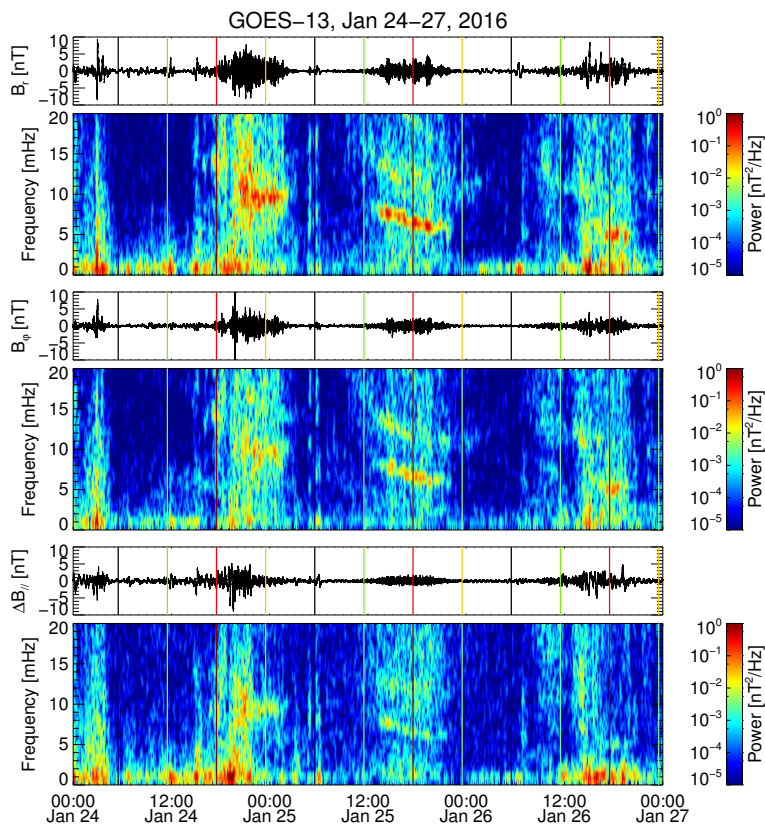


Figure 4.4: The magnetic field data from GOES 13 in the Mean-Field-Aligned coordinate system and the dynamic power spectra from 24 to 27 January 2016. The red (black) vertical lines identify local noon (midnight). The green (yellow) vertical lines identify local dawn (dusk).

poloidal waves observed by GOES 13 and GOES 15 are probably due to their different orbits, recalling that GOES 15 was closer to the magnetic equator than GOES 13 (Figure 4.1b).

We now consider the waves observed by the two THEMIS satellites near dusk. During the outbound pass of THD and THE, both satellites observed monochromatic ULF waves in the radial and azimuthal electric field components at 6-8 mHz. Note that the ULF electric field perturbation amplitudes, periods, and phases measured by the THEMIS EFI short and long booms agree well, suggesting that the THEMIS double probe electric field measurement is not affected by contamination during this interval. The waves lasted for

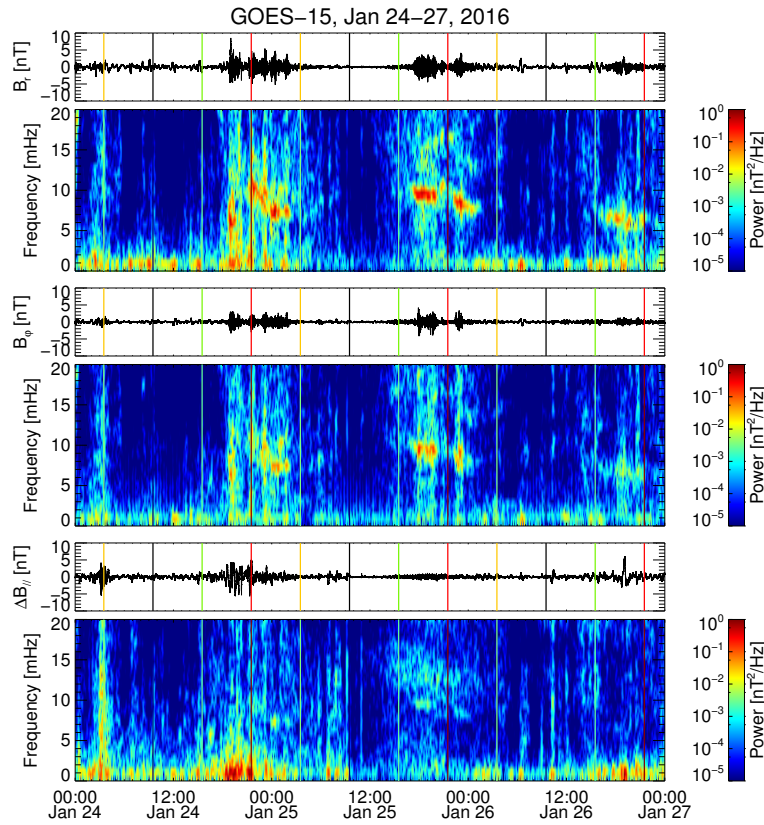


Figure 4.5: The magnetic field data from GOES 15 in the Mean-Field-Aligned coordinate system and the dynamic power spectra from 24 to 27 January 2016.

several wave cycles around 19 MLT (vertical red lines in Figure 4.6). THD (left column), located closer to the magnetic equator, passed through the wave active region a few minutes before THE, and observed a stronger wave power in the radial electric field (E_r) while THE (right column) observed a stronger electric field power in the azimuthal component (E_ϕ). Since both satellites were located off the magnetic equator, the wave power at the same frequency from the radial magnetic field (B_r) is very weak. We will demonstrate later in the Discussion that the observations in the magnetosphere are consistent with a second harmonic standing Alfvén wave.

Unlike the GOES satellites which observed wave activity during three successive passes of the dayside magnetosphere, THEMIS only observed wave activity during the first outbound

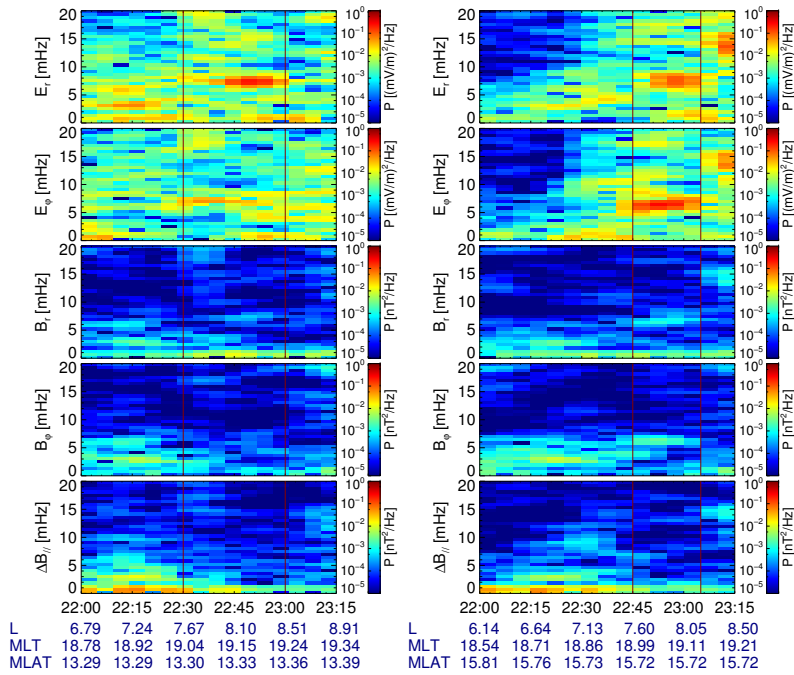


Figure 4.6: The dynamic power spectra of electric and magnetic field components in the Mean-Field-Aligned coordinate system from THD (left) and THE (right) at 22:00-23:15 UT on 24 January 2016.

pass near the dusk flank. Figure 4.1 shows that during the wave event THD and THE were located ~ 1.5 h eastward of GOES 13 which continued observing monochromatic poloidal waves until after ~ 21 MLT. By contrast, GOES 15 located ~ 4 h eastward of GOES13 did not see the waves after 18 MLT during the first pass. Neither GOES 13 or GOES 15 observed wave signatures between 5-10 mHz after dusk on either the second or third passes. Hence, the wave active region extended past dusk only during the first pass and thus THD and THE could only observe the wave during this initial period of wave activity.

4.3.3 Wave Properties in the Ionosphere

After examining wave properties in the magnetosphere, we now analyze wave signatures in the ionosphere observed by ground-based SuperDARN radars and magnetometers. Figure 4.7

shows ionospheric ULF wave signatures observed by the PGR radar in the camping beam 12 from 2016-01-24/23:00 UT to 2016-01-25/02:00 UT. The alternating green and yellow stripes starting at about 23:10 UT on January 24 over range gate 10-15 were signatures of flow velocity modulations by ULF waves in the ionosphere as shown in the Range-Time Intensity (RTI) plot (Figure 4.7a). An enhancement in flow velocity (300 m/s) at 01-02 UT on January 25 was localized within 3-5 range gates (135-225 km) and merged with lower frequency (< 5 mHz) waves at higher latitudes, probably Pc5 pulsations in the auroral region. Time series of LOS velocity from range gate 12 is shown in Figure 4.7b and its dynamic power spectrum is shown in Figure 4.7c. Monochromatic waves at $\sim 7-8$ mHz with weaker wave power were observed before 2016-01-25/01:00 UT, waves with stronger power were seen after 2016-01-25/01:00 UT at similar frequencies. Figure 4.7d shows time series of LOS velocity from successive range gates. The progression from top to bottom panel corresponds to decreasing magnetic latitude (first number in the square brackets) at similar magnetic longitude (second number in the square brackets). Wave intensifications are isolated to a few range gates, the location of the intensification varies with time generally propagating to lower latitudes.

Besides the PGR radar, the SAS and KAP radars observed monochromatic ionospheric ULF wave signatures between 5-10 mHz, as shown in Figure 4.8. RTI plots in Figure 4.8 (left) show that these monochromatic ULF waves were mostly observed equatorward of lower frequency Pc5 waves at higher latitudes and lasted for a few hours as long as ionospheric backscatter persisted. Time series of LOS velocity in 0.5 h intervals incremented by 7.5 min from individual radar and range gate were analyzed separately for spectral power from 2016-01-24/20:00 UT to 2016-01-25/04:00 UT, using the Lomb-Scargle periodogram technique reported in Shi et al. [2018b]. Figure 4.8d shows the frequency of wave events from the three radars as a function of MLT. Wave events were mostly observed in the afternoon sector and

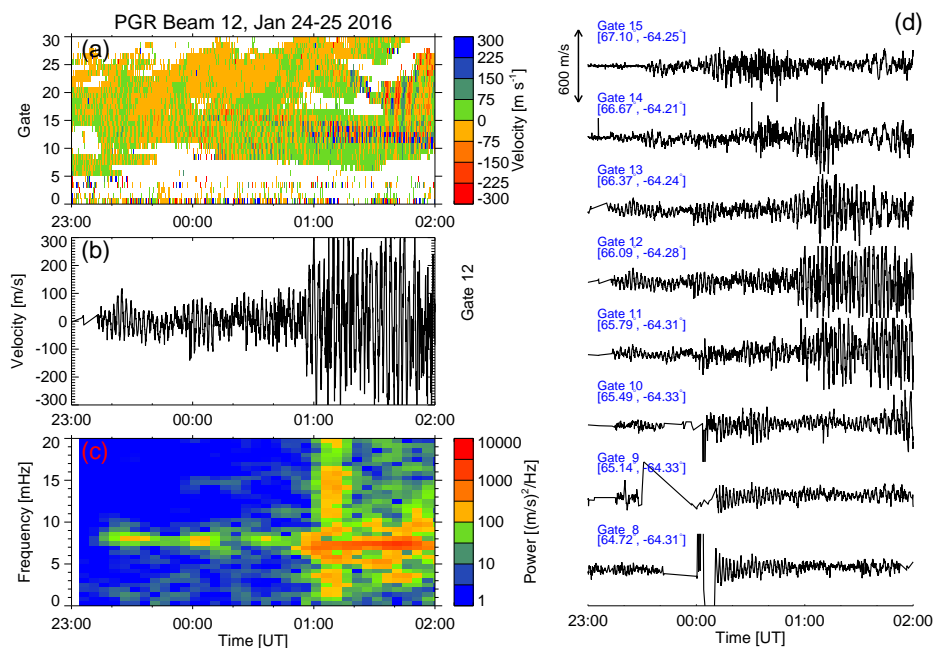


Figure 4.7: Ionospheric ULF signatures observed by the PGR radar in the camping beam 12 from 2016-01-24/23:00 UT to 2016-01-25/02:00 UT. (a) The range-time intensity plot; (b) Doppler velocity time series from range gate 12 of beam 12; (c) Dynamic power spectrum of data from panel (b); (d) Doppler velocity time series from range gate 8-15 of beam 12.

the wave frequency did not show a clear variation with MLT. A clear trend of wave frequency decrease with increasing magnetic latitude is observed in Figure 4.8e, which is a prominent feature of the field line eigenfrequency variation with latitude.

Knowledge of the azimuthal wave number is important for understanding the ULF wave excitation mechanism and wave interactions with the ambient plasma. Data from individual SuperDARN radars can be analyzed for information on m number by comparing measurements across multiple beam directions. In standard operation mode, a scan repeats once a minute. In THEMIS mode, a scan repeats once every two minutes while the THEMIS beam is sample every 6 s. Thus, high-time resolution data are available in one beam direction but this is unsuitable for resolving m value. There is scope for combing THEMIS beam data from multiple radars provided the sampling is dense enough in longitude.

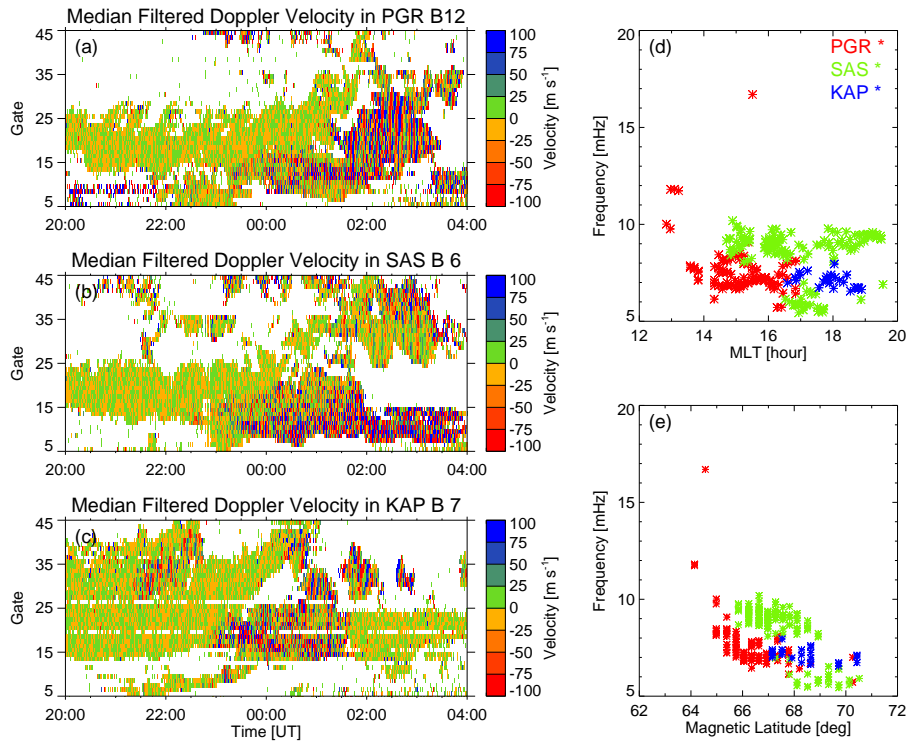


Figure 4.8: (Left) The range-time intensity plot for (a) PGR, (b) SAS, and (c) KAP radar from 2016-01-24/20:00 UT to 2016-01-25/04:00 UT. (Right) Frequency versus (d) MLT and (e) magnetic latitude distribution of wave events.

We thus investigate the azimuthal wave number using data from the SNKQ and FSIM ground magnetometers near the ionospheric footprint of GOES 13 and GOES 15. Radially polarized (poloidal) Alfvén waves should be observed in the Y component by ground magnetometers due to the 90° polarization rotation by the ionosphere [Hughes and Southwood, 1976]. However, no long-lasting ULF waves between 5–10 mHz were observed on the dayside by either ground magnetometer in the Y component, as seen in Figure 4.9. This suggests that monochromatic ULF waves between 5–10 mHz observed by the satellites in the dayside magnetosphere and by SuperDARN HF radars in the dayside ionosphere were high- m mode waves which were screened by the ionosphere from detection by ground magnetometers. Note that we do see higher harmonic waves between 10–15 mHz on the dayside from 2016-01-25/12:00 UT to 2016-01-26/00:00 UT at the SNKQ station, which is consistent with

observations from GOES 13 (Figure 4.4). These waves are probably low- m higher harmonic toroidal waves which are less affected by screening and can be detected on the ground. We applied the cross-phase analysis (not shown) of Waters et al. [1991] using the Bx components from two closely spaced meridional ground magnetometers. Preliminary results do indicate the existence of higher harmonic toroidal modes. Detailed consideration of the toroidal mode in this event is left to future work.

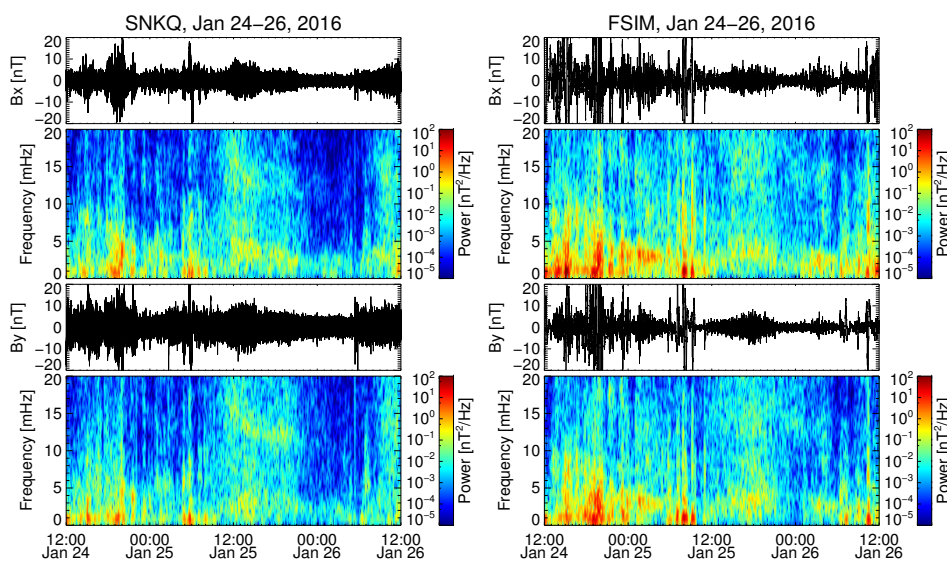


Figure 4.9: Time series and dynamic power spectra of ground magnetic field northward (Bx) and eastward (By) components observed at the SNKQ (left) and FSIM (right) stations from 24 to 26 January 2016.

4.3.4 Wave Spatial and Spectral Characteristics

To characterize the wave spatial extent and spectral properties, the wave frequency distribution as a function of MLAT and MLT from the SuperDARN radars, GOES satellites and THEMIS spacecraft from 2016-01-24/20:00 UT to 2016-01-25/04:00 UT are shown in Figure 4.10. Each symbol represents the frequency of the spectral peak power from 0.5 h interval satellite and radar data. The wave activities are mainly localized at $\sim 64\text{--}70^\circ$ MLAT in

the afternoon sector in the subauroral region, as indicated by the Special Sensor Ultraviolet Spectrographic Imager (SSUSI) data from the Defense Meteorological Satellite Program (DMSP) satellites (not shown). The wave frequency from GOES 13 (diamond) stays stable at ~ 10 mHz from 14-22 MLT and is consistent with the SAS (triangle) radar measurements just poleward of GOES 13. The ionospheric footprint of GOES 15 (square) was located close to the PGR (x) radar camping beam measurements and they recorded similar wave frequencies at 6-8 mHz at $\sim 66^\circ$ MLAT and 14-16 MLT. The THD (asterisk) and THE (circle) spacecraft observed ULF waves at a lower frequency (~ 6.5 mHz) which is closer with the KAP (cross) and SAS radar measurements at higher latitudes. Despite the uncertainties in mapping of radar backscatter and of spacecraft measurements to the ionosphere, the 2D wave frequency distribution shows the consistency of space and ground-based observations of the monochromatic ULF waves in the dayside magnetosphere and ionosphere. It also illustrates the importance of using multi-point coordinated satellite and radar observations to obtain information about the radial and azimuthal extent of the waves at the time of occurrence. In this case the long-lasting high- m ULF waves were localized in the radial direction but extended in the azimuthal direction across the dayside.

4.4 Discussion

In this section, we summarize the observed wave properties and discuss possible mechanisms for wave excitation and the impact these waves have on magnetospheric plasma via wave-particle interactions.

The very strong wave power in the radial magnetic field observed by GOES 13 and GOES 15 near the magnetic equator suggests these waves were second harmonic poloidal mode (antisymmetric). As shown in Figure 4.1 from Dai et al. [2013], the fundamental poloidal

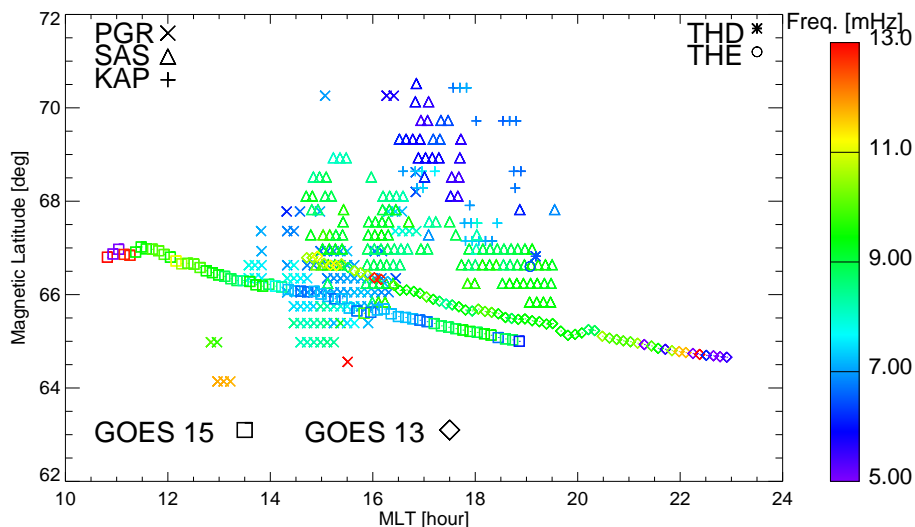


Figure 4.10: Frequency distribution as a function of magnetic latitude and MLT for ULF wave events from three high latitude SuperDARN radars, GOES and THEMIS satellites from 2016-01-24/20:00 UT to 2016-01-25/04:00 UT.

mode (symmetric) with a magnetic node near the magnetic equator is not detectable as a magnetic field oscillation. Furthermore, THD and THE located 13° - 16° off the magnetic equator observed very strong electric field oscillations but very weak magnetic field oscillations (Figure 4.6). This suggests the THEMIS satellites were located close to the magnetic field node of the second harmonic wave.

Although the observed ULF waves share similarities with giant pulsations (Pgs) [Chisham, 1996, Motoba et al., 2015, Wright et al., 2001], (i.e. localized in latitude, monochromatic waveform, high- m , poloidal mode, usually observed during geomagnetically quiet times, driven by internal instabilities), the ULF waves observed in this study are not likely Pgs which are more often observed in the morning sector in the auroral zone and can be detected by ground magnetometers with $|m| \sim 20 - 40$. Our observed ULF waves are generally constrained to the dayside and extended to post-dusk in the subauroral region on the first day; there is also no clear signature of the wave in ground-based magnetometer observations

(Figure 4.9). Fortunately, high-latitude SuperDARN HF radars detected the ionospheric signatures of these high- m waves and the latitudinal extent of the wave active region is estimated to be 135-225 km in the ionosphere (Figure 4.7). With the aid of SuperDARN observations, we are also able to distinguish waves with different sources, e.g., lower frequency waves from the auroral region and long-lasting higher frequency waves in the subauroral region (Figure 4.7a). In addition, multiple radar observations provide information on the wave azimuthal extent and wave property variations with magnetic latitude and longitude (Figure 4.8d-e and Figure 4.10). In summary, we conclude that the observations of narrow-band ULF waves in the magnetosphere and ionosphere are consistent with a high- m mode second harmonic standing Alfvén wave with a wide longitudinal extent but narrow radial extent.

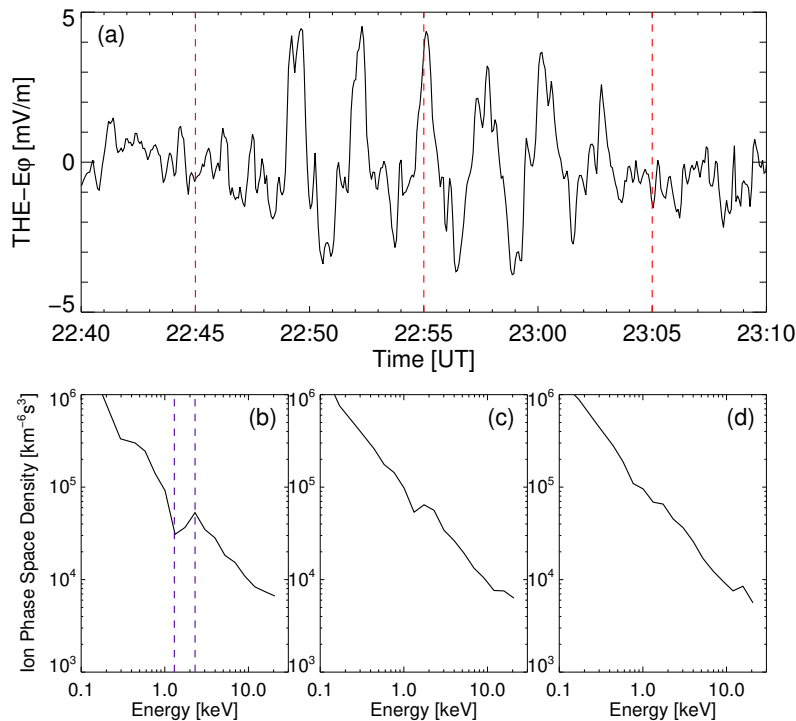


Figure 4.11: (a) The azimuthal electric field from 22:40 UT to 23:10 UT on 24 January 2016 and ion phase space density as a function of energy measured at about (b) 22:45 UT, (c) 22:55 UT, and (d) 23:05 UT by the THE spacecraft.

As mentioned in the Introduction, high- m poloidal standing Alfvén waves are often driven by internal instabilities, such as the drift-bounce resonance. To gain insights into internal sources of free energy for wave excitation, we examine the ion phase space density (f) as a function of energy (W) to determine if a bump-on-tail distribution exists [e.g., [Baddeley et al., 2005](#)]. The Electrostatic Analyzer (ESA) [[McFadden et al., 2008](#)] measures phase space density as functions of energy, pitch angle and time. We obtained omnidirectional (pitch angle averaged) ion phase space density from THE ESA measurements and present in Figure 4.11 (bottom panels). The azimuthal electric field measured by the THE spacecraft is shown in Figure 4.11a. The positive energy slope ($\partial f/\partial W > 0$) marked between blue dashed lines in the ion distribution function identifies a bump-on-tail structure which contains "free energy" in the "bump" that can be fed to a wave when the drift frequency (ω_d) and bounce frequency (ω_b) of ions match the wave frequency (ω) through the drift-bounce resonance condition [e.g., [Southwood, 1976](#)]:

$$\omega - m\omega_d = N\omega_b \quad (4.1)$$

where m is the azimuthal wave number and N is an integer ($0, \pm 1, \pm 2, \dots$) representing the harmonic mode of the wave. We estimate proton ω_d and ω_b based on the following formulas given by [Hamlin et al. \[1961\]](#) and [Chisham \[1996\]](#):

$$\omega_b \approx \frac{\pi\sqrt{W}}{\sqrt{2m_p}LR_E(1.3 - 0.56\sin\alpha_{eq})} \quad (4.2)$$

$$\omega_d \approx -\frac{6WL(0.35 + 0.15\sin\alpha_{eq})}{qB_sR_E^2} + \frac{90(1 - 0.159K_p + 0.0093K_p^2)^{-3}L^3\sin\phi}{B_sR_E^2} \quad (4.3)$$

where W is the proton energy, m_p is the proton mass, L is the proton's L-shell, R_E is the radius of the Earth, α_{eq} is the proton equatorial pitch angle, B_s is the equatorial surface

magnetic field strength, K_p is the planetary magnetic activity index, ϕ is the azimuthal angle of the particle measured anticlockwise from local midnight ($\phi = mlt/24. \times 360.$). The first term on the right hand side of equation (3) represents gradient-curvature drift and the second $\mathbf{E} \times \mathbf{B}$ drift under a model magnetospheric potential [Maynard and Chen, 1975, Yeoman and Wright, 2001].

The proton bounce and drift frequencies at the location of the bump $W = 2 \text{ keV}$ are estimated to be $\omega_b = 0.0196739 \text{ rad/s}$ ($f_b = \omega_b/2\pi = 3.13119 \text{ mHz}$), $\omega_d = -8.19879 \times 10^{-5} \text{ rad/s}$ ($f_d = \omega_d/2\pi = -0.0130488 \text{ mHz}$), using $L = 7.6$, $\alpha_{eq} = 30^\circ$, $Kp = 1$, $mlt = 19$ for THE observed the bump-on-tail distribution at 2016-01-24/22:45 UT. For low-energy ions interacting with the second harmonic poloidal wave through drift-bounce resonance, we have $N = 1$ and the m value is estimated to be -258 (negative value represents westward propagation) based on equation (1) and wave frequency $\omega = 2\pi f = 0.04084 \text{ rad/s}$ ($f = 6.5 \text{ mHz}$). Takahashi et al. [2018b] reported Van Allen Probes observations of second harmonic poloidal standing Alfvén waves propagating westward with $m \sim -200$. The proton phase space density in their study also exhibited a bump-on-tail structure occurring in the 1-10 keV energy range. Seen from Table 4.1, a similar event has been reported by Liu et al. [2013] in the plasmasphere boundary layer. Since the high- m modes are usually observed with $|m| \sim 100$, previous studies seldom observed any ground signatures due to ionospheric screening effects. Baddeley et al. [2005] examined the cause and effect relationship between the unstable magnetospheric particle populations and conjugate ionospheric high- m ULF waves measured by the Doppler Pulsation Experiment (DOPE) HF sounder. In this study, multiple ground-based SuperDARN HF radars provide 2D wave properties in the ionosphere (Figure 4.10) and nicely fill the gap between observations from space-based satellites and ground-based magnetometers.

High- m poloidal mode waves may also be excited via high-energy ion drift-bounce resonance

with an inward radial gradient of ion phase space density, e.g., $\partial f/\partial L < 0$. Previous studies [e.g., [Takahashi et al., 1990](#)] show that the radial magnetic field oscillation should be 180° (0°) out of phase with the southward (northward) moving proton flux oscillations in the resonant energy associated with a second harmonic poloidal standing Alfvén wave observed at the magnetic equator. At energies away from the resonance, the cross phase of ion flux oscillation and the radial magnetic field oscillation should approach $\pm 90^\circ$. Signatures of drift-bounce resonance in ion flux oscillations at 95-300 keV with field-aligned pitch angles (α) from GOES 13 are shown in Figure 4.12. Namely, $\sim 180^\circ$ phase shift between B_r (Figure 4.12a), southward moving ($\alpha \sim 140^\circ$) ion residual flux at 95 keV (red line in Figure 4.12b), $\sim 90^\circ$ phase shift for 140 keV ions (green line in Figure 4.12b). Also, the amplitude of ion residual flux oscillations peaks at 95 keV energy channel. For ions moving nearly parallel to the magnetic field ($\alpha \sim 2^\circ$) from the detector telescope 7 (Figure 4.12c), the 95 keV residual flux leads B_r by a few degrees which is consistent with the pitch angle dependence reported by [Takahashi et al. \[2018b\]](#) in Figure 12. Another approach to estimate m value draws on assuming the 95 keV ions are in drift-bounce resonance ($N=-1$) with the observed poloidal wave. The m number is estimated to be -152 in this case, which is still consistent with a high- m mode wave. However, we are unable to check the radial phase space density profile at the resonant energy using GOES satellite measurements. Thus, we cannot exclude or confirm the possibility of wave excitation involving drift-bounce resonance at high energy with an inward radial gradient of ring current protons.

Finally, we discuss possible explanations for why these high- m poloidal waves could last for days and are observed on the dayside with a wide azimuthal extent but a localized radial extent. Both event analysis and statistical studies suggest these waves are mostly observed during low geomagnetic times within the recovery phase of a geomagnetic storm [e.g., [Engebretson et al., 1992](#), [Le et al., 2017](#), [Sarris et al., 2009](#), [Shi et al., 2018b](#)]. Previous

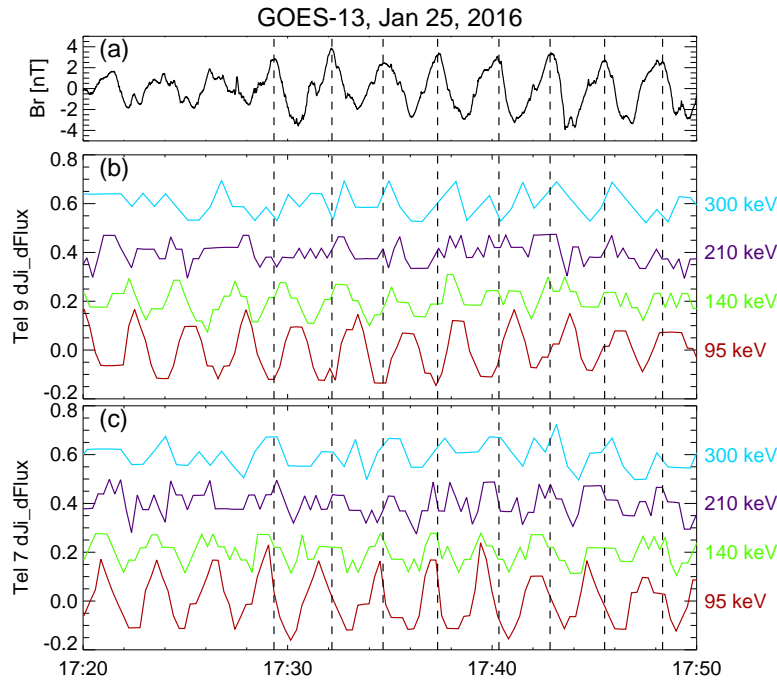


Figure 4.12: Time series of magnetic field and energetic ion residual flux data from GOES 13 between 17:20 and 17:50 UT on Jan 25, 2016: (a) radial magnetic field; (b) southward moving energetic ion residual fluxes at $\sim 140^\circ$ pitch angle from detector telescope 9; (c) northward moving energetic ion residual fluxes at $\sim 2^\circ$ pitch angle from detector telescope 7.

investigations also indicate a connection between the occurrence of these waves with prior substorm activity (followed by sharp AE drops) and the decay of the ring current [Anderson et al., 1990, Oimatsu et al., 2018, Shi et al., 2018b]. For low energy ions (< 10 keV), the convection electric field becomes significant and can cause these particles to drift out of the magnetosphere and form unstable bump-on-tail distribution occurring ~ 0.5 -2 days after particle injections as proposed by Ozeke and Mann [2001]. However, it is difficult to identify the source of these low energy particles which may be associated with prior substorm activity or other magnetospheric processes [Liu et al., 2013, Wright et al., 2001]. The bump-on-tail distribution might last for a few days and cover some longitudinal extent on the dayside. The cold background plasma density during the plasmaspheric refilling would change the

local field line eigenfrequency and thus control the location of ULF wave excitation through the drift-bounce resonance condition [Liu et al., 2013, Min et al., 2017].

4.5 Conclusions

Using multiple spacecraft and high-latitude SuperDARN radars, we have analyzed a long-lasting (2-3 days) second harmonic poloidal ULF wave during the recovery phase of the geomagnetic storm on 24-27 January 2016. These narrowband waves between 5-10 mHz are very localized radially but extended azimuthally (up to 10 hr) in the dayside magnetosphere and ionosphere. The waves are westward propagating high- m (~ -258) mode and thus cannot be detected by ground magnetometers due to ionospheric screening effects. The source of wave excitation is suggested to be bump-on-tail ion distributions at 1-3 keV. These waves could impact magnetospheric particle dynamics through drift-bounce resonance, including modulation and acceleration/deceleration of ring current energetic particles and cold plasmaspheric particles. This study emphasizes the role of conjugate satellite-SuperDARN observations in high- m ULF wave study as well as multi-point SuperDARN high-time resolution data in estimating the wave spatial extent and ionospheric electric fields/flow for Pc4-5 waves in the radiation belts/ring current (i.e., sub-auroral region). The relatively recent mid-latitude SuperDARN radars and high-time resolution radar data (e.g., THEMIS mode) open up several possibilities for ULF wave studies and make it possible to study global waves at higher frequency and lower latitude as shown in this study.

Acknowledgments

Work at Virginia Tech was supported by National Aeronautics and Space Administration (NASA) Headquarters under the NASA Earth and Space Science Fellowship Program - Grant 80NSSC17K0456 P00001, National Science Foundation (NSF) grant AGS-1341918 and ICER-1541007. M. D. Hartinger was supported by NASA grant NNX17AD35G. K. R. Murphy is partially funded by NSF grant 1602403. J. V. Rodriguez was supported by National Center for Environmental Information (NCEI) through NOAA Cooperative Agreement NA17OAR4320101. The authors acknowledge the use of SuperDARN data, which are freely available through the SuperDARN website at Virginia Polytechnic Institute and State University (<http://vt.superdarn.org/>). SuperDARN is a collection of radars funded by national scientific funding agencies of Australia, Canada, China, France, Italy, Japan, Norway, South Africa, the United Kingdom and the United States. SuperDARN Canada radar operations are supported by the Canada Foundation for Innovation, the Province of Saskatchewan, and the Canadian Space Agency. The GOES magnetic field and energetic particle data are publicly available from NOAA National Centers for Environmental Information (formerly the National Geophysical Data Center). We acknowledge NASA contract NAS5-02099 and V. Angelopoulos for use of data from the THEMIS Mission (<http://themis.ssl.berkeley.edu/>). Specifically J. W. Bonnell and F. S. Mozer for use of EFI data; K. H. Glassmeier, U. Auster and W. Baumjohann for the use of FGM data provided under the lead of the Technical University of Braunschweig and with financial support through the German Ministry for Economy and Technology and the German Center for Aviation and Space (DLR) under contract 50 OC 0302; J. McFadden for the use of THEMIS/ESA data; I.R. Mann, D.K. Milling and the rest of the CARISMA team for use of GMAG data (<http://carisma.ca/>). CARISMA is operated by the University of Alberta, funded by the Canadian Space Agency. The SNKQ ground magnetometer data are obtained by the CANMOS network, maintained

and operated by the Geological Survey of Canada. Dst and AE indices are obtained at the World Data Center Kyoto University (<http://wdc.kugi.kyoto-u.ac.jp/dstdir/>).

Table 4.1: Comparisons of Select Long-Lasting Poloidal ULF Wave Case Studies

Case study	Magnetic activity & event duration	Wave mode & frequency	Instrumentation & spatial coverage	m-value	Source mechanism
This study	Recovery phase of the Jan 19-28, 2016 geomagnetic storm 2-3 days	2nd harmonic 5-10 mHz	THEMIS, G-13 G-15, SuperDARN dayside L~5.5-8	~ -258 westward postdusk	Bounce resonance through bump-on-tail unstable proton distributions at 1-3 keV
Takahashi et al. 2018	After a geomagnetic storm during low geomagnetic activity 1 day	2nd harmonic ~10 mHz	Van Allen probes MLT~10-14 L~4.4-5.8	~ -200 westward near noon	Bounce resonance through bump-on-tail unstable proton distributions at 1-10 keV
Min et al. 2017	After a minor geomagnetic storm during quiet time 1 day	2nd harmonic ~7 mHz	Van Allen probes G-15 MLT~17-02 L~6-6.7	~ -100 westward pre- midnight	Drift-bounce resonance through an inward radial gradient of ring current protons
Le et al. 2017	Recovery phase of the 22 June 2015 geomagnetic storm 3 days	2nd harmonic 3-30 mHz	Van Allen probes THEMIS, Cluster G-15, G-13, MMS dayside to premidnight L~4-12	~ -100 westward postdusk	No observational evidence, could be drift-bounce resonance
Korotova et al. 2016	After the main phase of the 1-2 May 2014 geomagnetic storm during quiet time 3 days	2nd harmonic 10-25 mHz	Van Allen probes THEMIS, G-15 dayside L~4-8	Not available	Not completely clear, attribute to bounce resonance
Liu et al. 2013	After a moderate geomagnetic storm 1 day	2nd harmonic 5-15 mHz	THEMIS MLT~12-14 L~3.7-6.8	Not available	Bounce resonance through bump-on-tail unstable proton distributions at ~10 keV
Sarris et al. 2009	Recovery phase of the Nov 24-30, 1997 geomagnetic storm 4-5 days	Narrowband Pc5 5-9 mHz	G-8, G-9, Geotail LANL, ground magnetometer dayside L~6.6	~ 20-55 eastward prenoon	Undetermined, but exclude: external solar wind source, KH waves, ion drift-bounce resonance

Chapter 5

Conclusions and Future Work

The goal of this research has been to gain a better understanding of the occurrence and generation mechanisms of magnetospheric and ionospheric ULF waves, their interactions with particles, and their role in solar wind - magnetosphere - ionosphere coupling. In Chapter 2, we examined the generation of ULF waves in the magnetosphere and their propagation to the ionosphere. A case study of Pi2 pulsations observed near the plasmopause was analyzed through coordinated spacecraft and ground observations. By analyzing the longitudinal polarization pattern of the wave and its azimuthal phase propagation, we confirmed that the pulsations were consistent with a global plasmaspheric virtual resonance excited by a longitudinally localized source near midnight. A logical extension of this work would be to conduct a statistical investigation of similar events to develop a better understanding of the properties of this type of pulsation and the conditions that lead to its excitation in the complicated midlatitude transition region. The effects of these pulsations on energetic particle injections associated with substorm activity [Turner et al., 2015] could be explored as a practical and possibly predictable impact of ULF wave activity.

Chapter 3 presented a statistical study that further investigated the overall occurrence of ionospheric ULF wave signatures using an automated detection algorithm to identify ionospheric signatures of Pc3-5 waves in seven years of high-time resolution SuperDARN data. We investigated the wave spatial occurrence, frequency characteristics, and seasonal effects, and considered their dependencies on solar wind and geomagnetic conditions. The results

suggest an internal source is responsible for Pc4 waves in the high-latitude duskside ionosphere while processes associated with magnetotail dynamics during active geomagnetic times are responsible for Pc3-4/Pi2 events in the midlatitude nightside ionosphere. Similar techniques could be applied to SuperDARN data in other special modes (e.g., RBSP and ULF modes) that feature multiple camping beams operating in high-time resolution. Extension of this work could estimate the wave propagation (i.e., m value) by comparing measurements across the multiple camping beams with high time resolution data from the individual SuperDARN radars. As stated in the Introduction, knowledge of m value and wave propagation are vital for distinguishing possible excitation mechanisms, i.e., internal versus external. Statistically quantifying the azimuthal wave number using SuperDARN data is a promising future direction to gain a better understanding of the ULF wave sources.

In Chapter 4 we investigated the possibility that internal sources can be important as generation mechanisms. Using multiple spacecraft and the high-latitude SuperDARN radars, we analyzed a long-lasting (2-3 days) second harmonic poloidal ULF wave event that occurred during the recovery phase of a geomagnetic storm. These narrowband waves (5-10 mHz) were very localized radially but extended azimuthally across the dayside magnetosphere and ionosphere. They were westward propagating high- m mode and thus could not be detected by ground magnetometers due to ionospheric screening effects. The source of wave excitation was suggested to be bump-on-tail ion distributions at 1-3 keV based on ion phase space density distribution data from one THEMIS probe. Applying sonification to the GOES magnetometer data, [Archer et al. \[2018\]](#) found 21 long-lasting poloidal wave events following geomagnetic storms in 2013, suggesting that such events cannot be considered rare. Collaboration with Dr. Martin Archer to find more GOES-SuperDARN conjunction events is suggested as a way to resolve the properties of these events on global scales and to clarify the source in geomagnetic storm conditions.

In summary, utilizing the SuperDARN high-time resolution data, we investigated ionospheric Pc3-5 ULF wave occurrence statistics, including their spatial and frequency distribution, seasonal, solar wind condition, and geomagnetic activity level dependencies. This study answers the first science question we brought up in Section 1.3, which provides better constraints on where and when ULF waves occur. Through space and ground coordinated observations, we confirmed the generation mechanism of a Pi2 pulsation event and a long-lasting poloidal wave event. Both studies help answer the second science question of the primary driving sources of ionospheric ULF waves. Research in this dissertation also provides some insight into how ULF waves can affect magnetospheric and ionospheric dynamics.

In addition, we provide the following suggestions for future work that could make good use of the ULF wave database presented in Chapter 3:

1. Only a few event studies have quantified the energy dissipation in the ionosphere related to ULF waves. [Greenwald and Walker \[1980\]](#) estimated the total energy deposition in the ionosphere through Joule heating by Pc5 toroidal mode pulsations to be up to 4% of the energy that is deposited during a small substorm. However, [Rae et al. \[2008\]](#) found that the total energy deposition via Joule heating of a global FLR may actually be 30% or more of the energy deposited in the ionosphere during a substorm cycle. Very few studies have statistically quantified the energy budget in the magnetosphere - ionosphere (M-I) system associated with ULF waves. The ULF wave database described in Chapter 3 could be used to statistically quantify energy deposition in the ionosphere via Joule heating associated with ULF waves.
2. We have mainly focused on nightside ULF wave activity in this dissertation; identification and characterization of ULF waves observed on the dayside remains unexplored. Transient ion foreshock phenomena, such as hot flow anomalies and foreshock bubbles, are known to drive field-aligned currents, traveling convection vortices, and ULF waves in the

magnetosphere-ionosphere system. Taking advantage of the ULF wave events in our database observed on the dayside by multiple SuperDARN radars operating simultaneously at different latitudes and local times, it should be possible to monitor the large-scale ionospheric response to foreshock transients and to characterize the ULF wave spatial distribution and propagation.

3. The generation mechanisms of ULF waves observed on the Earth's closed magnetic field lines have been extensively studied and are reasonably well understood. However, ULF waves observed in the polar cap region on open magnetic field lines are poorly understood. Previous investigations have suggested three possible sources that might contribute to the generation of polar ULF pulsations: turbulent processes occurring in the magnetosheath, transient wave activity in the magnetotail lobes, and solar wind direct driven source. The ULF wave events from three PolarDARN radars (i.e., INV, RKN, and CLY) detected in the database described in Chapter 3 could be used to further investigate the nature of polar cap ULF waves and to identify their causes.

The studies described in Chapter 2-4 were published in the *Journal of Geophysical Research: Space Physics* [Shi et al., 2017, 2018a,b] and supported by NSF grants and a NASA Earth and Space Science Fellowship. ULF waves have been recognized to play an important role in magnetospheric plasma energization/loss and energy transfer from the solar wind to Earth's magnetosphere and ionosphere. The improved understanding of ULF wave and particle interactions developed in this work is a step forward in improving future space weather forecasts, which is the NASA Heliophysics main goal, because ULF waves are important for modulating energetic particle precipitation and accelerating radiation belt particles to relativistic energies and hence creating space weather hazards.

Bibliography

- S-I Akasofu. The development of the auroral substorm. *Planetary and Space Science*, 12(4): 273–282, 1964.
- Hannes Alfvén. Existence of electromagnetic-hydrodynamic waves. *Nature*, 150(3805):405, 1942.
- W Allan and FB Knox. A dipole field model for axisymmetric Alfvén waves with finite ionosphere conductivities. *Planetary and Space Science*, 27(1):79–85, 1979.
- W. Allan, F. W. Menk, B. J. Fraser, Y. Li, and S. P. White. Are low-latitude Pi2 pulsations cavity/waveguide modes? *Geophysical Research Letters*, 23(7):765–768, 1996. doi: 10.1029/96GL00661. URL <https://agupubs.onlinelibrary.wiley.com/doi/abs/10.1029/96GL00661>.
- B. J. Anderson, M. J. Engebretson, S. P. Rounds, L. J. Zanetti, and T. A. Potemra. A statistical study of Pc 3–5 pulsations observed by the AMPTE/CCE Magnetic Fields Experiment, 1. Occurrence distributions. *Journal of Geophysical Research: Space Physics*, 95(A7):10495–10523, 1990. doi: 10.1029/JA095iA07p10495. URL <https://agupubs.onlinelibrary.wiley.com/doi/abs/10.1029/JA095iA07p10495>.
- BJ Anderson. An overview of spacecraft observations of 10 s to 600 s period magnetic pulsations in the Earth’s magnetosphere. *Washington DC American Geophysical Union Geophysical Monograph Series*, 81:25–43, 1994.
- Brian J Anderson. Statistical studies of Pc 3-5 pulsations and their relevance for possible

- source mechanisms of ULF waves. In *Annales Geophysicae*, volume 11, pages 128–143, 1993.
- V. Angelopoulos. The THEMIS Mission. *Space Science Reviews*, 141(1):5, Apr 2008. ISSN 1572-9672. doi: 10.1007/s11214-008-9336-1. URL <https://doi.org/10.1007/s11214-008-9336-1>.
- MO Archer, MD Hartinger, R Redmon, V Angelopoulos, BM Walsh, and Eltham Hill School Year 12 Physics Students. First Results From Sonification and Exploratory Citizen Science of Magnetospheric ULF Waves: Long-Lasting Decreasing-Frequency Poloidal Field Line Resonances Following Geomagnetic Storms. *Space Weather*, 16(11):1753–1769, 2018.
- H. U. Auster, K. H. Glassmeier, W. Magnes, O. Aydogar, W. Baumjohann, D. Constantinescu, D. Fischer, K. H. Fornacon, E. Georgescu, P. Harvey, O. Hillenmaier, R. Kroth, M. Ludlam, Y. Narita, R. Nakamura, K. Okrafka, F. Plaschke, I. Richter, H. Schwarzl, B. Stoll, A. Valavanoglou, and M. Wiedemann. The THEMIS Fluxgate Magnetometer. *Space Science Reviews*, 141(1):235–264, Dec 2008. ISSN 1572-9672. doi: 10.1007/s11214-008-9365-9. URL <https://doi.org/10.1007/s11214-008-9365-9>.
- W Ian Axford and Colin O Hines. A unifying theory of high-latitude geophysical phenomena and geomagnetic storms. *Canadian Journal of Physics*, 39(10):1433–1464, 1961.
- HW Babcock. The Topology of the Sun’s Magnetic Field and the 22-YEAR Cycle. *The Astrophysical Journal*, 133:572, 1961.
- LJ Baddeley, TK Yeoman, DM Wright, KJ Trattner, and BJ Kellet. A statistical study of unstable particle populations in the global ring current and their relation to the generation of high m ULF waves. *ANNALES GEOPHYSICAE*, 22(12):4229–4241, 2004. ISSN 0992-7689. doi: {10.5194/angeo-22-4229-2004}.

LJ Baddeley, TK Yeoman, DM Wright, KJ Trattner, and BJ Kellet. On the coupling between unstable magnetospheric particle populations and resonant high m ULF wave signatures in the ionosphere. *ANNALES GEOPHYSICAE*, 23(2):567–577, 2005. ISSN 0992-7689. doi: {10.5194/angeo-23-567-2005}.

Gregory J. Baker, Eric F. Donovan, and Brian J. Jackel. A comprehensive survey of auroral latitude Pc5 pulsation characteristics. *Journal of Geophysical Research: Space Physics*, 108(A10), 2003. doi: 10.1029/2002JA009801. URL <https://agupubs.onlinelibrary.wiley.com/doi/abs/10.1029/2002JA009801>.

J. B. H. Baker, R. A. Greenwald, J. M. Ruohoniemi, K. Oksavik, J. W. Gjerloev, L. J. Paxton, and M. R. Hairston. Observations of ionospheric convection from the Wallops SuperDARN radar at middle latitudes. *Journal of Geophysical Research: Space Physics*, 112(A1), 2007. doi: 10.1029/2006JA011982. URL <https://agupubs.onlinelibrary.wiley.com/doi/abs/10.1029/2006JA011982>.

K. B. Baker and S. Wing. A new magnetic coordinate system for conjugate studies at high latitudes. *Journal of Geophysical Research: Space Physics*, 94(A7):9139–9143, 1989. doi: 10.1029/JA094iA07p09139. URL <https://agupubs.onlinelibrary.wiley.com/doi/abs/10.1029/JA094iA07p09139>.

Wolfgang Baumjohann and Karl-Heinz Glaßmeier. The transient response mechanism and Pi2 pulsations at substorm onset—Review and outlook. *Planetary and Space Science*, 32(11):1361 – 1370, 1984. ISSN 0032-0633. doi: [https://doi.org/10.1016/0032-0633\(84\)90079-5](https://doi.org/10.1016/0032-0633(84)90079-5). URL <http://www.sciencedirect.com/science/article/pii/0032063384900795>.

G. T. Blanchard, S. Sundeen, and K. B. Baker. Probabilistic identification of high-frequency radar backscatter from the ground and ionosphere based on spectral char-

- acteristics. *Radio Science*, 44(5), 2009. doi: 10.1029/2009RS004141. URL <https://agupubs.onlinelibrary.wiley.com/doi/abs/10.1029/2009RS004141>.
- Emma C. Bland, Andrew J. McDonald, Frederick W. Menk, and John C. Devlin. Multipoint visualization of ULF oscillations using the Super Dual Auroral Radar Network. *Geophysical Research Letters*, 41(18):6314–6320, 2014. doi: 10.1002/2014GL061371. URL <https://agupubs.onlinelibrary.wiley.com/doi/abs/10.1002/2014GL061371>.
- J. W. Bonnell, F. S. Mozer, G. T. Delory, A. J. Hull, R. E. Ergun, C. M. Cully, V. Angelopoulos, and P. R. Harvey. The Electric Field Instrument (EFI) for THEMIS. *Space Science Reviews*, 141(1):303–341, Dec 2008. ISSN 1572-9672. doi: 10.1007/s11214-008-9469-2. URL <https://doi.org/10.1007/s11214-008-9469-2>.
- William B. Cade III and Christina Chan-Park. The Origin of “Space Weather”. *Space Weather*, 13(2):99–103, 2015. doi: 10.1002/2014SW001141. URL <https://agupubs.onlinelibrary.wiley.com/doi/abs/10.1002/2014SW001141>.
- Liu Chen and Akira Hasegawa. Kinetic theory of geomagnetic pulsations: 1. Internal excitations by energetic particles. *Journal of Geophysical Research: Space Physics*, 96(A2):1503–1512, 1991. doi: 10.1029/90JA02346. URL <https://agupubs.onlinelibrary.wiley.com/doi/abs/10.1029/90JA02346>.
- P. J. Chi and G. Le. Observations of magnetospheric high-m poloidal waves by ST-5 satellites in low Earth orbit during geomagnetically quiet times. *Journal of Geophysical Research: Space Physics*, 120(6):4776–4783, 2015. doi: 10.1002/2015JA021145. URL <https://agupubs.onlinelibrary.wiley.com/doi/abs/10.1002/2015JA021145>.
- G. Chisham. Giant pulsations: An explanation for their rarity and occurrence during geomagnetically quiet times. *Journal of Geophysical Research: Space Physics*, 101(A11):

- 24755–24763, 1996. doi: 10.1029/96JA02540. URL <https://agupubs.onlinelibrary.wiley.com/doi/abs/10.1029/96JA02540>.
- G. Chisham, M. Lester, S. E. Milan, M. P. Freeman, W. A. Bristow, A. Grocott, K. A. McWilliams, J. M. Ruohoniemi, T. K. Yeoman, P. L. Dyson, R. A. Greenwald, T. Kikuchi, M. Pinnock, J. P. S. Rash, N. Sato, G. J. Sofko, J.-P. Villain, and A. D. M. Walker. A decade of the Super Dual Auroral Radar Network (SuperDARN): scientific achievements, new techniques and future directions. *Surveys in Geophysics*, 28(1):33–109, Jan 2007. ISSN 1573-0956. doi: 10.1007/s10712-007-9017-8. URL <https://doi.org/10.1007/s10712-007-9017-8>.
- S. G. Claudepierre, S. R. Elkington, and M. Wiltberger. Solar wind driving of magnetospheric ULF waves: Pulsations driven by velocity shear at the magnetopause. *Journal of Geophysical Research: Space Physics*, 113(A5), 2008. doi: 10.1029/2007JA012890. URL <https://agupubs.onlinelibrary.wiley.com/doi/abs/10.1029/2007JA012890>.
- S. G. Claudepierre, I. R. Mann, K. Takahashi, J. F. Fennell, M. K. Hudson, J. B. Blake, J. L. Roeder, J. H. Clemmons, H. E. Spence, G. D. Reeves, D. N. Baker, H. O. Funsten, R. H. W. Friedel, M. G. Henderson, C. A. Kletzing, W. S. Kurth, R. J. MacDowall, C. W. Smith, and J. R. Wygant. Van Allen Probes observation of localized drift resonance between poloidal mode ultra-low frequency waves and 60 keV electrons. *Geophysical Research Letters*, 40(17):4491–4497, 2013. doi: 10.1002/grl.50901. URL <https://agupubs.onlinelibrary.wiley.com/doi/abs/10.1002/grl.50901>.
- E. D. P. Cousins and S. G. Shepherd. Statistical characteristics of small-scale spatial and temporal electric field variability in the high-latitude ionosphere. *Journal of Geophysical Research: Space Physics*, 117(A3), 2012. doi: 10.1029/2011JA017383. URL <https://agupubs.onlinelibrary.wiley.com/doi/abs/10.1029/2011JA017383>.

- G Crowley, N Wade, JA Waldock, TR Robinson, and TB Jones. High time-resolution observations of periodic frictional heating associated with a Pc5 micropulsation. *Nature*, 316(6028):528, 1985.
- Ioannis A Daglis, Richard M Thorne, Wolfgang Baumjohann, and Stefano Orsini. The terrestrial ring current: Origin, formation, and decay. *Reviews of Geophysics*, 37(4):407–438, 1999.
- Lei Dai, Kazue Takahashi, John R. Wygant, Liu Chen, John Bonnell, Cynthia A. Cattell, Scott Thaller, Craig Kletzing, Charles W. Smith, Robert J. MacDowall, Daniel N. Baker, J. Bernard Blake, Joseph Fennell, Seth Claudepierre, Herbert O. Funsten, Geoffrey D. Reeves, and Harlan E. Spence. Excitation of poloidal standing Alfvén waves through drift resonance wave-particle interaction. *Geophysical Research Letters*, 40(16):4127–4132, 2013. doi: 10.1002/grl.50800. URL <https://agupubs.onlinelibrary.wiley.com/doi/abs/10.1002/grl.50800>.
- Lei Dai, Kazue Takahashi, Robert Lysak, Chi Wang, John R. Wygant, Craig Kletzing, John Bonnell, Cynthia A. Cattell, Charles W. Smith, Robert J. MacDowall, Scott Thaller, Aaron Breneman, Xiangwei Tang, Xin Tao, and Lunjin Chen. Storm time occurrence and spatial distribution of Pc4 poloidal ULF waves in the inner magnetosphere: A Van Allen Probes statistical study. *Journal of Geophysical Research: Space Physics*, 120(6):4748–4762, 2015. doi: 10.1002/2015JA021134. URL <https://agupubs.onlinelibrary.wiley.com/doi/abs/10.1002/2015JA021134>.
- T. Neil Davis and Masahisa Sugiura. Auroral electrojet activity index AE and its universal time variations. *Journal of Geophysical Research (1896-1977)*, 71(3):785–801, 1966. doi: 10.1029/JZ071i003p00785. URL <https://agupubs.onlinelibrary.wiley.com/doi/abs/10.1029/JZ071i003p00785>.

- AJ Dessler. Upper atmosphere density variations due to hydromagnetic heating. *Nature*, 184(4682):261, 1959.
- J. W. Dungey. Electrodynamics of the Outer Atmosphere. In *Physics of the Ionosphere*, page 229, 1955.
- James W Dungey. Interplanetary magnetic field and the auroral zones. *Physical Review Letters*, 6(2):47, 1961.
- Scot R. Elkington, Mary K. Hudson, and Anthony A. Chan. Acceleration of relativistic electrons via drift-resonant interaction with toroidal-mode Pc-5 ULF oscillations. *Geophysical Research Letters*, 26(21):3273–3276, 1999. doi: 10.1029/1999GL003659. URL <https://agupubs.onlinelibrary.wiley.com/doi/abs/10.1029/1999GL003659>.
- M. J. Engebretson, D. L. Murr, K. N. Erickson, R. J. Strangeway, D. M. Klumpar, S. A. Fuselier, L. J. Zanetti, and T. A. Potemra. The spatial extent of radial magnetic pulsation events observed in the dayside near synchronous orbit. *Journal of Geophysical Research: Space Physics*, 97(A9):13741–13758, 1992. doi: 10.1029/92JA00992. URL <https://agupubs.onlinelibrary.wiley.com/doi/abs/10.1029/92JA00992>.
- F. R. Fenrich, J. C. Samson, G. Sofko, and R. A. Greenwald. ULF high- and low-m field line resonances observed with the Super Dual Auroral Radar Network. *Journal of Geophysical Research: Space Physics*, 100(A11):21535–21547, 1995. doi: 10.1029/95JA02024. URL <https://agupubs.onlinelibrary.wiley.com/doi/abs/10.1029/95JA02024>.
- B. J. Fraser, J. L. Horwitz, J. A. Slavin, Z. C. Dent, and I. R. Mann. Heavy ion mass loading of the geomagnetic field near the plasmopause and ULF wave implications. *Geophysical Research Letters*, 32(4), 2005. doi: 10.1029/2004GL021315. URL <https://agupubs.onlinelibrary.wiley.com/doi/abs/10.1029/2004GL021315>.

- N. A. Frissell, J. B. H. Baker, J. M. Ruohoniemi, L. B. N. Clausen, Z. C. Kale, I. J. Rae, L. Kepko, K. Oksavik, R. A. Greenwald, and M. L. West. First radar observations in the vicinity of the plasmopause of pulsed ionospheric flows generated by bursty bulk flows. *Geophysical Research Letters*, 38(1), 2011. doi: 10.1029/2010GL045857. URL <https://agupubs.onlinelibrary.wiley.com/doi/abs/10.1029/2010GL045857>.
- H. Fukunishi. Polarization changes of geomagnetic Pi2 pulsations associated with the plasmopause. *Journal of Geophysical Research*, 80(1):98–110, 1975. doi: 10.1029/JA080i001p00098. URL <https://agupubs.onlinelibrary.wiley.com/doi/abs/10.1029/JA080i001p00098>.
- C. Gelpi, H. J. Singer, and W. J. Hughes. A comparison of magnetic signatures and DMSP auroral images at substorm onset: Three case studies. *Journal of Geophysical Research: Space Physics*, 92(A3):2447–2460, 1987. doi: 10.1029/JA092iA03p02447. URL <https://agupubs.onlinelibrary.wiley.com/doi/abs/10.1029/JA092iA03p02447>.
- E. Ghamry, K.-H. Kim, H.-J. Kwon, D.-H. Lee, J.-S. Park, J. Choi, K. Hyun, W. S. Kurth, C. Kletzing, J. R. Wygant, and J. Huang. Simultaneous Pi2 observations by the Van Allen Probes inside and outside the plasmasphere. *Journal of Geophysical Research: Space Physics*, 120(6):4567–4575, 2015. doi: 10.1002/2015JA021095. URL <https://agupubs.onlinelibrary.wiley.com/doi/abs/10.1002/2015JA021095>.
- J. W. Gjerloev, R. A. Greenwald, C. L. Waters, K. Takahashi, D. Sibeck, K. Oksavik, R. Barnes, J. Baker, and J. M. Ruohoniemi. Observations of Pi2 pulsations by the Wallops HF radar in association with substorm expansion. *Geophysical Research Letters*, 34(20), 2007. doi: 10.1029/2007GL030492. URL <https://agupubs.onlinelibrary.wiley.com/doi/abs/10.1029/2007GL030492>.

- RA Greenwald and ADM Walker. Energetics of long period resonant hydromagnetic waves. *Geophysical Research Letters*, 7(10):745–748, 1980.
- D. A. Hamlin, R. Karplus, R. C. Vik, and K. M. Watson. Mirror and azimuthal drift frequencies for geomagnetically trapped particles. *Journal of Geophysical Research*, 66(1):1–4, 1961. doi: 10.1029/JZ066i001p00001. URL <https://agupubs.onlinelibrary.wiley.com/doi/abs/10.1029/JZ066i001p00001>.
- MD Hartinger, DL Turner, F Plaschke, V Angelopoulos, and H Singer. The role of transient ion foreshock phenomena in driving Pc5 ULF wave activity. *Journal of Geophysical Research: Space Physics*, 118(1):299–312, 2013.
- Akira Hasegawa. Drift Mirror Instability in the Magnetosphere. *The Physics of Fluids*, 12(12):2642–2650, 1969. doi: 10.1063/1.1692407. URL <https://aip.scitation.org/doi/abs/10.1063/1.1692407>.
- MK Hudson, RE Denton, MR Lessard, EG Miftakhova, and RR Anderson. A study of Pc-5 ULF oscillations. *ANNALES GEOPHYSICAE*, 22(1):289–302, 2004. ISSN 0992-7689. doi: {10.5194/angeo-22-289-2004}.
- W. J. Hughes and R. J. L. Grard. A second harmonic geomagnetic field line resonance at the inner edge of the plasma sheet: GEOS 1, ISEE 1, and ISEE 2 observations. *Journal of Geophysical Research: Space Physics*, 89(A5):2755–2764, 1984. doi: 10.1029/JA089iA05p02755. URL <https://agupubs.onlinelibrary.wiley.com/doi/abs/10.1029/JA089iA05p02755>.
- W. J. Hughes and D. J. Southwood. The screening of micropulsation signals by the atmosphere and ionosphere. *Journal of Geophysical Research*, 81(19):3234–3240, 1976. doi: 10.1029/JA081i019p03234. URL <https://agupubs.onlinelibrary.wiley.com/doi/abs/10.1029/JA081i019p03234>.

- W Jeffrey Hughes. Magnetospheric ULF waves: A tutorial with a historical perspective. *Solar Wind Sources of Magnetospheric Ultra-Low-Frequency Waves*, 81:1–11, 1994.
- Toshihiko Iyemori. Storm-time magnetospheric currents inferred from mid-latitude geomagnetic field variations. *Journal of geomagnetism and geoelectricity*, 42(11):1249–1265, 1990.
- J. A. Jacobs, Y. Kato, S. Matsushita, and V. A. Troitskaya. Classification of geomagnetic micropulsations. *Journal of Geophysical Research*, 69(1):180–181, 1964. doi: 10.1029/JZ069i001p00180. URL <https://agupubs.onlinelibrary.wiley.com/doi/abs/10.1029/JZ069i001p00180>.
- M. K. James, T. K. Yeoman, P. N. Mager, and D. Yu. Klimushkin. The spatio-temporal characteristics of ULF waves driven by substorm injected particles. *Journal of Geophysical Research: Space Physics*, 118(4):1737–1749, 2013. doi: 10.1002/jgra.50131. URL <https://agupubs.onlinelibrary.wiley.com/doi/abs/10.1002/jgra.50131>.
- Secil Karatay, Feza Arikan, and Orhan Arikan. Investigation of total electron content variability due to seismic and geomagnetic disturbances in the ionosphere. *Radio Science*, 45(05):1–12, 2010.
- A. Keiling, V. Angelopoulos, D. Larson, R. Lin, J. McFadden, C. Carlson, J. W. Bonnell, F. S. Mozer, K.-H. Glassmeier, H. U. Auster, W. Magnes, S. Mende, H. Frey, A. Roux, O. LeContel, S. Frey, T. Phan, E. Donovan, C. T. Russell, I. Mann, W. Liu, X. Li, M. Fillingim, G. Parks, K. Shiokawa, and J. Raeder. Correlation of substorm injections, auroral modulations, and ground Pi2. *Geophysical Research Letters*, 35(17), 2008. doi: 10.1029/2008GL033969. URL <https://agupubs.onlinelibrary.wiley.com/doi/abs/10.1029/2008GL033969>.
- Andreas Keiling. Pi2 pulsations driven by ballooning instability. *Journal of Geophysical*

- Research: Space Physics*, 117(A3), 2012. doi: 10.1029/2011JA017223. URL <https://agupubs.onlinelibrary.wiley.com/doi/abs/10.1029/2011JA017223>.
- Andreas Keiling and Kazue Takahashi. Review of Pi2 Models. *Space Science Reviews*, 161(1):63–148, Nov 2011. ISSN 1572-9672. doi: 10.1007/s11214-011-9818-4. URL <https://doi.org/10.1007/s11214-011-9818-4>.
- Michael C Kelley. *The Earth's ionosphere: plasma physics and electrodynamics*, volume 96. Academic press, 2009.
- L. Kepko and H. E. Spence. Observations of discrete, global magnetospheric oscillations directly driven by solar wind density variations. *Journal of Geophysical Research: Space Physics*, 108(A6), 2003. doi: 10.1029/2002JA009676. URL <https://agupubs.onlinelibrary.wiley.com/doi/abs/10.1029/2002JA009676>.
- Larry Kepko and Margaret Kivelson. Generation of Pi2 pulsations by bursty bulk flows. *Journal of Geophysical Research: Space Physics*, 104(A11):25021–25034, 1999. doi: 10.1029/1999JA900361. URL <https://agupubs.onlinelibrary.wiley.com/doi/abs/10.1029/1999JA900361>.
- K.-H. Kim, D.-H. Lee, K. Takahashi, C. T. Russell, Y.-J. Moon, and K. Yumoto. Pi2 pulsations observed from the Polar satellite outside the plasmopause. *Geophysical Research Letters*, 32(18), 2005. doi: 10.1029/2005GL023872. URL <https://agupubs.onlinelibrary.wiley.com/doi/abs/10.1029/2005GL023872>.
- J. H. King and N. E. Papitashvili. Solar wind spatial scales in and comparisons of hourly Wind and ACE plasma and magnetic field data. *Journal of Geophysical Research: Space Physics*, 110(A2), 2005. doi: 10.1029/2004JA010649. URL <https://agupubs.onlinelibrary.wiley.com/doi/abs/10.1029/2004JA010649>.

- M. G. Kivelson and C. T. Russell. *Introduction to space physics*. Cambridge University Press, 1995.
- Margaret G. Kivelson and David J. Southwood. Resonant ULF waves: A new interpretation. *Geophysical Research Letters*, 12(1):49–52, 1985. doi: 10.1029/GL012i001p00049. URL <https://agupubs.onlinelibrary.wiley.com/doi/abs/10.1029/GL012i001p00049>.
- Galina Korotova, David Sibeck, Mark Engebretson, John Wygant, Scott Thaller, Harlan Spence, Craig Kletzing, Vassilis Angelopoulos, and Robert Redmon. Multipoint spacecraft observations of long-lasting poloidal Pc4 pulsations in the dayside magnetosphere on 1-2 May 2014. *ANNALES GEOPHYSICAE*, 34(11):985–998, NOV 14 2016.
- Hannu E. J. Koskinen and Tuija I. Pulkkinen. Midnight velocity shear zone and the concept of Harang discontinuity. *Journal of Geophysical Research: Space Physics*, 100(A6):9539–9547, 1995. doi: 10.1029/95JA00228. URL <https://agupubs.onlinelibrary.wiley.com/doi/abs/10.1029/95JA00228>.
- O. V. Kozyreva, V. A. Pilipenko, M. J. Engebretson, D. Y. Klimushkin, and P. N. Mager. Correspondence between the ULF wave power distribution and auroral oval. *Solar-Terrestrial Physics*, 2:46–65, 2016. doi: 10.12737/20999. URL <https://doi.org/10.12737/20999>.
- H.-J. Kwon, K.-H. Kim, C.-W. Jun, K. Takahashi, D.-H. Lee, E. Lee, H. Jin, J. Seon, Y.-D. Park, and J. Hwang. Low-latitude Pi2 pulsations during intervals of quiet geomagnetic conditions ($K_p \leq 1$). *Journal of Geophysical Research: Space Physics*, 118(10):6145–6153, 2013. doi: 10.1002/jgra.50582. URL <https://agupubs.onlinelibrary.wiley.com/doi/abs/10.1002/jgra.50582>.
- G. Le, P. J. Chi, R. J. Strangeway, C. T. Russell, J. A. Slavin, K. Takahashi, H. J. Singer, B. J. Anderson, K. Bromund, D. Fischer, E. L. Kepko, W. Magnes, R. Nakamura,

- F. Plaschke, and R. B. Torbert. Global observations of magnetospheric high-m poloidal waves during the 22 June 2015 magnetic storm. *Geophysical Research Letters*, 44(8): 3456–3464, 2017. doi: 10.1002/2017GL073048. URL <https://agupubs.onlinelibrary.wiley.com/doi/abs/10.1002/2017GL073048>.
- Dong-Hun Lee and Kihong Kim. Compressional MHD waves in the magnetosphere: A new approach. *Journal of Geophysical Research: Space Physics*, 104(A6):12379–12385, 1999. doi: 10.1029/1999JA900053. URL <https://agupubs.onlinelibrary.wiley.com/doi/abs/10.1029/1999JA900053>.
- Dong-Hun Lee and Robert L. Lysak. MHD waves in a three-dimensional dipolar magnetic field: A search for Pi2 pulsations. *Journal of Geophysical Research: Space Physics*, 104(A12):28691–28699, 1999. doi: 10.1029/1999JA900377. URL <https://agupubs.onlinelibrary.wiley.com/doi/abs/10.1029/1999JA900377>.
- Dong-Hun Lee and Kazue Takahashi. *MHD Eigenmodes in the Inner Magnetosphere*, pages 73–89. American Geophysical Union (AGU), 2013. ISBN 9781118666319. doi: 10.1029/169GM07. URL <https://agupubs.onlinelibrary.wiley.com/doi/abs/10.1029/169GM07>.
- D.-H. Lee and R. L. Lysak. Magnetospheric ULF wave coupling in the dipole model: The impulsive excitation. *Journal of Geophysical Research: Space Physics*, 94(A12):17097–17103, 1989. doi: 10.1029/JA094iA12p17097. URL <https://agupubs.onlinelibrary.wiley.com/doi/abs/10.1029/JA094iA12p17097>.
- Joseph F Lemaire and Konstantin I Gringauz. *The Earth's plasmasphere*. Cambridge University Press, 2005.
- Mark Lester, W. Jeffrey Hughes, and Howard J. Singer. Longitudinal structure in Pi 2 pulsations and the substorm current wedge. *Journal of Geophysical Research: Space Physics*,

- 89(A7):5489–5494, 1984. doi: 10.1029/JA089iA07p05489. URL <https://agupubs.onlinelibrary.wiley.com/doi/abs/10.1029/JA089iA07p05489>.
- Y. Li, B. J. Fraser, F. W. Menk, D. J. Webster, and K. Yumoto. Properties and sources of low and very low latitude Pi2 pulsations. *Journal of Geophysical Research: Space Physics*, 103(A2):2343–2358, 1998. doi: 10.1029/97JA02921. URL <https://agupubs.onlinelibrary.wiley.com/doi/abs/10.1029/97JA02921>.
- Dong Lin, Chi Wang, Wenya Li, Binbin Tang, Xiaocheng Guo, and Zhong Peng. Properties of Kelvin-Helmholtz waves at the magnetopause under northward interplanetary magnetic field: Statistical study. *Journal of Geophysical Research: Space Physics*, 119(9):7485–7494, 2014. doi: 10.1002/2014JA020379. URL <https://agupubs.onlinelibrary.wiley.com/doi/abs/10.1002/2014JA020379>.
- K. Liou, C.-I. Meng, P. T. Newell, K. Takahashi, S.-I. Ohtani, A. T. Y. Lui, M. Brittnacher, and G. Parks. Evaluation of low-latitude Pi2 pulsations as indicators of substorm onset using Polar ultraviolet imagery. *Journal of Geophysical Research: Space Physics*, 105(A2): 2495–2505, 2000. doi: 10.1029/1999JA900416. URL <https://agupubs.onlinelibrary.wiley.com/doi/abs/10.1029/1999JA900416>.
- W. Liu, J. B. Cao, X. Li, T. E. Sarris, Q.-G. Zong, M. Hartinger, K. Takahashi, H. Zhang, Q. Q. Shi, and V. Angelopoulos. Poloidal ULF wave observed in the plasmasphere boundary layer. *Journal of Geophysical Research: Space Physics*, 118(7):4298–4307, 2013. doi: 10.1002/jgra.50427. URL <https://agupubs.onlinelibrary.wiley.com/doi/abs/10.1002/jgra.50427>.
- Nicholas R Lomb. Least-squares frequency analysis of unequally spaced data. *Astrophysics and Space Science*, 39(2):447–462, 1976. ISSN 0004-640X. doi: {10.1007/BF00648343}.

- Anthony TY Lui. Tutorial on geomagnetic storms and substorms. *IEEE Transactions on plasma science*, 28(6):1854–1866, 2000.
- H. Luo, G. X. Chen, A. M. Du, V. Angelopoulos, W. Y. Xu, X. D. Zhao, and Y. Wang. THEMIS multipoint observations of Pi2 pulsations inside and outside the plasmasphere. *Journal of Geophysical Research: Space Physics*, 116(A12), 2011. doi: 10.1029/2011JA016746. URL <https://agupubs.onlinelibrary.wiley.com/doi/abs/10.1029/2011JA016746>.
- R. L. Lysak, Y. Song, M. D. Sciffer, and C. L. Waters. Propagation of Pi2 pulsations in a dipole model of the magnetosphere. *Journal of Geophysical Research: Space Physics*, 120(1):355–367, 2015. doi: 10.1002/2014JA020625. URL <https://agupubs.onlinelibrary.wiley.com/doi/abs/10.1002/2014JA020625>.
- I. R. Mann, D. K. Milling, I. J. Rae, L. G. Ozeke, A. Kale, Z. C. Kale, K. R. Murphy, A. Parent, M. Usanova, D. M. Pahud, E.-A. Lee, V. Amalraj, D. D. Wallis, V. Angelopoulos, K.-H. Glassmeier, C. T. Russell, H.-U. Auster, and H. J. Singer. The Upgraded CARISMA Magnetometer Array in the THEMIS Era. *Space Science Reviews*, 141(1):413–451, Dec 2008. ISSN 1572-9672. doi: 10.1007/s11214-008-9457-6. URL <https://doi.org/10.1007/s11214-008-9457-6>.
- R. A. Mathie and I. R. Mann. A correlation between extended intervals of ULF wave power and storm-time geosynchronous relativistic electron flux enhancements. *Geophysical Research Letters*, 27(20):3261–3264, 2000. doi: 10.1029/2000GL003822. URL <https://agupubs.onlinelibrary.wiley.com/doi/abs/10.1029/2000GL003822>.
- N. C. Maynard and A. J. Chen. Isolated cold plasma regions: Observations and their relation to possible production mechanisms. *Journal of Geophysical Research*, 80(7):1009–1013,

1975. doi: 10.1029/JA080i007p01009. URL <https://agupubs.onlinelibrary.wiley.com/doi/abs/10.1029/JA080i007p01009>.
- J. P. McFadden, C. W. Carlson, D. Larson, M. Ludlam, R. Abiad, B. Elliott, P. Turin, M. Marckwordt, and V. Angelopoulos. The THEMIS ESA Plasma Instrument and In-flight Calibration. *SPACE SCIENCE REVIEWS*, 141(1-4):277–302, DEC 2008. ISSN 0038-6308. doi: {10.1007/s11214-008-9440-2}.
- Robert L McPherron. Magnetic pulsations: their sources and relation to solar wind and geomagnetic activity. *Surveys in Geophysics*, 26(5):545–592, 2005.
- FW Menk, D Orr, MA Clilverd, AJ Smith, CL Waters, DK Milling, and BJ Fraser. Monitoring spatial and temporal variations in the dayside plasmasphere using geomagnetic field line resonances. *Journal of Geophysical Research: Space Physics*, 104(A9):19955–19969, 1999.
- Kyungguk Min, Kazue Takahashi, Aleksandr Y. Ukhorskiy, Jerry W. Manweiler, Harlan E. Spence, J. Singer, Howard, Seth G. Claudepierre, Brian A. Larsen, A. Rualdo Soto-Chavez, and Ross J. Cohen. Second harmonic poloidal waves observed by Van Allen Probes in the dusk-midnight sector. *Journal of Geophysical Research: Space Physics*, 122(3):3013–3039, 2017. doi: 10.1002/2016JA023770. URL <https://agupubs.onlinelibrary.wiley.com/doi/abs/10.1002/2016JA023770>.
- Akira Miura. Kelvin-Helmholtz instability at the magnetospheric boundary: Dependence on the magnetosheath sonic Mach number. *Journal of Geophysical Research: Space Physics*, 97(A7):10655–10675, 1992. doi: 10.1029/92JA00791. URL <https://agupubs.onlinelibrary.wiley.com/doi/abs/10.1029/92JA00791>.
- Tetsuo Motoba, Kazue Takahashi, Juan V. Rodriguez, and Christopher T. Russell. Giant pulsations on the afternoonside: Geostationary satellite and ground observations. *Jour-*

- nal of Geophysical Research: Space Physics*, 120(10):8350–8367, 2015. doi: 10.1002/2015JA021592. URL <https://agupubs.onlinelibrary.wiley.com/doi/abs/10.1002/2015JA021592>.
- Kyle R. Murphy, Ian R. Mann, and Louis G. Ozeke. A ULF wave driver of ring current energization. *Geophysical Research Letters*, 41(19):6595–6602, 2014. doi: 10.1002/2014GL061253. URL <https://agupubs.onlinelibrary.wiley.com/doi/abs/10.1002/2014GL061253>.
- Takesi Nagata, S Kokubun, and T Iijima. Geomagnetically conjugate relationships of giant pulsations at Syowa Base, Antarctica, and Reykjavik, Iceland. *Journal of Geophysical Research*, 68(15):4621–4625, 1963.
- Nozomu Nishitani, John Michael Ruohoniemi, Mark Lester, J Baker, Alexandre Vasilyevich Koustov, S Shepherd, Gareth Chisham, T Hori, E Thomas, RA Makarevich, et al. Review of the Accomplishments of Mid-latitude Super Dual Auroral Radar Network (SuperDARN) HF Radars. *Progress in Earth and Planetary Science*, 2019.
- L. Norouzi-Sedeh, C. L. Waters, and F. W. Menk. Survey of ULF wave signatures seen in the Tasman International Geospace Environment Radars data. *Journal of Geophysical Research: Space Physics*, 120(2):949–963, 2015. doi: 10.1002/2014JA020652. URL <https://agupubs.onlinelibrary.wiley.com/doi/abs/10.1002/2014JA020652>.
- M. Nosé, K. Liou, and P. R. Sutcliffe. Longitudinal dependence of characteristics of low-latitude Pi2 pulsations observed at Kakioka and Hermanus. *Earth, Planets and Space*, 58(6):775–783, Jun 2006. ISSN 1880-5981. doi: 10.1186/BF03351981. URL <https://doi.org/10.1186/BF03351981>.
- S. Oimatsu, M. Nosé, K. Takahashi, K. Yamamoto, K. Keika, C. A. Kletzing, C. W. Smith, R. J. MacDowall, and D. G. Mitchell. Van Allen Probes Observations of Drift-Bounce

- Resonance and Energy Transfer Between Energetic Ring Current Protons and Poloidal Pc4 Wave. *Journal of Geophysical Research: Space Physics*, 123(5):3421–3435, 2018. doi: 10.1029/2017JA025087. URL <https://agupubs.onlinelibrary.wiley.com/doi/abs/10.1029/2017JA025087>.
- L. G. Ozeke and I. R. Mann. Modeling the properties of high-m Alfvén waves driven by the drift-bounce resonance mechanism. *Journal of Geophysical Research: Space Physics*, 106(A8):15583–15597, 2001. doi: 10.1029/2000JA000393. URL <https://agupubs.onlinelibrary.wiley.com/doi/abs/10.1029/2000JA000393>.
- Eugene N Parker. Dynamics of the interplanetary gas and magnetic fields. *The Astrophysical Journal*, 128:664, 1958.
- VL Patel. Low frequency hydromagnetic waves in the magnetosphere: Explorer XII. *Planetary and Space Science*, 13(6):485–506, 1965.
- V Pilipenko, V Belakhovsky, A Kozlovsky, E Fedorov, and K Kauristie. ULF wave modulation of the ionospheric parameters: Radar and magnetometer observations. *Journal of Atmospheric and Solar-Terrestrial Physics*, 108:68–76, 2014a.
- V Pilipenko, V Belakhovsky, D Murr, E Fedorov, and M Engebretson. Modulation of total electron content by ULF Pc5 waves. *Journal of Geophysical Research: Space Physics*, 119(6):4358–4369, 2014b.
- V. Pilipenko, V. Belakhovsky, A. Kozlovsky, E. Fedorov, and K. Kauristie. Determination of the wave mode contribution into the ULF pulsations from combined radar and magnetometer data: Method of apparent impedance. *JOURNAL OF ATMOSPHERIC AND SOLAR-TERRESTRIAL PHYSICS*, 77:85–95, MAR 2012. ISSN 1364-6826. doi: {10.1016/j.jastp.2011.11.013}.

- P. V. Ponomarenko and C. L. Waters. Transition of Pi2 ULF wave polarization structure from the ionosphere to the ground. *Geophysical Research Letters*, 40(8):1474–1478, 2013. doi: 10.1002/grl.50271. URL <https://agupubs.onlinelibrary.wiley.com/doi/abs/10.1002/grl.50271>.
- Pavlo V. Ponomarenko, Frederick W. Menk, and Colin L. Waters. Visualization of ULF waves in SuperDARN data. *Geophysical Research Letters*, 30(18), 2003. doi: 10.1029/2003GL017757. URL <https://agupubs.onlinelibrary.wiley.com/doi/abs/10.1029/2003GL017757>.
- IJ Rae, CEJ Watt, FR Fenrich, IR Mann, LG Ozeke, and A Kale. Energy deposition in the ionosphere through a global field line resonance. *Annales Geophysicae*, 25(12):2529–2539, 2008.
- M Regi. ULF power fluctuations in the solar-wind parameters and their relationship with the relativistic electron flux at the geosynchronous orbit. *IL NUOVO CIMENTO*, 100(285):39, 2016.
- J. V. Rodriguez. GOES 13-15 MAGE/PD pitch angles algorithm theoretical basis document, version 1.0. *Boulder, CO: NOAA National Geophysical Data Center*, 2014. URL <http://www.ngdc.noaa.gov/stp/satellite/goes/documentation.html>.
- G. Rostoker, S.-I. Akasofu, J. Foster, R.A. Greenwald, Y. Kamide, K. Kawasaki, A.T.Y. Lui, R.L. McPherron, and C.T. Russell. Magnetospheric substorms—definition and signatures. *Journal of Geophysical Research: Space Physics*, 85(A4):1663–1668, 1980. doi: 10.1029/JA085iA04p01663. URL <https://agupubs.onlinelibrary.wiley.com/doi/abs/10.1029/JA085iA04p01663>.
- J. M. Ruohoniemi, R. A. Greenwald, K. B. Baker, and J. C. Samson. HF radar observations of Pc 5 field line resonances in the midnight/early morning MLT sector. *Journal of*

- Geophysical Research: Space Physics*, 96(A9):15697–15710, 1991. doi: 10.1029/91JA00795. URL <https://agupubs.onlinelibrary.wiley.com/doi/abs/10.1029/91JA00795>.
- C. T. Russell and R. L. McPherron. Semiannual variation of geomagnetic activity. *Journal of Geophysical Research*, 78(1):92–108, 1973. doi: 10.1029/JA078i001p00092. URL <https://agupubs.onlinelibrary.wiley.com/doi/abs/10.1029/JA078i001p00092>.
- C. T. Russell, P. J. Chi, D. J. Dearborn, Y. S. Ge, B. Kuo-Tiong, J. D. Means, D. R. Pierce, K. M. Rowe, and R. C. Snare. THEMIS Ground-Based Magnetometers. *Space Science Reviews*, 141(1):389–412, Dec 2008. ISSN 1572-9672. doi: 10.1007/s11214-008-9337-0. URL <https://doi.org/10.1007/s11214-008-9337-0>.
- T Saito. GEOMAGNETIC PULSATIONS. *SPACE SCIENCE REVIEWS*, 10(3):319+, 1969. ISSN 0038-6308.
- Takao Saito and S. Matsushita. Solar cycle effects on geomagnetic Pi2 pulsations. *Journal of Geophysical Research*, 73(1):267–286, 1968. doi: 10.1029/JA073i001p00267. URL <https://agupubs.onlinelibrary.wiley.com/doi/abs/10.1029/JA073i001p00267>.
- K. Sakaguchi, T. Nagatsuma, T. Ogawa, T. Obara, and O. A. Troshichev. Ionospheric Pc5 plasma oscillations observed by the King Salmon HF radar and their comparison with geomagnetic pulsations on the ground and in geostationary orbit. *Journal of Geophysical Research: Space Physics*, 117(A3), 2012. doi: 10.1029/2011JA016923. URL <https://agupubs.onlinelibrary.wiley.com/doi/abs/10.1029/2011JA016923>.
- JC Samson, RA GREENWALD, JM RUOHONIEMI, TJ HUGHES, and DD WALLIS. MAGNETOMETER AND RADAR OBSERVATIONS OF MAGNETOHYDRODYNAMIC CAVITY MODES IN THE EARTH'S MAGNETOSPHERE. *CANADIAN JOURNAL OF PHYSICS*, 69(8-9):929–937, AUG-SEP 1991. ISSN 0008-4204. doi: {10.1139/p91-147}.

- BR Sandel, J Goldstein, DL Gallagher, and M Spasojevic. Extreme ultraviolet imager observations of the structure and dynamics of the plasmasphere. In *Magnetospheric Imaging—The Image Prime Mission*, pages 25–46. Springer, 2003.
- T. Sarris, X. Li, and H. J. Singer. A long-duration narrowband Pc5 pulsation. *Journal of Geophysical Research: Space Physics*, 114(A1), 2009. doi: 10.1029/2007JA012660. URL <https://agupubs.onlinelibrary.wiley.com/doi/abs/10.1029/2007JA012660>.
- JD Scargle. STUDIES IN ASTRONOMICAL TIME-SERIES ANALYSIS .2. STATISTICAL ASPECTS OF SPECTRAL-ANALYSIS OF UNEVENLY SPACED DATA. *ASTROPHYSICAL JOURNAL*, 263(2):835–853, 1982. ISSN 0004-637X. doi: {10.1086/160554}.
- Xiao-Chen Shen, Quanqi Shi, Boyi Wang, Hui Zhang, Mary K Hudson, Yukitoshi Nishimura, Michael D Hartinger, Anmin Tian, Qiu-Gang Zong, IJ Rae, et al. Dayside Magnetospheric and Ionospheric Responses to a Foreshock Transient on 25 June 2008: 1. FLR Observed by Satellite and Ground-Based Magnetometers. *Journal of Geophysical Research: Space Physics*, 123(8):6335–6346, 2018.
- S. G. Shepherd. Altitude-adjusted corrected geomagnetic coordinates: Definition and functional approximations. *Journal of Geophysical Research: Space Physics*, 119(9):7501–7521, 2014. doi: 10.1002/2014JA020264. URL <https://agupubs.onlinelibrary.wiley.com/doi/abs/10.1002/2014JA020264>.
- X. Shi, J. B. H. Baker, J. M. Ruohoniemi, M. D. Hartinger, N. A. Frissell, and Jiang Liu. Simultaneous space and ground-based observations of a plasmaspheric virtual resonance. *Journal of Geophysical Research: Space Physics*, 122(4):4190–4209, 2017. doi: 10.1002/2016JA023583. URL <https://agupubs.onlinelibrary.wiley.com/doi/abs/10.1002/2016JA023583>.

- X. Shi, J. B. H. Baker, J. M. Ruohoniemi, M. D. Hartinger, K. R. Murphy, J. V. Rodriguez, Y. Nishimura, K. A. McWilliams, and V. Angelopoulos. Long-Lasting Poloidal ULF Waves Observed by Multiple Satellites and High-Latitude SuperDARN Radars. *Journal of Geophysical Research: Space Physics*, 123(10):8422–8438, 2018a. doi: 10.1029/2018JA026003. URL <https://agupubs.onlinelibrary.wiley.com/doi/abs/10.1029/2018JA026003>.
- X. Shi, J. M. Ruohoniemi, J. B. H. Baker, D. Lin, E. C. Bland, M. D. Hartinger, and W. A. Scales. Survey of Ionospheric Pc3-5 ULF Wave Signatures in SuperDARN High Time Resolution Data. *Journal of Geophysical Research: Space Physics*, 123(5):4215–4231, 2018b. doi: 10.1029/2017JA025033. URL <https://agupubs.onlinelibrary.wiley.com/doi/abs/10.1029/2017JA025033>.
- HJ Singer, DJ Southwood, RJ Walker, and MG Kivelson. Alfvén wave resonances in a realistic magnetospheric magnetic field geometry. *Journal of Geophysical Research: Space Physics*, 86(A6):4589–4596, 1981.
- HJ Singer, L Matheson, R Grubb, A Newman, and SD Bouwer. Monitoring space weather with the GOES magnetometers. In Washwell, ER, editor, *GOES-8 AND BEYOND*, volume 2812 of *PROCEEDINGS OF THE SOCIETY OF PHOTO-OPTICAL INSTRUMENTATION ENGINEERS (SPIE)*, pages 299–308. Soc Photo Opt Instrumentat Engineers; NARSIA; ASPRS, 1996. ISBN 0-8194-2200-2. doi: {10.1117/12.254077}. Conference on GOES-8 and Beyond, DENVER, CO, AUG 07-09, 1996.
- M. Smiddy, M. C. Kelley, W. Burke, F. Rich, R. Sagalyn, B. Shuman, R. Hays, and S. Lai. Intense poleward-directed electric fields near the ionospheric projection of the plasmopause. *Geophysical Research Letters*, 4(11):543–546, 1977. doi: 10.1029/GL004i011p00543. URL <https://agupubs.onlinelibrary.wiley.com/doi/abs/10.1029/GL004i011p00543>.
- D. J. Southwood. A general approach to low-frequency instability in the ring cur-

- rent plasma. *Journal of Geophysical Research*, 81(19):3340–3348, 1976. doi: 10.1029/JA081i019p03340. URL <https://agupubs.onlinelibrary.wiley.com/doi/abs/10.1029/JA081i019p03340>.
- D. J. Southwood and W. J. Hughes. Concerning the structure of Pi2 pulsations. *Journal of Geophysical Research: Space Physics*, 90(A1):386–392, 1985. doi: 10.1029/JA090iA01p00386. URL <https://agupubs.onlinelibrary.wiley.com/doi/abs/10.1029/JA090iA01p00386>.
- D. J. Southwood and WJ HUGHES. THEORY OF HYDROMAGNETIC-WAVES IN THE MAGNETOSPHERE. *SPACE SCIENCE REVIEWS*, 35(4):301–366, 1983. ISSN 0038-6308.
- David J. Southwood and Margaret G. Kivelson. Charged particle behavior in low-frequency geomagnetic pulsations, 2. Graphical approach. *Journal of Geophysical Research: Space Physics*, 87(A3):1707–1710, 1982. doi: 10.1029/JA087iA03p01707. URL <https://agupubs.onlinelibrary.wiley.com/doi/abs/10.1029/JA087iA03p01707>.
- David J. Southwood and Margaret G. Kivelson. Mirror instability: 1. Physical mechanism of linear instability. *Journal of Geophysical Research: Space Physics*, 98(A6):9181–9187, 1993. doi: 10.1029/92JA02837. URL <https://agupubs.onlinelibrary.wiley.com/doi/abs/10.1029/92JA02837>.
- DJ Southwood, JW DUNGEY, and ETHERING. RJ. BOUNCE RESONANT INTERACTION BETWEEN PULSATIONS AND TRAPPED PARTICLES. *PLANETARY AND SPACE SCIENCE*, 17(3):349–&, 1969. ISSN 0032-0633. doi: {10.1016/0032-0633(69)90068-3}.
- J. A. E. Stephenson and A. D. M. Walker. HF radar observations of Pc5 ULF pulsations driven by the solar wind. *Geophysical Research Letters*, 29(9):8–1–8–4, 2002. doi: 10.

1029/2001GL014291. URL <https://agupubs.onlinelibrary.wiley.com/doi/abs/10.1029/2001GL014291>.

Balfour Stewart. XXII. On the great magnetic disturbance which extended from August 28 to September 7, 1859, as recorded by photography at the Kew Observatory. *Philosophical Transactions of the Royal Society of London*, 151:423–430, 1861.

M Sugiura and T Kamei. Equatorial Dst index 1957–1986, IAGA Bull., 40. *by A. Berthelier and M. Menville (Int. Serv. Geomagn. Indices Publ. Off., Saint Maur, 1991)*, 1991.

Masahisa Sugiura. Evidence of low-frequency hydromagnetic waves in the exosphere. *Journal of Geophysical Research*, 66(12):4087–4095, 1961.

P. R. Sutcliffe. Observations of Pi2 pulsations in a near ground state magnetosphere. *Geophysical Research Letters*, 25(21):4067–4070, 1998. doi: 10.1029/1998GL900092. URL <https://agupubs.onlinelibrary.wiley.com/doi/abs/10.1029/1998GL900092>.

Peter R. Sutcliffe and Kiyohumi Yumoto. On the cavity mode nature of low-latitude Pi 2 pulsations. *Journal of Geophysical Research: Space Physics*, 96(A2):1543–1551, 1991. doi: 10.1029/90JA02007. URL <https://agupubs.onlinelibrary.wiley.com/doi/abs/10.1029/90JA02007>.

K Takahashi and RL McPherron. Standing Hydromagnetic Oscillations in the Magnetosphere. *PLANETARY AND SPACE SCIENCE*, 32(11):1343–1359, 1984. ISSN 0032-0633.

K. Takahashi, R. W. McEntire, A. T. Y. Lui, and T. A. Potemra. Ion flux oscillations associated with a radially polarized transverse Pc 5 magnetic pulsation. *Journal of Geophysical Research: Space Physics*, 95(A4):3717–3731, 1990. doi: 10.1029/JA095iA04p03717. URL <https://agupubs.onlinelibrary.wiley.com/doi/abs/10.1029/JA095iA04p03717>.

Kazue Takahashi and Kan Liou. Longitudinal structure of low-latitude Pi2 pulsations and its dependence on aurora. *Journal of Geophysical Research: Space Physics*, 109(A12), 2004. doi: 10.1029/2004JA010580. URL <https://agupubs.onlinelibrary.wiley.com/doi/abs/10.1029/2004JA010580>.

Kazue Takahashi, Shin-ichi Ohtani, and Brian J. Anderson. Statistical analysis of Pi2 pulsations observed by the AMPTE CCE Spacecraft in the inner magnetosphere. *Journal of Geophysical Research: Space Physics*, 100(A11):21929–21941, 1995. doi: 10.1029/95JA01849. URL <https://agupubs.onlinelibrary.wiley.com/doi/abs/10.1029/95JA01849>.

Kazue Takahashi, Dong-Hun Lee, Masahito Nosé, Roger R. Anderson, and W. Jeffrey Hughes. CRRES electric field study of the radial mode structure of Pi2 pulsations. *Journal of Geophysical Research: Space Physics*, 108(A5), 2003. doi: 10.1029/2002JA009761. URL <https://agupubs.onlinelibrary.wiley.com/doi/abs/10.1029/2002JA009761>.

Kazue Takahashi, David Berube, Dong-Hun Lee, Jerry Goldstein, Howard J. Singer, Farideh Honary, and Mark B. Moldwin. Possible evidence of virtual resonance in the dayside magnetosphere. *Journal of Geophysical Research: Space Physics*, 114(A5), 2009. doi: 10.1029/2008JA013898. URL <https://agupubs.onlinelibrary.wiley.com/doi/abs/10.1029/2008JA013898>.

Kazue Takahashi, Robert Lysak, Massimo Vellante, Craig A Kletzing, Michael D Hartinger, and Charles W Smith. Observation and numerical simulation of cavity mode oscillations excited by an interplanetary shock. *Journal of Geophysical Research: Space Physics*, 123(3):1969–1988, 2018a.

Kazue Takahashi, Satoshi Oimatsu, Masahito Nosé, Kyungguk Min, Seth G. Claudepierre, Anthony Chan, John Wygant, and Hyomin Kim. Van Allen Probes Obser-

- vations of Second Harmonic Poloidal Standing Alfvén Waves. *Journal of Geophysical Research: Space Physics*, 123(1):611–637, 2018b. doi: 10.1002/2017JA024869. URL <https://agupubs.onlinelibrary.wiley.com/doi/abs/10.1002/2017JA024869>.
- M. Teramoto, M. Nosé, and P. R. Sutcliffe. Statistical analysis of Pi2 pulsations inside and outside the plasmasphere observed by the polar orbiting DE-1 satellite. *Journal of Geophysical Research: Space Physics*, 113(A7), 2008. doi: 10.1029/2007JA012740. URL <https://agupubs.onlinelibrary.wiley.com/doi/abs/10.1029/2007JA012740>.
- M. Teramoto, N. Nishitani, V. Pilipenko, T. Ogawa, K. Shiokawa, T. Nagatsuma, A. Yoshikawa, D. Baishev, and K. T. Murata. Pi2 pulsation simultaneously observed in the E and F region ionosphere with the SuperDARN Hokkaido radar. *Journal of Geophysical Research: Space Physics*, 119(5):3444–3462, 2014. doi: 10.1002/2012JA018585. URL <https://agupubs.onlinelibrary.wiley.com/doi/abs/10.1002/2012JA018585>.
- Mariko Teramoto, Nozomu Nishitani, Yukitoshi Nishimura, and Tsutomu Nagatsuma. Latitudinal dependence on the frequency of Pi2 pulsations near the plasmopause using THEMIS satellites and Asian-Oceanian SuperDARN radars. *Earth, Planets and Space*, 68(1):22, Feb 2016. ISSN 1880-5981. doi: 10.1186/s40623-016-0397-1. URL <https://doi.org/10.1186/s40623-016-0397-1>.
- Nikolai A. Tsyganenko and David P. Stern. Modeling the global magnetic field of the large-scale Birkeland current systems. *Journal of Geophysical Research: Space Physics*, 101(A12):27187–27198, 1996. doi: 10.1029/96JA02735. URL <https://agupubs.onlinelibrary.wiley.com/doi/abs/10.1029/96JA02735>.
- DL Turner, SG Claudepierre, JF Fennell, TP O’Brien, JB Blake, C Lemon, M Gkioulidou, K Takahashi, GD Reeves, S Thaller, et al. Energetic electron injections deep into the

- inner magnetosphere associated with substorm activity. *Geophysical Research Letters*, 42(7):2079–2087, 2015.
- JA Van Allen, GH Ludwig, EC Ray, and CE McIlwain. Observation of high intensity radiation by satellites 1958 Alpha and Gamma. *Journal of Jet Propulsion*, 28(9):588–592, 1958.
- James Alfred Van Allen and Louis A Frank. Radiation around the Earth to a radial distance of 107,400 km. *Nature*, 183, 1959.
- Boyi Wang, Yukitoshi Nishimura, Heli Hietala, Xiao-Chen Shen, Quanqi Shi, Hui Zhang, Larry Lyons, Ying Zou, Vassilis Angelopoulos, Yusuke Ebihara, et al. Dayside Magnetospheric and Ionospheric Responses to a Foreshock Transient on 25 June 2008: 2. 2-D Evolution Based on Dayside Auroral Imaging. *Journal of Geophysical Research: Space Physics*, 123(8):6347–6359, 2018.
- James A Wanliss and Kristin M Showalter. High-resolution global storm index: Dst versus SYM-H. *Journal of Geophysical Research: Space Physics*, 111(A2), 2006.
- C. L. Waters, F. W. Menk, and B. J. Fraser. The resonance structure of low latitude Pc3 geomagnetic pulsations. *Geophysical Research Letters*, 18(12):2293–2296, 1991. doi: 10.1029/91GL02550. URL <https://agupubs.onlinelibrary.wiley.com/doi/abs/10.1029/91GL02550>.
- D. M. Wright, T. K. Yeoman, I. J. Rae, J. Storey, A. B. Stockton-Chalk, J. L. Roeder, and K. J. Trattner. Ground-based and Polar spacecraft observations of a giant (Pg) pulsation and its associated source mechanism. *Journal of Geophysical Research: Space Physics*, 106(A6):10837–10852, 2001. doi: 10.1029/2001JA900022. URL <https://agupubs.onlinelibrary.wiley.com/doi/abs/10.1029/2001JA900022>.

- N. V. Yagova, V. A. Pilipenko, L. J. Lanzerotti, M. J. Engebretson, A. S. Rodger, S. Lepidi, and V. O. Papitashvili. Two-dimensional structure of long-period pulsations at polar latitudes in Antarctica. *Journal of Geophysical Research: Space Physics*, 109(A3), 2004. doi: 10.1029/2003JA010166. URL <https://agupubs.onlinelibrary.wiley.com/doi/abs/10.1029/2003JA010166>.
- TK Yeoman and DM Wright. ULF waves with drift resonance and drift-bounce resonance energy sources as observed in artificially-induced HF radar backscatter. *ANNALS GEOPHYSICAE*, 19(2):159–170, FEB 2001. ISSN 0992-7689. doi: {10.5194/angeo-19-159-2001}.
- T.K. Yeoman, D.K. Milling, and D. Orr. Pi2 pulsation polarization patterns on the U.K. sub-auroral magnetometer network (SAMNET). *Planetary and Space Science*, 38(5):589 – 602, 1990. ISSN 0032-0633. doi: [https://doi.org/10.1016/0032-0633\(90\)90065-X](https://doi.org/10.1016/0032-0633(90)90065-X). URL <http://www.sciencedirect.com/science/article/pii/003206339090065X>.
- Jie Zhang, IG Richardson, DF Webb, N Gopalswamy, E Huttunen, JC Kasper, NV Nitta, W Poomvises, BJ Thompson, C-C Wu, et al. Solar and interplanetary sources of major geomagnetic storms (Dst - 100 nT) during 1996–2005. *Journal of Geophysical Research: Space Physics*, 112(A10), 2007.
- XY Zhang, Q-G Zong, YF Wang, H Zhang, L Xie, SY Fu, CJ Yuan, C Yue, B Yang, and ZY Pu. ULF waves excited by negative/positive solar wind dynamic pressure impulses at geosynchronous orbit. *Journal of Geophysical Research: Space Physics*, 115(A10), 2010.
- Xiaoming Zhu and Margaret G. Kivelson. Global mode ULF pulsations in a magnetosphere with a nonmonotonic Alfvén velocity profile. *Journal of Geophysical Research: Space Physics*, 94(A2):1479–1485, 1989. doi: 10.1029/JA094iA02p01479. URL <https://agupubs.onlinelibrary.wiley.com/doi/abs/10.1029/JA094iA02p01479>.

- Q.-G. Zong, X.-Z. Zhou, Y. F. Wang, X. Li, P. Song, D. N. Baker, T. A. Fritz, P. W. Daly, M. Dunlop, and A. Pedersen. Energetic electron response to ULF waves induced by interplanetary shocks in the outer radiation belt. *Journal of Geophysical Research: Space Physics*, 114(A10), 2009. doi: 10.1029/2009JA014393. URL <https://agupubs.onlinelibrary.wiley.com/doi/abs/10.1029/2009JA014393>.
- Qiugang Zong, Robert Rankin, and Xuzhi Zhou. The interaction of ultra-low-frequency pc3-5 waves with charged particles in Earth's magnetosphere. *Reviews of Modern Plasma Physics*, 1(1):10, 2017.
- S. Zou, L. R. Lyons, C.-P. Wang, A. Boudouridis, J. M. Ruohoniemi, P. C. Anderson, P. L. Dyson, and J. C. Devlin. On the coupling between the Harang reversal evolution and substorm dynamics: A synthesis of SuperDARN, DMSP, and IMAGE observations. *Journal of Geophysical Research: Space Physics*, 114(A1), 2009. doi: 10.1029/2008JA013449. URL <https://agupubs.onlinelibrary.wiley.com/doi/abs/10.1029/2008JA013449>.

Appendices

Appendix A

Methodology: Lomb-Scargle Periodogram

The Lomb-Scargle periodogram is a spectrum analysis technique especially advantageous for unevenly sampled data [Lomb, 1976, Scargle, 1982]. It has recently been used to search Pc5 ULF oscillations from the SuperDARN common mode data [Bland et al., 2014]. The periodogram at angular frequency ω is defined as

$$P(\omega) = \frac{1}{2\sigma^2} \left(\frac{[\sum_i x_i \cos \omega(t_i - \tau)]^2}{\sum_i \cos^2 \omega(t_i - \tau)} + \frac{[\sum_i x_i \sin \omega(t_i - \tau)]^2}{\sum_i \sin^2 \omega(t_i - \tau)} \right), \quad (\text{A.1})$$

where x_i is the sampled signal at sampling time t_i , σ is the standard deviation of the data, and the constant τ is defined such that $\tan(2\omega\tau) = \frac{\sum_i \sin 2\omega t_i}{\sum_i \cos 2\omega t_i}$ and $P(\omega)$ is invariant under a constant shift applied to all the time stamps. The power spectrum is normalized by the variance of the signal (σ^2). A sufficiently high value of NPP indicates the existence of a wave signature at the associated frequency. The significance of this prediction used to be evaluated by the false alarm probability, namely the probability that the peak was produced by white Gaussian noise:

$$p = 1 - (1 - e^{-z})^M \approx M \cdot e^{-z} \quad (\text{A.2})$$

Here M is the number of independent frequencies which is roughly the number of signal points, and z is the NPP. However, this evaluation is frequency-independent and may become unevenly fair when the target frequency has a broad range. The ULF wave frequency range is typically from 1.0 to 1000 mHz, which covers three orders of magnitude. Assuming the observed wave signatures have a comparable number of cycles, the NPP of a high-frequency wave should be lower than that of a low-frequency wave due to lower duty cycle, as verified in the numerical experiments below.

In order to determine thresholds of NPP that account for wave periods, numerical experiments were conducted to explore the statistically expected NPP of signals with different wave periods. SuperDARN measurements are simulated by assuming the signal as a mixture of a sinusoidal component and a Gaussian background noise. It should be pointed out that besides the wave period, NPP also depends on signal parameters including the number of data points, duty cycle of the sinusoidal component, and the signal-to-noise-ratio (SNR). The duty cycle is defined as $N_{CYC} \cdot T_{sin}/N$, where N_{CYC} is the number of sinusoidal cycles, T_{sin} is the wave period, and N is the signal length. The SNR is determined by the wave amplitude A_{sin} normalized by the standard deviation of Gaussian noise. In the simulations presented in this paper, A_{sin} and T_{sin} are both assumed to be constant within one signal. Figure A.1(a) shows a sample simulation with a signal length of $N = 600$. This length is equivalent to 1 h given 6 s sampling rate of the SuperDARN THEMIS mode data. The length is chosen so as to cover a few Pc5 wave cycles. The sinusoidal signal component has a period of 45 6-s steps in time (i.e., 270 s) and an amplitude of 2. The signal consists of 4 cycles. Figure A.1(b) shows the Lomb-Scargle periodogram of the sample simulation. The NPP is found to be 37.6 at a period of 46 time steps, which is within 5% of the designed value.

Figure A.2 illustrates the procedures to derive a wave-period dependent threshold NPP

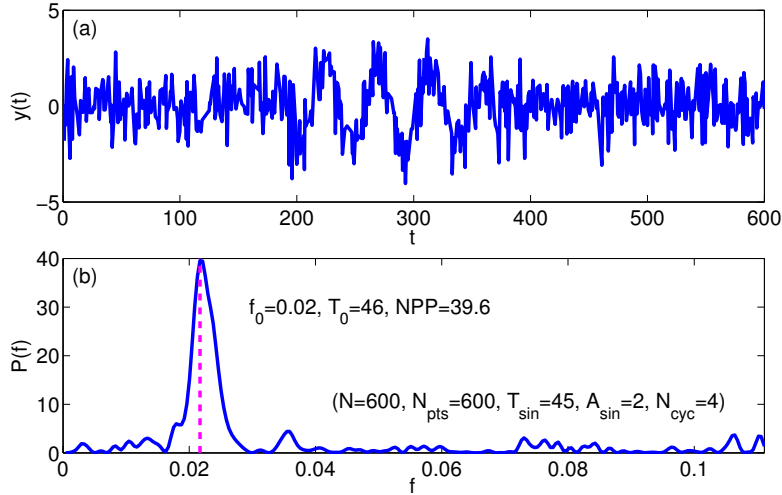


Figure A.1: Example Lomb-Scargle periodogram analysis: (a) A simulated signal with length of 600 points, wave period of 45 points, wave amplitude of 2, and 4 sinusoidal cycles; (b) Lomb-Scargle periodogram of the simulated signal. The magenta dashed line indicates the NPP is 37.6, the wave frequency is 0.02, and the wave period is 46.

for signals with length of $N = 600$. 2000 simulations were performed to be statistically significant for the same parameter set as in Figure A.1 ($N = 600$, $T_{sin} = 45$, $A_{sin} = 2$, $N_{CYC} = 4$). The effectiveness of Lomb-Scargle periodogram for this parameter set is evaluated by the correct-period probability P_{Cf} , which is defined as the ratio between the number of simulations for which the wave period is consistently identified by Lomb-Scargle periodogram and the total number of simulations. Figure A.2(a) shows the distribution of NPPs with consistently identified wave period. The P_{Cf} of this parameter set is $1658/2000 = 0.83$. The mean value of the period-consistent NPPs is 38.2 and the standard deviation is 5.0. Figure A.2(b) shows the mean NPP (blue) and P_{Cf} (green) for N_{CYC} from 1 to 6 with ($N = 600$, $T_{sin} = 45$, $A_{sin} = 2$). It is visible that Lomb-Scargle periodogram has a better performance in identifying wave period correctly with more cycles. The NPP also increases with cycle number monotonically. Defining a threshold P_{Cf} of 80%, the threshold NPP corresponding to this probability can be calculated via linear interpolation as shown by the magenta dashed lines. The threshold NPP for ($N = 600$, $T_{sin} = 45$, $A_{sin} = 2$) is 36.8. Figure

A.2(c) shows the threshold NPP for A_{sin} from 1 to 10 with ($N = 600, T_{sin} = 45$). The threshold NPP increases with the wave amplitude and approaches a stable level of ~ 54.3 when A_{sin} is above 4. The asymptotic level represents the threshold NPP of the given signal length and wave period. Figure A.2(d) shows the threshold NPPs of 8 wave periods in the Pc5 range (150 s - 600 s): 25, 30, 37, 45, 55, 67, 82, and 100. These threshold NPPs are linearly fitted by $NPP = 0.71T_{sin} + 21.2$. NPP above the value specified by this equation indicates the existence of a wave signature at the associated period with a probability of more than 80%.

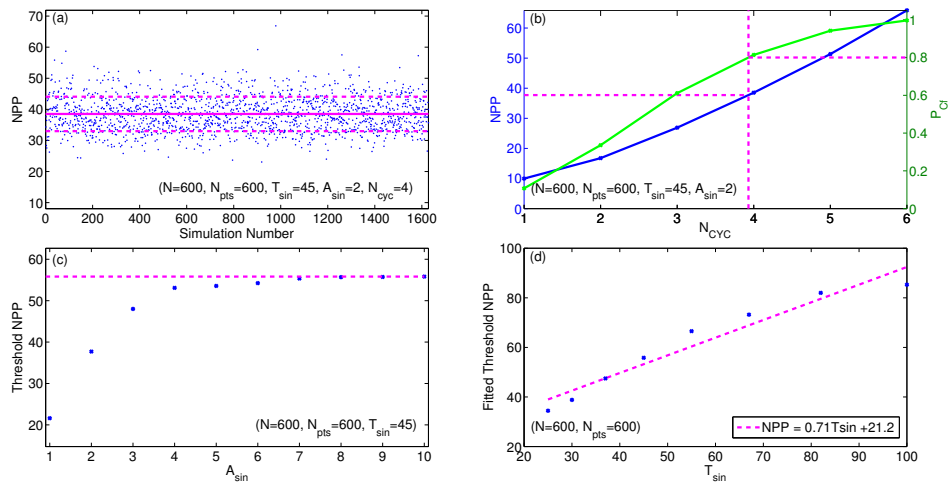


Figure A.2: Procedure to derive wave period-dependent threshold NPP. (a) NPP distribution for ($N = 600, T_{sin} = 45, A_{sin} = 2, N_{CYC} = 4$); (b) P_{Cf} (green) and mean NPP (blue) for $N_{CYC} = 1 - 6$ with ($N = 600, T_{sin} = 45, A_{sin} = 2$); (c) Threshold NPP for $A_{sin} = 1 - 10$ with ($N = 600, T_{sin} = 45$); (d) Asymptotic threshold NPP for $T_{sin} = 25 - 100$ with ($N = 600$). See text for details.

It should be noted that the empirical equation obtained by fitting values of NPP depends on two observables of Lomb-Scargle periodogram: T_{sin} and NPP. The threshold NPP for a high frequency wave signature is lower than for a lower frequency wave, which is reasonable considering that more cycles of high frequency waves are needed to achieve the same duty cycle. The classical false alarm probability uniquely dependent on NPP is overly strict for high frequency wave signatures and not strict enough for low frequency wave signatures.

In Figure A.2(c), the asymptotic level may raise the threshold for small amplitude wave signatures. However, this could exclude weak signals relative to the background noise, thus increasing the reliability of wave signature identification. In real SuperDARN data, the number of data points available in a 1-h interval could deviate from 600 due to gaps or oversampling. Gaps and oversampling effects were simulated and analyzed with the same method introduced above. The threshold NPP equations for different numbers of points (N_{pts}) are listed in Table 3.1. The threshold equations for Pc3-4 wave identification are based on a basic length of 30 minutes.